Quantitative Analysis of Local Mineral Content and Composition During Bone Growth and Remodeling

D I S S E R T A T I O N

zur Erlangung des akademischen Grades

d o c t o r r e r u m n a t u r a l i u m

(Dr. rer. nat.)

im Fach Physik

eingereicht an der

Mathematisch-Naturwissenschaftlichen Fakultät I
der Humboldt-Universität zu Berlin

von

Diplom Ingenieur Andreas Roschger

Präsident der Humboldt-Universität zu Berlin
Prof. Dr. Jan-Hendrik Olbertz

Dekan der Mathematisch-Naturwissenschaftlichen Fakultät
Prof. Dr. Elmar Kulke

Gutachter: 1. . . . Prof. Dr. Jürgen P. Rabe . . . . .

2. . . . Prof. Dr. Claus-Christian Glüer . . .

3. . . . Prof. Dr. Dr.h.c. Peter Fratzl . . .

Tag der mündlichen Prüfung: . . . 17. August 2015 . . .

I love science, and it pains me to think that so many are terrified of the subject or feel that choosing science means you cannot also choose compassion, or the arts, or be awed by nature. Science is not meant to cure us of mystery, but to reinvent and reinvigorate it.

Robert Sapolsky

Kurzfassung

Da das menschliche Skelett permanent Belastungen ausgesetzt ist, sind dessen mechanischen Eigenschaften von entscheidender Bedeutung. Sie hängen unter anderem von der Knochenmineralisierung ab. Während Knochenumbau, Wachstum oder Frakturheilung wird von knochenaufbauenden Zellen (Osteoblasten) eine zunächst nicht-mineralisierte Matrix (Osteoid) gebildet, die hauptsächlich aus Kollagen Typ I besteht und anschließend mineralisiert. Hierbei werden manche der Zellen in den Knochen eingebaut und differenzieren zu Osteozyten, deren Dendriten sie untereinander und mit der Knochenoberfläche verbinden. Es gibt Hinweise darauf, dass Osteozyten über das so gebildete Netzwerk die Materialzusammensetzung in ihrer Umgebung beeinflussen können.

Das Ziel der Studien, die im Rahmen dieser Arbeit vorgestellt werden, war es neue Informationen über die elementare Zusammensetzung des mineralisierten Knochens zu gewinnen. Um unterschiedliche Methoden wie quantitative Rückstreuelektronenmikroskopie (qBEI), energiedispersiver Röntgenanalyse (EDX), Raman Mikrospektroskopie und konfokaler Lasermikroskopie (CLSM) zu kombinieren, wurden neue Routinen entwickelt oder bereits etablierte Methoden verbessert. Mit diesen Techniken konnten sowohl humane Proben (Oberschenkelquerschnitte von gesunden Erwachsenen und Kindern) als auch Mausknochen (Oberschenkel Längs- und Querschnitte von zwei Mausmodellen) charakterisiert werden.

In einer ersten, grundlegenden Studie wurden zwei Parameter verglichen, die beide eng mit der Knochenmineralisierung verknüpft sind. So zeigte die Gegenüberstellung des $mineral/matrix$ Raman-Wertes und der Kalziumkonzentration (ermittelt mit qBEI) gute Übereinstimmung mit theoretischen Überlegungen. Diese Methoden wurden auch verwendet um Knochengewebe von Mäusen zu charakterisieren bei denen ein genetischer Defekt zu einem Mangel von Sclerostin (ein Negativ - Regulator für Knochenaufbau) führte. So war es möglich nachzuweisen, dass eine hierdurch verstärkte Knochenneubildung zu einer veränderten Mineralisationskinetik des Knochens führen kann. Nachdem zukünftig Sclerostinantikörper für die Behandlung von Knochenkrankheiten eingesetzt werden sollen, haben diese Erkenntnisse große medizinische Bedeutung. Aus diesem Grund wurde auch die Mineraldichteverteilung eines Mausmodells mit extrem fragilem Knochen (Osteogenesis Imperfecta, OI) untersucht. Die Mäuse wurden mit Sclerostinantikörpern behandelt und mit unbehandelten Tieren verglichen. Es zeige sich ein signifikanter Knochenzuwachs doch die Mineraldichteverteilung veränderte sich gleichermaßen für gesunde und für OI Mäuse.

In einer Studie am humanen kompakten Knochen konnten der Zusammenhang zwischen dem Osteozytennetzwerk und der Knochenzusammensetzung untersucht werden. Elemente wie Na, Mg und S wiesen typische Konzentrationsverteilungen auf. Die entwickelten Routinen wurden auch verwendet um Mineralisationsfronten zu charakterisieren, welche eine kritische Phase der Knochenentwicklung darstellen. Es zeigte sich, dass die Konzentrationen von K, Mg, Na und Cl abhängig von dem analysierten anatomischen Ort, stark voneinander abweichen.

Abschließend kann gesagt werden, dass durch die Entwicklung neuer Routinen zusätzliche Erkenntnisse über die Knochenmineralisierung und Zusammensetzung gewonnen werden konnten. Die Resultate sind von medizinischer und biologischer Bedeutung und tragen zu aktuellen Debatten über die Knochenentwicklung bei.

Abstract

Bone matrix mineralization is an important quantity linked to mechanical properties of the skeleton. If new bone is formed (in the course of bone remodeling, growth or fracture healing), osteoblasts produce a soft non-mineralized matrix consisting of mainly collagen type I (Osteoid), which eventually mineralizes. Some of the osteoblasts get embedded in the bone matrix and differentiate to osteocytes. These cells develop dendrites, which interconnect osteocytes to each other and to the cells at the bone surface, forming the osteocyte-lacuna canaliculi network (OLCN). There is evidence that osteocytes have the ability to alter the composition of bone tissue adjacent to the lacunae and the canaliculi.

The purpose of the presented work was to gain new insight into the elemental composition of mineralized bone matrix at different sites of human bone tissue, and in mouse models linked to human genetic diseases. Routines for the combination of quantitative backscattered electron imaging (qBEI), energy dispersive X-ray analysis (EDX), Raman micro-spectroscopy, and confocal laser scanning microscopy (CLSM) were developed. Using these tools, human (femur cross sections from healthy adults and children) and murine samples (femur long-and cross sections of two mouse models) were analyzed with focus on the elemental composition.

In a methodological study the consistency of matrix mineralization measured by Raman microspectroscopy (e.g. the $mineral/matrix$ ratio) and the Calcium content ($wt\%Ca$) as measured by qBEI was proved. Both methods were applied to a mouse model exhibiting induced bone overgrowth due to a genetic defect causing a lack of Sclerostin, which is a negative regulator for bone formation. We found changes in the mineralization kinetics depending on the anatomical site. This result is of clinical importance since sclerostin antibodies are suggested for future treatment of diseases characterized by fragile bone. Hence, also a mouse model of a brittle bone disease (Osteogenesis Imperfecta) was analyzed with and without sclerostin antibody treatment. A significant increase in bone mass was documented while the mineralization pattern revealed no interaction between genotype and treatment.

The correlation between OLCN and the composition of the mineralized matrix was examined in the same regions of human compact bone. Characteristic distributions of the minor elements (Mg, Na, S) were found. The developed tools were also used to investigate mineralization fronts, reflecting a critical stage of bone development. Differences in the Ca/P ratio and in the concentrations of K, Mg, Na and Cl depending on the anatomical site were revealed.

In conclusion, using newly developed measurement routines, it was possible to gain novel information of bone mineralization and composition. The results contribute to actively debated issues of biological and medical importance.

Acknowledgements

The presented work is the result of a close cooperation of the Ludwig Boltzmann Institute of Osteology (Vienna, Austria) and the Biomaterials Department of the Max Planck Institute of Colloids and Interfaces (Potsdam, Germany). I want to acknowledge the teams of both institutes for a constructive, creative and pleasant working environment. Thanks are dedicated to the people who supported me during the last years facilitating this thesis:

Ao.Univ.Prof.Dr. Klaus Klaushofer for giving me the opportunity to follow my scientific carrear at the LBIO, and for his trust and motivation.

Prof.Dr. Peter Fratzl for his supervision, for taking time for extensive scientific discussions, and for his ability to arouse interest and enthusiasm in science.

Prof.Dr. Paul Roschger for advices and numerous scientific discussions, and for his trust and his support anytime whenever I needed it.

Dr. Eleftherios Paschalis, Dr. Sonja Gamsjäger und Dr. Norbert Hassler for their expertise in Raman-spectroscopy and for their time whenever questions raised.

Dr. Stéphane Blouin, Dr. Nadja Fratzl-Zelman, Dr. Barbara Misof for sharing their expertise and numerous constructive scientific discussions.

Gerda Dienst, Daniela Gabriel, Petra Keplinger, Sonja Lueger, Phedra Messner (MSc) for sample preparation, assistance during data acquisition and evaluation, and the enjoyable working atmosphere.

Dr. Wolfgang Wagermaier, Dr.habil. Richard Weinkamer, Dipl.-Phys. Felix Repp, Dr. Michael Kerschnitzki for sharing their expertise, offering new perspectives and for integrating me into their work at the Biomaterials Department of the MPIKG.

My special thanks are addressed to my parents **Mauki and Peter** for facilitating my studies, for support and encouragement during the last years and their trust in my abilities. Thanks are also addressed to my brother **Christoph** for his advices and corrections and to my girlfriend **Carmen** for corrections, her sympathy, and for sharing her passion for science with me.

Contents

Chapter 1

Introduction

The human skeleton meets a multitude of requirements such as resistance to high impact forces and long-term strain, facilitation of body growth, and fracture healing. In its role as an endocrine organ, hormones excreted from bone cells are permanently involved in systemic regulation mechanisms. These biomechanical and biological properties require a complex but highly adaptive bone architecture and composition which is achieved by a hierarchical organization from the organ level down to the nano-range (Figure 2.1). Especially the combination of the tough organic matrix, mainly consisting of collagen type I, and a stiff mineral phase leads to a high resistance to fracture despite low material weight.

Adaption to mechanical load and renewal of matured bone matrix is facilitated by permanent bone remodeling. Through the interplay of osteoclasts (bone resorbing cells) and osteoblasts (bone forming cells), old bone matrix is gradually replaced by young tissue, accounting for high heterogeneity in tissue age. Tissue age is linked to the degree of mineralization and thus also to the local material stiffness [1]. Hence, bone tissue consists of compartments exhibiting distinct variations in mechanical properties what inhibits crack propagation, likely decreasing the susceptibility to fracture [2]. During the bone-formation phase osteoblasts produce non-mineralized matrix, called osteoid, which eventually mineralizes. Some osteoblasts get entrapped in the osteoid tissue and subsequently start to differentiate to another cell type - the osteocyte. While differentiation, early osteocytes change their protein expression pattern and start to develop cell processes forming a dense network that interconnects cells and bone surface. Already in 1951 H. Kind introduced the exciting concept of osteocytic osteolysis, suggesting osteocytes, have the ability to interact with their proximal environment allowing deposition and resorption of mineral from the matrix [3]. The osteocyte lacunae canaliculi network (OLCN) provides paths for protein secretion, communication, nutrition supply, ion exchange and mechanosensing capabilities [4]. Osteocytes are reported to interact with cells on the bone surface, thus being part of the regulatory mechanism for bone resorption and formation [5].

In healthy adult humans, bone remodeling renews the bone matrix continuously without affecting the overall bone mass. Hence, disturbances of this system caused by genetic defects, acquired disorders, malnutrition, reduced physical activity or other environmental factors lead to an imbalance of bone formation and resorption or to alterations in the molecular structure.

Osteoporosis is one of the most abundant diseases affecting mainly postmenopausal women and elderly men [6]. Men sustain $20 - 30$ % of all osteoporotic fractures [7]. About 40 % of women older than 50 years suffer a fracture related to post-menopausal Osteoporosis [6]. Postmenopausal Osteoporosis is a systemic disease mainly characterized by an altered bone turnover leading to a net loss of bone mass [8]. About 20 % of women suffering an osteoporotic hip fracture have long term impairments in the ability to walk and osteoporotic vertebral fractures often cause back pain, kyphosis (spinal curvature), and height loss [9]. According to the demographic development of our society, bone health will be a major topic to ensure a high quality of life for elderly people.

Beside Osteoporosis, there are also many other pathological changes in bone development known [10]. The investigation of bone samples from patients or from animal models linked to a certain disease is essential for the development and optimization of new treatment strategies. Characterizing bone matrix under pathological conditions often provides valuable insight into the fundamental mechanisms of osteogenesis, which might not show up in studies on healthy bone. An illustrative example is Osteogenesis Imperfecta or brittle bone disorder, a heritable bone condition caused by mutation of genes encoding collagen type I or a collagen-linked protein leading to low bone mass and altered bone material properties [11]. There are currently more than 1500 mutations known causing Osteogenesis Imperfecta with mild to severe (perinatal lethal) phenotypes [11]. The investigation of bone biopsies taken from the iliac crest of Osteogenesis Imperfecta patients revealed abnormally increased bone matrix mineralization, likely contributing to bone fragility [12]. From this and other studies we learn that (i) beside bone volume also intrinsic bone material parameters must be taken into consideration for a comprehensive tissue characterization and (ii) it must be kept in mind that mineral and organic properties are closely connected and should be interpreted in the context of each other. The situation appears even more complicated when it is taken into account that compositions of mineral and of organic matrix are not static but change in the course of time. This is reported to happen extensively at very early stages of mineralization where new bone is formed (during growth, fracture healing or remodeling), but also at later time points the composition of bone distinctly depends on the tissue age [13, 14, 15, 16].

The considerations made above highlight that an approach to characterize bone material needs to combine specialized methods. An optimized measurement strategy must consider consistency of sample preparation according to differing sample processing requirements depending on the applied techniques. Furthermore, damage of the specimen surface caused during data acquisition might adulterate subsequently obtained parameters. Hence, the aim of this thesis is to modify, extend and combine methods to create novel tools for the investigation of bone material. Thus, facilities available at the Ludwig Boltzmann Institute of Osteology (Vienna, Austria) and the Max Planck Institute for Colloids and Interfaces (Potsdam, Germany) are used to gain information on same regions of interest (ROI) of embedded human and murine bone samples. Using this approach for a predefined ROI, information on the sample composition, mineral and organic matrix, tissue age and OLCN structure, thus allowing a more comprehensive interpretation of the material properties is gained. Therefore, standardized measurement routines and sample preparation protocols for quantitative backscattered

electron imaging (qBEI), energy dispersive X-ray analysis (EDX), confocal laser scanning microscopy (CLSM) were adapted or newly developed with a focus on compatibility amongst these methods and to Raman micro-spectroscopy. As parameters linked to the degree of mineralization are accessible by qBEI and Raman, the corresponding quantities on the very same ROIs in human osteonal bone were investigated with both methods. In the associated paper, this correlation as well as the contribution of biological and technical fluctuations has been presented (A. Roschger et al., JBO 2014) [17].

Combining qBEI, CLSM and Raman micro-spectroscopy leads to new insight into the mineralization kinetics in mice carrying a defect in the *Sost* gene (Sost-knockout *SostKO*) (N. Hassler* and A. Roschger*[1] et al., J Bone Miner Res 2014) [18]. This gene encodes sclerostin, which is known to be a negative regulator for bone formation [19]. Hence, *SostKO* mice are expected to exhibit high bone mass. The developed routines provide access to tissue age specific parameters like degree of mineralization and organic matrix properties. These findings are of special clinical importance since the administration of sclerostin antibodies *SclAB* (targeting the same pathway) is one of the most promising approaches for future treatment of Osteoporosis and other bone fragility diseases [20]. The obvious follow-up study was to evaluate the mineralization pattern in a mouse model suffering a brittle bone disorder related to extremely low bone mass (namely Osteogenesis Imperfecta) with and without SclAB treatment (A. Roschger et al. Bone 2014) [21].

The concept of osteocytic osteolysis assumes that osteocytic activity and the OLCN structure are linked to bone material properties and composition [22, 23]. Additionally, osteocytes are known to play a major role in the very early phase of mineralization [4] and impaired osteocyte activity causes severe mineralization defects [24]. Hence, an examination of major and minor elemental concentrations at regions with different OLCN structure and at mineralization fronts of different anatomical sites was performed using a combination of qBEI, EDX and CLSM. The aims of these projects are to gain information on the role of minor elements in early stages of mineralization and to shed light on the impact of the OLCN on the bone material composition.

[1]* Both authors contributed equally to this paper and are listed in alphabedical order

Chapter 2

State of the Art

2.1 Bone Structure, Remodeling, and Development

2.1.1 Multiscale Structure and Composition of Long Bone

Long bone is multi-structurally organized, ranging from the organ level down to the nano-scale resulting in the capability to resist high forces without fracturing despite low material weight [25]. As shown in Figure 2.1 a compact cortical shell of mineralized bone matrix encases the bone marrow. In contrast to this (diaphyseal) part of the long bone in metaphyseal regions (adjacent to the growth plate), a spongy (trabecular) bone structure is located inside the bone marrow cavity (left image in Figure 2.1). At these regions near the joints, the organ is most sensitive to mechanical forces requiring this additional stabilization [26]. In humans the cortical thickness of the femur midshaft is around 7.5 mm (65 years old women) and decreases during further aging [27]. Typical values for trabecular thickness in healthy adult humans are $150 - 180$ μm with a calcified bone volume to tissue volume fraction of around 18 % [28, 29]. In the last years much progress was made in the characterization of the structural properties of bone. Modern micro-computer tomography (μCT) devices provide detailed 3-dimensional information on the architecture of cortical and trabecular architecture of ex-vivo bone samples. Recently, also the in-vivo application of a μCT scanner with an appropriate resolution to visualize the trabecular structure of rat bone was introduced [30].

The cortical part of human long bone exhibits cavities (haversian canals) which are occupied by blood vessels, orientated mainly parallel to the bone's long axis. The adjacent bone matrix is aligned in lamellar circumferential orientation around the haversian canals forming osteons (Figure 2.1). Tissue between the osteons is called interstitial bone and also consists of lamellar aligned matrix likely being part of a former osteon which lost its structure according to the remodeling process. Each lamella has a thickness of about $3 - 5$ μm and differs from its neighbors in collagen fiber bundle orientation as discussed below [31, 32].

High resolution imaging revealed an abundant presence of ellipsoid-shaped voids (approximately 13000 mm^{-3}) within the mineralized bone matrix, so called lacunae [34]. These lacunae are interconnected by a dense network of narrow channels known as canaliculi (about $200 - 300$ nm diameter [35]). Already in the middle of the 19th century, structure and align-

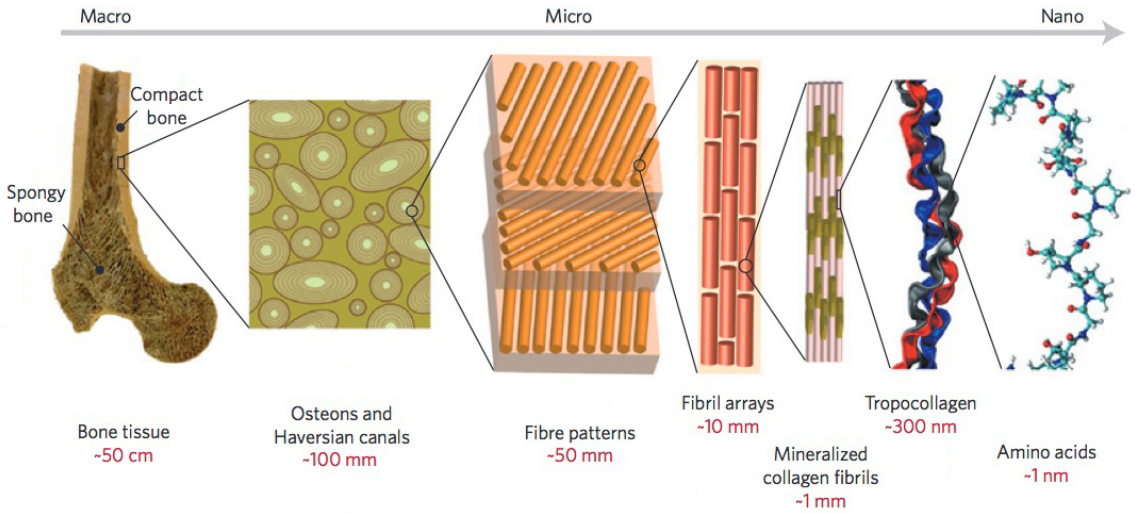

Figure 2.1: Hierarchically organized structure of a human long bone (femur) exhibiting a trabecular structure adjacent to the joints (metaphysis and epiphysis) and compact cortical in the midshaft region (diaphysis). The cortical shows a typical osteonal structure with circumferentially aligned lamellas consisting of fiber bundles with more or less regular orientation. Each fiber is built of mineralized single collagen fibrils. Adapted by permission from Macmillan Publishers Ltd [33].

ment of the lacunae and the canaliculi network were described [36]. Later it was shown that cells called osteocytes, which exhibit long cell processes within the canaliculi, occupy these voids, thus forming a cell network pervading the whole bone tissue. Since the osteocytes are interconnected by gap-junctions, communication or/and molecule transportation through the network are most likely and will be discussed later (Chapter 2.1.4).

On the nanometer level, bone is a unique nano-composite material [25]. The combination of a tough organic matrix consisting of collagen type I, non-collagenous proteins like Proteoglycans, lipids, water, and a stiff crystalline phase of more or less pure Hydroxyapatite (HAP) ($Ca_{10}(PO_4)6(OH)_2$) leads to properties featuring high resistance against cracks and fractures. Collagen fibrils with a thickness of about 100 nm are well aligned but they change their orientation depending on their location [37]. Hence, they form a twisted plywood-like three-dimensional structure [38]. According to the hierarchical structure, each fiber consists of single collagen fibrils as shown in Figure 2.1. HAP crystals are located within collagen chains hardening the tissue to resist mechanical stress and exhibit plate-like dimensions of about $2-7$ nm x $15-200$ nm x $10-18$ nm [25, 39]. To reinforce resistance against sheer forces, divalent and trivalent collagen cross-links are formed during ossification linking adjacent collagen fibers and fibrils.

Despite technical improvements, the characterization of the chemical composition of bone is still challenging, especially if spatial resolution in the μm-range is desired. Due to sophisticated combination of organic matrix and mineral phase, different methods need to be combined for a comprehensive material characterization. Beside others, still much remains

unknown about the local distribution and bindings of minor and trace elements like Magnesium (Mg), Potassium (K), Lead (Pb), Zinc (Zb), Chlorous (Cl), Sulfur (S) and Strontium (Sr). Mg, Pb, and Sr are known to substitute Ca^{2+} ions in the HAP crystal, thus potentially changing the lattice structure [40, 41, 42]. Additional, Mg and Zn are reported to be found in the organic matrix located in the active centers of various enzymes like alkaline phosphatase [43]. S is a minor element that is located in Proteoglycans, which can act as inhibitor of mineralization [44]. Proteoglycans are mainly found in the cartilage tissue, but also in mineralization fronts at sites of new bone formation or (in smaller quantities) in the mineralized bone matrix. Transmission electron microscopy revealed that Proteoglycans are located close to the canaliculi walls, most likely to prevent further mineralization of the voids occupied by osteocytes [45]. Interestingly, Pb and Zn were found to accumulate in the bone tissue at similar regions, but also to much higher amounts in narrow bands in the articular cartilage, the so called tidemarks [46].

The importance of Zn for the alkaline phosphatase enzyme [43] and of Mg for the stabilization of amorphous calciumphosphate phases [47] indicate the importance of these elements during early mineralization. Nevertheless, the process of bone mineralization is still intensively investigated. Much is unknown about the early stages in the formation of organic matrix and HAP crystallization and therefore even less is known about the role of minor and trace elements in the mineralization process.

2.1.2 Bone as a Dynamic Biomaterial

Like most biological tissues, bone is a dynamic material facilitating growth of the individual, fracture healing, repair mechanisms of micro fractures and adaption to mechanical loading. The major actors for these remodeling and modeling processes are the osteoblasts (bone building cells) and osteoclasts (bone resorbing cells). The interplay of these cells is controlled by various communication mechanisms like the RANK - RANKL (Receptor Activator of NFkB Ligand) pathway or WNT signaling, which are extensively described in the literature [48, 49]. The overall bone volume balance can be neutral, positive or negative depending on osteoblast and osteoclast activity [50]. Obviously, during a growth phase a positive balance is needed while it remains almost neutral in healthy adult people. Hormonal changes during aging or in bone diseases often cause a negative balance (e.g. in Osteoporosis). This results in an overall loss of trabecular bone and thinning of cortical bone increasing the susceptibility for fragility fractures [33]. Therefore, to medicate patients with fragile bone, much effort is made to develop drugs to shift bone remodeling from a negative to a neutral or even a positive balance which requires an essential understanding of the remodeling cycle. Bone remodeling appears on the endosteal surface and on trabecular surfaces (both surfaces together are termed the endosteum). Bone modeling occurs throughout life in murine bones on the outer periosteal surface (periosteum). In bigger mammals a remodeling process also occurs inside the cortical, thus forming a system of cannels occupied by blood vessels (Haversian system). Sims et al. lists five phases occurring during remodeling [51]:
After a resting period, where no bone formation or resorption occurs, the activation and resorbtion phase (1) starts. Initiated by systemic hormones (Parathyroid hormone (PTH) or 1,25-dihydroxyvitamin D3) or by mechanical stress sensed by osteocytes, osteoclasts dif-

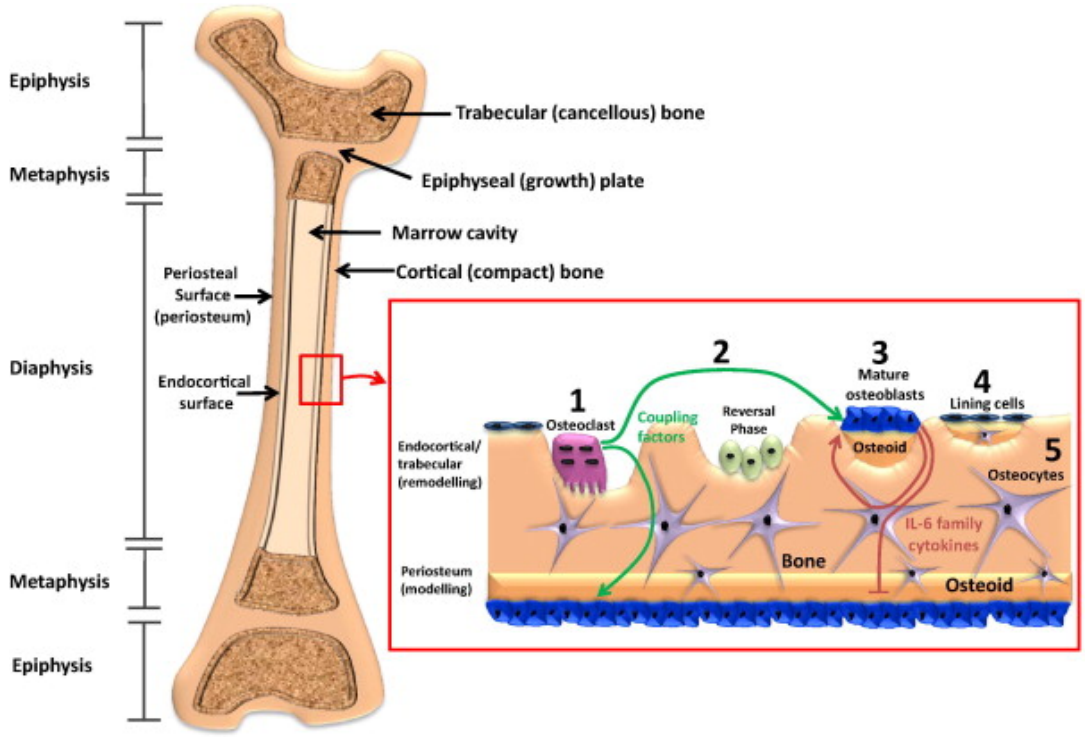

Figure 2.2: Schematic illustration of various anatomical sites of a long bone and the five phases of the bone remodeling cycle; (1) activation and resorbtion phase, (2) reversal phase, (3) bone apposition and osteoblast maturation, (4) osteoblast apoptosis or differentiation, (5) osteocyte maturation; Reprinted from Reference [51] with permission from Elsevier.

ferentiate into multinucleated cells. During bone remodeling osteoclasts attach to the bone surface, solute the mineral phase of the bone matrix, while simultaneously resorbing the organic matrix leaving behind resorption pits or Howship's lacunae and release coupling factors (cardiotrophin-1 and sphingosine-1-phosphate) that stimulate osteoblast differentiation on the endosteal surface. These coupling factors also signal to periosteal osteoblasts, perhaps through the osteocyte canalicular network.
In the following (reversal phase (2)) osteoclasts undergo apoptosis (programmed cell death). Mononuclear cells are then forming a layer rich of Proteoglycans, which will later become the so-called cement line.
After the reversal phase pre-osteoblasts mature, attach to the bone surface and place non-mineralized bone matrix, which mainly consists of type I collagen. This purely organic matrix, called osteoid, has a thickness of approximately 10 μm and rests for about 10 days before the primary mineralization process starts. In this phase (3), HAP crystals are formed through various transient phases, which are yet not fully understood. Within a few days the degree of mineralization reaches about 70 % of the maximum value. That corresponds to roughly 18 weight percent Ca ($wt\%Ca$) [14]. This period of rapid mineralization is followed by the phase of secondary mineralization, that lasts for several months. Finally the Ca concentration saturates (at about 23 to 24 $wt\%$ reported for humans [14]).
In the next phase (4) mature osteoblasts, when their task of producing osteoid is completed,

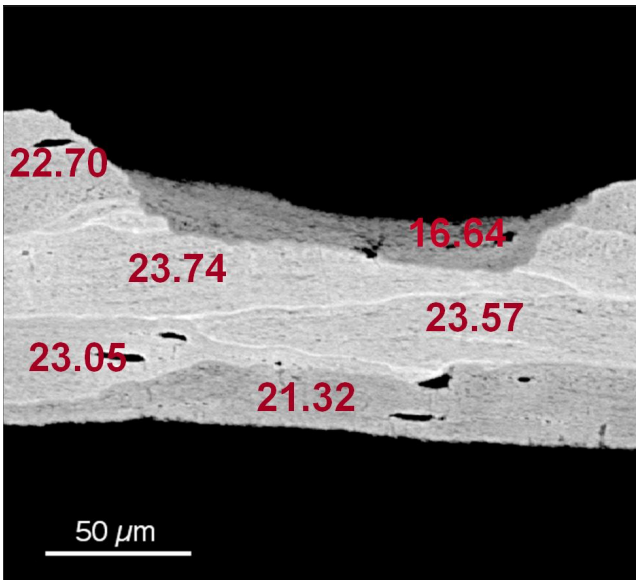

Figure 2.3: Calibrated backscattered electron image (qBEI) showing differently mineralized bone packets. The numbers represent the Ca concentration in $wt\%$ as determined by qBEI. Modified from Reference [25] with permission of the Royal Society of Chemistry.

become lining cells or become encased in the bone matrix differentiating into preosteocytes. The preosteocytes become osteocytes and develop processes which connect to their neighbors and to the bone surface. They start expressing proteins characteristic for the differentiation into mature osteocytes (Sclerostin, RANKL)) during matrix mineralization seems to be specific and highly-controlled (phase 5) [5]. Proteins (e.g. IL-6 family cytokines) are released by the osteoblast lineage and act to stimulate osteoblast differentiation and bone matrix production on endosteal surfaces, but limit osteoblast activity on the periosteum.

As a result of the gradual remodeling processes, bone tissue consists of various bone structural units (BSU) with different tissue age and therefore also of various degree of mineralization as depicted in Figure 2.3. Since remodeling is a continuous process, the entire human skeleton is replaced by new bone matrix in about 10 years [52]. Consequently, it needs to be strictly distinguished between the individual age (depicting the age of the animal or human) and tissue age (corresponding to the age of a defined region of bone material).

Instantly, the question arises how tissue age can be measured. Fortunately an elegant routine was developed to label time points of bone formation using fluorescent dyes like Tetracycline (humans), or Alizerin or Calcein (animals). These fluorochromes are administered typically for 2 times for 3 days in 14 days interval (in adult humans) or are injected with a $1 - 10$ days break (mice) before bone examination[18, 53, 54]. Since these dyes bind to the apatite crystal during the very early stage of mineralization, regions of new bone apposition can be identified using a fluorescent microscope, and even more interestingly they label regions of well known tissue age in the mineralized matrix. A Raman micro spectroscopy routine was developed to set measurements with respect to these labels and also recently backscatter electron microscopy was combined with the tissue age information to gain bone material properties at regions with defined tissue ages [53, 55, 56]. Thus combinations of these methods provide material information independent of bone turnover.

2.1.3 The Early Mineralization Process of Bone Matrix

As mentioned earlier, the mechanical strength of bone is not only determined by bone mass and architecture but also by its material properties [25]. About 21 days (in humans) after osteoblasts laid down a matrix of non-mineralized tissue (osteoid) the early period of bone formation starts [57]. Disturbances in this so-called primary mineralization phase likely impair the mineralization pattern and therefore also the mechanical behavior of the whole bone later on. Hence, the understanding of the chemical processes at and next to active mineralization fronts is crucial for a comprehensive description of the bone material properties and last but not least also for the development of new therapeutic drugs.

The act of calcification in healthy bone is a well-regulated process, which is still part of current research. The osteoblastic formation of non-mineralized osteoid (consisting mainly of collagen type I) provides the basic tissue for mineralization. This soft tissue consists of collagen molecules parallel to the bone surface (Figure 2.4). There is still a discussion whether mineralization starts in the 40 nm wide gap zones or in the tighter overlapping zones of the collagen fibrils [58].

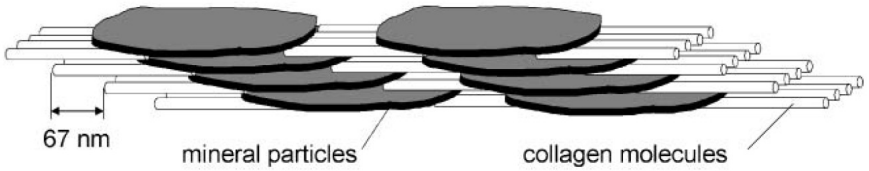

Figure 2.4: Arrangment of the mineral particles ($2 - 4$ nm thickness) in the collagen fibril. The collagen fibrils exhibit a staggered structure with characteristic 67 nm period [25]. With permission of the Royal Society of Chemistry.

HAP precipitation happens in several steps and is thought to start with the formation of about 1 nm small solid units, called Posner's clusters ($Ca_9(PO_4)$) [59]). Aggregation of these clusters leads to spherical amorphous Calciumphosphate particles with a diameter between 20 and 30 nm within the collagen fibrils [60]. Accompanied by a local decrease of the pH-value, phase transitions occur resulting finally in the formation of HAP [58]. Subsequently, the HPA crystals start to grow in a plate-like geometry. This process can be divided into a period of fast (primary) mineralization (< 10 days) and a period of slow (secondary) mineralization until the Ca content reaches saturation [61, 14].

Within the last years the role of so-called matrix vesicles (MV) in biomineralization became subject of extensive discussions. MVs are spherical bodies (diameter: $20 - 200$ nm), which are bud off the plasma-membrane of cells (in the case of bone formation, supposedly osteoblasts or preostecytes) [62]. It is documented that beside others, MVs are enriched in tissue non-specific alkaline phosphatase [63, 62], which is known to be a key enzyme in the hydrolyzation process of pyrophosphate (PPi) increasing the local concentration phosphate (Pi) which is essential for the formation of HAP. Additionally, PPi acts as inhibitor of mineralization [64, 65] and thus increased levels of PPi are associated with mineralization defects in humans (hypophosphatasia) [66] and corresponding animal models [64, 67]. MVs are also supposed to contain

lipids, which might act as mineralization nuclei [62].

Despite the gain of knowledge on the role of MVs in the early stages of bone formation it is still subject of discussion, whether the major role of MV is (i) to secrete proteins, enzymes and inorganic substances to enable the first step of the mineralization process, or (ii) to promote apatite-nucleation already inside the vesicle to subsequently seed them to the organic matrix or (iii) to directly associate with the collagen to initiate matrix calcification [62].

From small angle X-ray scattering (SAXS) and transmission electron microscopy measurements a plate like structure of the crystals with a few nanometer thickness is concluded [68, 69]. However, the reason for the 2-dimensional growth of the HAP remains unclear. A recent study of Xie et al. suspects an interplay of citrate and non-collagenous proteins to determine the crystal shape [70].

2.1.4 Osteocytes and their Role in Bone Mineralization

Already at the beginning of the 19th century the role of osteocytes in the bone and mineral metabolism was subject of speculations [71]. Only within the last years these cells were found to orchestrate bone remodeling and to substantially contribute to the Ca and P metabolism of the whole organism. It was shown that osteocytes express fibroblast growth factor 23 (FGF23); a hormone, that promotes phosphate excretion into urine and thus being part of the phosphate regulation mechanism [4]. Also sclerostin, which is known to be a negative regulator for bone formation, is expressed by osteocytes, inhibiting a pathway that is known to regulate osteoblastic apoptosis rate (Wnt-β-catenin signaling [72, 19]). This mechanism is a target for future strategies for treatments of bone diseases characterized by low bone mass like Osteoporosis or Ontogenesis Imperfecta. The idea for this approach came up when investigating two rare bone diseases: the van Buchem syndrome and Sclerosteosis. Both correspond to mutations in the SOST gene, encoding the previously mentioned protein Sclerostin. These patients exhibit abnormally high bone mass and increased bone length. The fact that no fractures are reported, suggest that no alterations in the bone material quality occur, which lead to an increased bone fragility [73]. Based on this observation, a model of Sost - knockout ($SostKO$) mice with a targeted disruption of the sclerostin coding region was generated resulting in a lack of sclerostin production [74]. Sclerostin antibodies (SclAB) were recently developed deactivating the circulating sclerostin proteins mimicking this mechanism [75, 76]. Consistently, $SostKO$ mice and mice treated with SclAB exhibit a higher bone volume fraction in the cancellous bone, a thicker cortical bone and thus improved mechanical parameters [77, 21].

Beside sclerostin, a protein which is known to be one of the main triggers promoting osteoclastogenesis (RANKL) was detected in the processes of the osteocyte-like (MLO-Y4) cells [78]. The expression of RANKL suggests that using multiple pathways, osteocytes have the potential to influence the balance between bone resorption and formation. Additional to the mentioned proteins, osteocytes express more markers indicating the crucial role that these cells are playing in bone metabolism and also in the hormonal balance of the organism [79].

Several experiments have shown that bone has the ability to react to mechanical stress, thus loading is known to increase bone mass. Osteocytes revealed to have mechanosensoric capabilities. Fluid flow through the lacuna-canaliculi system is sensed by the dendrites and/or the cell body stimulating sclerostin secretion and other pathways [80]. Even if the mechanism is not fully understood, a dense and extensively branched network like the osteocyte lacunae - canaliculi network (OLCN) offers ideal properties for the detection of local changes of fluid pressure caused by strain due to mechanical loading.

Beside the statements above, the question remains, whether osteocytes have the ability to directly interact with the mineralized matrix of their neighborhood. Osteocytes express markers like acid phosphatase and catepsin K which are usually attributed to osteoclasts which use them during bone resorption to solute the mineral and organic phase respectively [81]. Consistently, the Acid Phosphatase and Cathepsin K levels in the osteocytes appeared elevated in lactating mice, most likely to release Ca that is needed for lactation [35]. In that study, it was also indicated that the lacuna size and also the canaliculi diameter were increased in this stage. Beside that work, there are more studies where canaliculi and/or perilacunar matrix exhibits signs of remodeling indicating that osteocytic osteolysis naturally used to resorb and deposit bone matrix at inner bone surfaces [23, 82, 83, 84]. Even if the canaliculi and osteocyte lacunae account for only a minor porosity of the bone, still 60 % of the bone matrix are in 1 μm distance or less to the next canaliculi or osteocyte lacuna [85]. Thus the network features an extensive inner surface of about 1200 m^2 for an adult human individual, that is potentially available to the osteocytes. This is about 100 times larger than the bone surface available to osteoblasts and osteoclasts [86]. Consequently, even small systemic changes of canaliculi dimensions (in the magnitude of 0.1 nm) would have a significant impact on circulating, systemic ion levels [4].

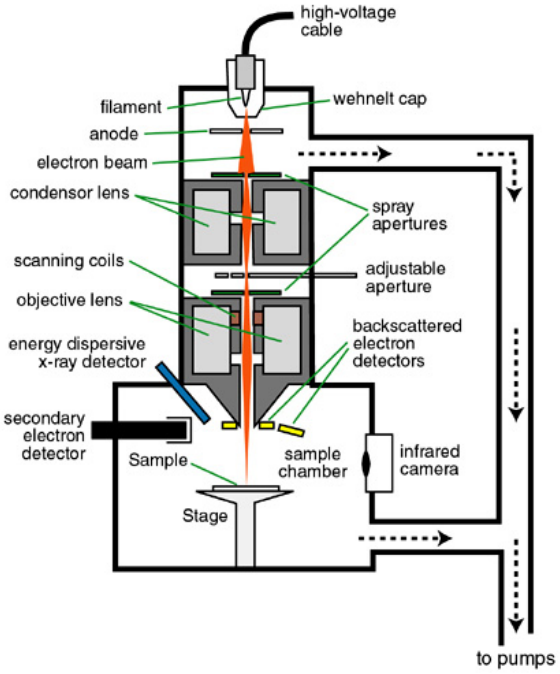

Figure 2.5: Schematic illustration of a scanning electron microscope equipped with a backscattered electron detector, a secondary electron detector and an energy dispersive X-ray detector: The primary beam, emitted by the cathode, is guided through a set of lenses and apertures to be focused on the samples. Scanning coils account for precise beam deflection. Reprinted from Reference [89] with kind permission from James H. Wittke.

2.2 Physical Characterization Techniques of Bone Tissue

2.2.1 Quantitative Backscattered Electron Microscopy (qBEI)

Experimental setup

Figure 2.5 shows the schematic setup of a scanning electron microscope, enabling qualitative and quantitative analysis of bone architecture, material composition and tissue organization with micrometer resolution.

In general there are three different types of electron sources (filaments) (Figure 2.6). Tungsten hairpin cathodes, Lanthanum Hexaboride filaments (LaB_6) or field emission cathodes are most often used, featuring various properties in terms of beam geometry, electron current, beam stability, lifetime and financial costs. The tungsten hairpin cathode is the first filament type applied for SEM, but is still used due to its low costs and tunable emission current. As the bias voltage determines the region of electron emission, it can be used to tune the emission current and the focus size can be set to an optimum. The typical lifetime reaches from 40 to 100 hours and the costs are low compared to other cathode types [87, 88].

State of the art filament types are field emission electron guns made of tungsten, but often coated with zirconium to reduce the work function of the electrons. These filaments exhibit a sharp tip with a diameter of 100 nm or less providing high field strength. This combined with the well defined spot of electron emission, leads to a small focal spot despite a high current density of about 10^5 A/cm^2 (tungsten hairpin cathodes: ≈ 3 A/cm^2) [88]. For this filament type, high beam stability and favorable beam characteristics are opposed by increased vacuum requirements and financial costs of cathode material and replacement.

After the electron extraction at the cathode, the beam is guided through a system of apertures, electric and magnetic lenses and coils for beam deflection that varies according to the desired properties of the final electron probe. Usually, an aperture wheel provides an adjustable electron current, which can be fine-tuned by varying the voltage at the extractor pinhole. The high voltage lies between 5 and 30 kV for most applications and must be chosen with respect to the desired image contrast, sampling volume, energy deposition and tolerable beam damage.

Scanning electron microscopes are usually operated in vacuum. Depending on the cathode type ultra high vacuum (around 10^{-10} $mbar$) in the gun chamber may be needed while high vacuum (10^{-6} $mbar$) is most often appropriate for the system vacuum. Specialized systems also allow measurements at environmental conditions in the sample chamber.

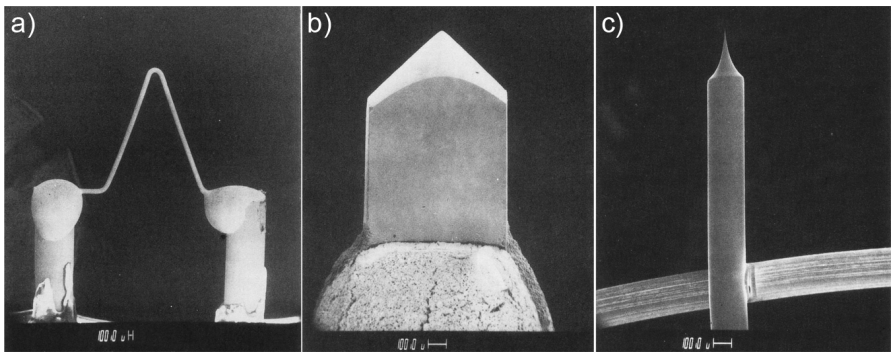

Figure 2.6: Common types of electron sources: secondary electron images a tungsten hairpin electron gun (a), a LaB_6 cathode (b), and a field emission electron gun (c); Reprinted from Reference [88] with permission from Springer-Verlag GmbH.

Generated signals

Electronic bombardment causes different types of outgoing signals, which can be measured using appropriate detectors. Backscattered electron detectors are often mounted in a ring-design around the primary electron beam next to the pole piece to measure the flux of emitted high-energy electrons after elastic scattering at the sample (Figure 2.7). In contrast, secondary electron detectors are designed to collect the low-energy electrons, which escape the sample after inelastic scattering thus providing information on the surface topology. Additionally, an energy dispersive X-ray system (EDX) may be used for chemical sample composition analysis by detecting the characteristic X-rays, which are emitted after atomic excitation due to the interaction of the primary beam electrons with the electron shells of the target material. In general the resolution and the quality of the gained signal depends on various parameters, namely the diameter of the primary electron beam, the penetration depth of the electrons (and thus the primary electron energy) the pixel size of the digital image, electron flux and counting statistics, beam damage, and instrument stability.

Fundamental knowledge of the physics of the electron - matter interactions is crucial in order to interpret the outgoing electronic and electromagnetic signals (Figure 2.8). Figure 2.9 shows a Monte Carlo simulation with parameters, similar to our measurement setup (20 kV

Figure 2.7: Photo of the vacuum chamber of a Zeiss Supra 40 SEM (Oberkochen, Germany). The backscattered electron detector is placed in a ring design below the pole piece while the energy dispersive X-ray detector and secondary electron detector are mounted laterally.

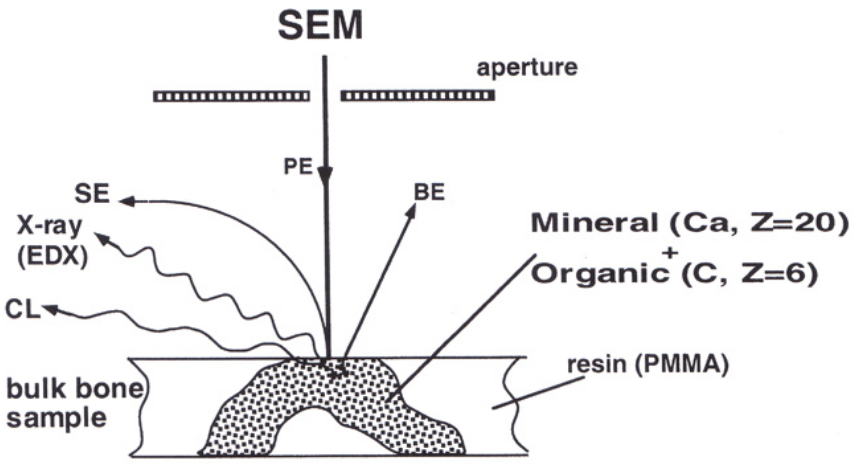

Figure 2.8: Overview of the outgoing signals caused by primary electron (PE) bombardment of an embedded bone sample. High-energy backscattered electrons (BE), low-energy secondary electrons (SE), as well as X-rays and cathodoluminescence radiation (CL) can be detected to characterize sample composition and topology. Reprinted from Reference [90] with permission from Paul Roschger.

acceleration voltage, bone-like target material). While the information depth of SEs is only around 10 nm, BEs also escape from deeper below the sample surface, providing a distinctly higher information volume. The escape probability of characteristic X-rays produced after inner-shell ionization of the target material depends on photon energy and thus its attenuation on its way to the sample surface. For the $Ca - K_\alpha$ line the information depth is estimated to be around 5 μm [90].
In the following the origin of these signals is discussed. Further information can be found in the literature (e.g. see Reference [88]).

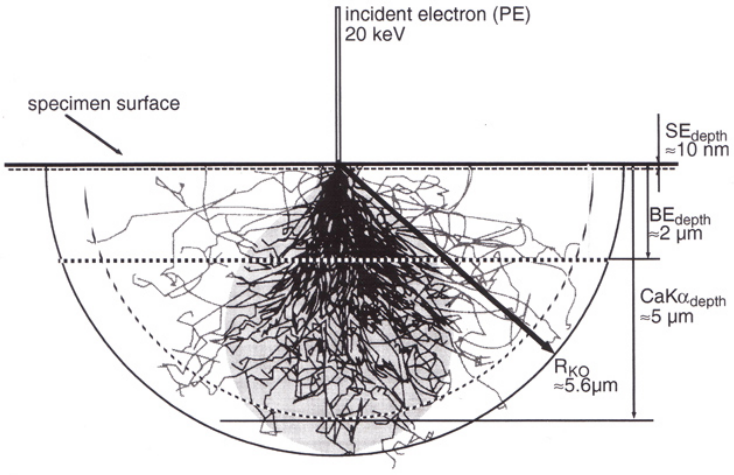

Figure 2.9: Monte Carlo simulation of electron trajectories calculated for a bone-like material. Information depths are marked for SE_{depth} (secondary electrons), BE_{depth} (backscattered electrons) and $CaK\alpha_{depth}$ ($CaK\alpha$ - X-ray line). R_{KO} is the radius of the semi-sperical Kanaya-Okyama electron range. Reprinted from Reference [88, 90] with permissions from Springer-Verlag GmbH and Paul Roschger.

- **Backscatter Electrons** (BEs):

  Elastic scattering of the electrons occurs when a scatter event leads to a change of an electron's trajectory, accompanied by only a minor loss of energy. After a cascade of multiple scatter events (involving mainly angles less then 90°), some of the primary beam electrons are able to escape the sample surface, still carrying energy just below that of the primary electrons. With increasing acceleration voltage, these backscattered electrons manage to escape the sample surface also from a distinct distance to the impinging spot, thus impairing the spatial resolution (Figure 2.9). The percentage of electrons sustaining high-angle scattering processes and further escaping the sample after a single-scatter event is low compared to those with multi-scatter events [88].

  The parameter η is introduced, to describe the yield of BEs. η denotes the ratio between the numbers of BEs ($n_B E$) and primary beam electrons n_B [88]. Fortunately for our

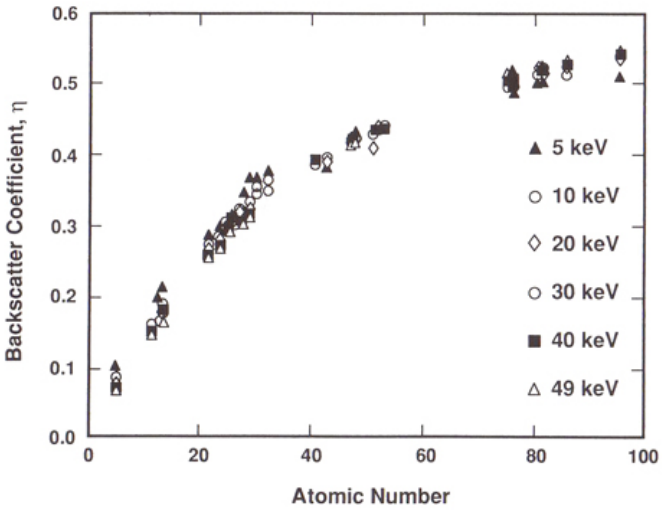

Figure 2.10: η as a function of the atomic number of the target material at different primary beam energies. While there is a distinct Z dependency, the same η values are observed for all acceleration energies. Reprinted from Reference [88] with permission from Springer-Verlag GmbH.

analysis, η strongly depends on the electron density, and thus on the average atomic number (Z) of the target material (Figure 2.10).

For samples with atomic numbers below 20, a linear relationship between Z and η is observed. Since bone mainly consists of HAP ($Z \approx 13.9$) and organic matrix ($Z \approx 6.5$) ([91]), a linear approximation seems to be adequate for all mixtures of HAP and organic matrix, which can be used for a quantitative analysis of bone as introduced by [92] and [93]. Surprisingly, η is independent on the energy of the primary beam electrons. This is supposed to be the result of two adverse effects, namely, the higher energy and thus the higher probability for electrons to escape the specimen according to a decreased stopping power, and on the other hand, the increased penetration depth of the electrons decreasing the number of electrons reaching the sample surface after scattering [88].

- **Secondary Electrons** (SEs):

  In contrast to elastically scattered BEs, SEs are caused by scatter events where a loss of energy occurs due to the production of characteristic X-rays, Auger electrons, Bremsstrahlung and others. Typically SEs, that escape the sample have an energy of only $2 - 50\ eV$ [88]. For these low-energy particles, the stopping power is increased distinctly, resulting in a very low information depth for SEs as shown in Figure 2.9. Only electrons of the first nanometers below the surface might leave the sample, thus reducing the escape depth of the electrons to roughly 1/100 of escape depth of BEs. Consequently, the SE signal is perfect to image surface topology in high resolution. The dependency on the atomic number of the target material is much less pronounced compared to BEs. Nevertheless, Seiler et al. were able to show that the composition dependent contrast of the secondary electron signal can be enhanced using a high-vacuum chamber and an in situ sample cleaning system [88], [94]. In contrast to BEs the SE yield increases with decreasing acceleration voltage. This is due to increased production of SEs near the surface [88].

Quantitative backscattered electron imaging (qBEI)
Using backscattered electron microscopy Boyde et al. suggested to use the Z-dependency of the backscattered electron yield to identify regions with different mineralization [92]. P. Roschger et al. extended this approach and established a routine to calculate the calcium concentration based on the measurement of the average Z, thus introducing the method of qBEI [95]. Some assumptions like the homogeneity of the interaction volume, the apatite composition and the atomic number of the organic matrix were made, which revealed to be appropriate in a validation study where the qBEI method was compared to energy dispersive X-ray analysis data of reference materials [93].

In the calibration routine, which needs to be performed for each measurement, Aluminum (Al) and Carbon (C) standard reference materials are used to adjust image brightness and contrast in a predefined way. In the case of the two devices used in our studies, the gray level in the 8-bit image of Al is set 225 and the carbon peak to 25 [93]. As long as the working distance remains constant, and monitoring of specimen current, detector stability and cathode parameters indicates stable measurement conditions, a fixed correlation between BE flux (represented by the gray value in the qBEI images) and the average atomic number are warranted. The further conversion to the local Ca concentration ($wt\%Ca$) corresponds to Formula 2.1 [93].

$$wt\%Ca = 0.1733 \times GV - 4.332 \tag{2.1}$$

While statements regarding the average atomic number of the target material are most reliable, for the conversion of gray values to $wt\%Ca$ one must keep in mind that changes in the atomic numbers of the organic matrix or fundamental changes in the mineral composition might cause systematic errors.
Based on Formula 2.1 qBEI images can be used to gain the bone mineralization density distribution (BMDD) correlating each gray value (and therefore the $wt\%Ca$ value) with its frequency of appearance in the analyzed image [93]. An example of such a histogram is shown in Figure 2.11.

Since the conversion from the image to the histogram causes a loss of spatial information of the mineral distribution, the BMDD curve reflects a fingerprint of the mineralization pattern. Thus it can be used for its characterization and comparison with other samples and individuals. As illustrated in Figure 2.11 the BMDD histogram is characterized using 5 parameters [12]:

- Ca_{Peak}: most frequently measured Ca concentration
- Ca_{Mean}: weighted mean Ca concentration
- Ca_{Width}: full width at half height of the distribution
- Ca_{Low}: percentage of bone area which is less mineralized than 17.68 $wt\%Ca$
- Ca_{High}: percentage of bone area which is higher mineralized than 25.30 $w\%Ca$

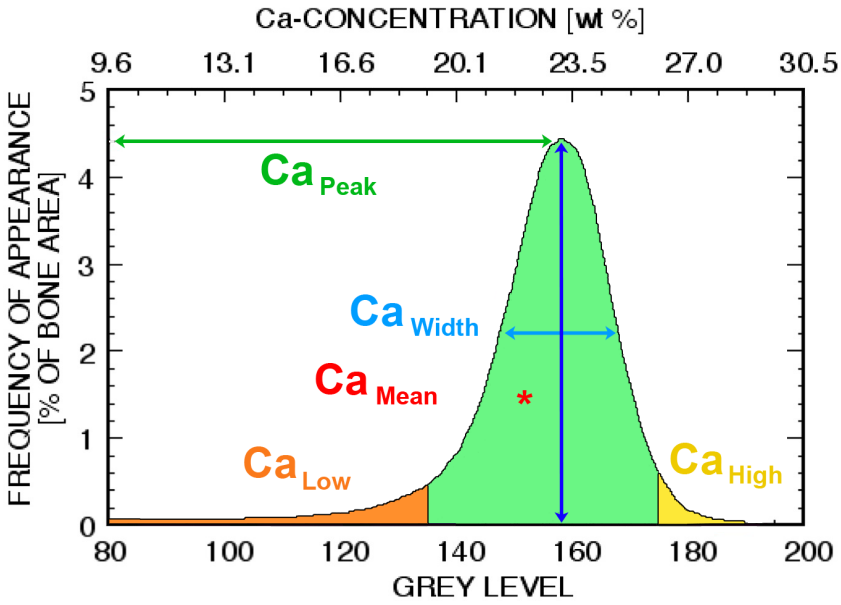

Figure 2.11: Example of a BMDD histogram. The five parameters Ca_{Peak}, Ca_{Mean}, Ca_{Width}, Ca_{High}, Ca_{Low} are used to characterize the distribution.

While Ca_{Peak} and Ca_{Mean} carry information on the degree of mineralization, Ca_{Width} becomes smaller the more homogenous the mineralization pattern is. Hence, this parameter can be seen as a measurement for the heterogeneity of mineralization. The cut-off values for Ca_{Low} and Ca_{High} are chosen with respect to the 5 % and 95 % percentile of an average BMDD originating from cancellous regions of healthy adult people [14]. The evaluation of BMDD revealed to be a powerful tool for the characterization of bone turnover effects on mineralization, and (maybe even more interesting) the description of pathological mineralization disturbances in humans [96, 97, 98, 14, 99] and in animal models [21, 100, 101, 102].

2.2.2 Energy Dispersive X-ray Analysis (EDX)

Beside the generation of BEs and SEs as discussed in Chapter 2.2.1, the interaction of electrons with matter also involve the emission of X-rays which can be used for a spatially resolved elemental analysis. The observed X-ray spectrum consists of two different components. The Bremsstrahlung, a continuous spectrum consisting of radiation produced due to the deceleration of the electrons in the sample, and electron-induced X-ray fluorescence (characteristic radiation), which is caused by electronic transitions.

Electronic transitions

In case of characteristic X-ray emission, the energy of the emitted photon E_{ph} corresponds to the difference of the involved energy shells E_i and E_f (Formula 2.2). The Bohr model of atoms describes the electronic shells as discrete energy levels. High-energy photons as used in an SEM are able to ionize the atoms of the target material by direct electron-electron interaction. If an inner shell electron is punched out, the atom remains in an excited state

followed by an electronic transition from an outer shell (higher energy level) to an inner one (lower energy level), which is accompanied by a release of energy in the form of the emission of an X-ray quantum or an outer shell electron, a so called Auger electron. In the first case the emitted photon with the energy E_{ph} might be able to leave the sample contributing to the spectrum of characteristic X-ray radiation. E_{ph} equals the energy difference between the initial and the final shells E_i and E_f.

$$E_{ph} = h\nu = E_i - E_f \tag{2.2}$$

The fact that the potential energy of the electron shells strongly depend on the charge of the core and thus on the chemical element, allows us to assign the energies of the measured photons to the elements present in the target material. Since the intensity of the outgoing photon flux corresponds to the element concentration, in the quantification routines this can be used to derive the composition of the sample.

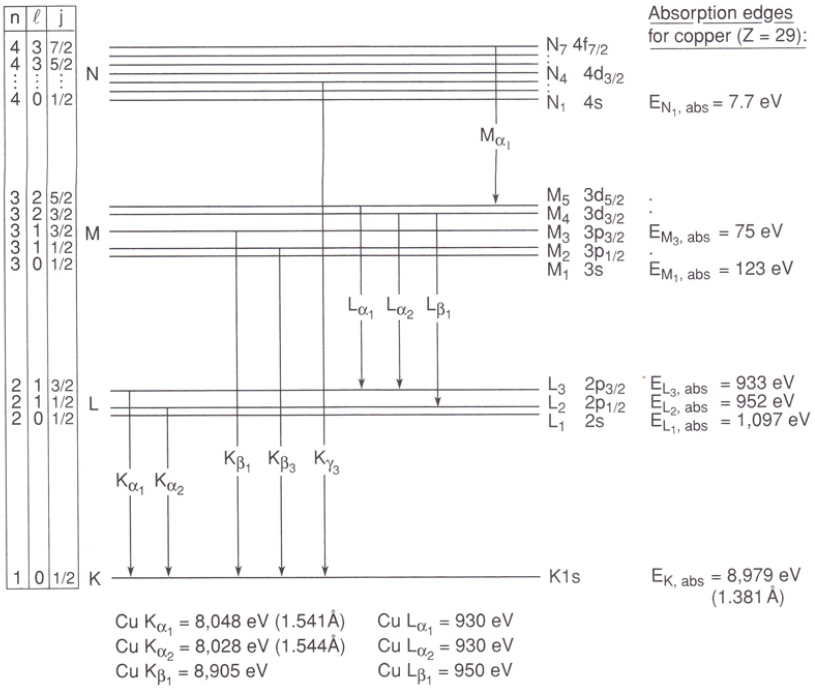

Figure 2.12: Allowed electronic transitions and corresponding X-ray energies of a Cu atom. The energy levels split according to the quantum numbers n, l, j. Reprinted from Reference [103] with permission from Cambridge University Press.

Figure 2.12 shows the electronic energy levels for Copper (Cu) and the possible transitions. The main shells (K, L, M, N,...) split into $2n + 1$ subshells and can be characterized by the quantum numbers n, l and j. All electron transitions with the K shell as their final state are summarized to the K-series, consisting of multiple K_α lines, K_β lines, and so on, depending on the initial shell of the transition electron. In practice, it cannot be distinguished between the various contributions of the subshells due to the limited energy resolution of the detector, but they contribute to broadening of the peak. It must be noted that not all transitions are

probable due to selection rules of dipole transitions:

1.)$\Delta j = 0, +1, -1$
2.)$\Delta l = +1, -1$

Quantification
These rules can be used to estimate the relative peak intensities of α, β and γ lines which are often well-separated, thus helping to identify the present element if there are energy overlaps in the spectrum. Quantification of the present elements based on the X-ray spectra is still a challenging topic, especially if there is only minor prior knowledge of its composition. Most quantification routines take matrix effects, X-ray attenuation, various information depths and sample coating into account. But there are still a couple of light elements, which are hard to detect reflecting unknown components which might cause errors in the quantification. Additionally, all routines assume a homogenous elemental distribution within the information volume (despite the presence of coating which can be considered) and also a flat sample surface. Adulterations in the quantitative results are most likely if these requirements are not fulfilled. Nevertheless, qualitative comparisons of minor elements between different regions of similar composition are most reliable even if the concentrations are close to the detection limit.

Restrictions
Emission of fluorescence photons and the emission of Auger electrons are two competitive processes and both signals provide information on the atomic number of the involved element [88]. As shown in Figure 2.13 there is a strong dependency of the X-ray yield ω_K on the atomic number after K-shell ionization. While for $Z < 30$ the majority of exertation energy is released according to the emission of Auger electrons, the X-ray production is favored for higher atomic numbers [104]. As for our analysis of bone, all elements have an atomic number distinctly below 30, this competition limits the X-ray flux that can be used for an elemental analysis.

From a technical point of view, the maximum resolution is determined by the primary electron beam energy (typically around 10 keV) and the element of interest. The former defines the interaction volume in the sample, thus lower energies lead to a smaller depth of penetration and thus to increased resolution. On the other hand one should keep in mind that X-rays emitted by light elements like O have distinctly less energy compared to more massive elements. Due to the strong dependency of the linear attenuation coefficient μ_L on the X-ray energy, the depth of information increases with the energy of the fluorescence radiation, thus reducing the spatial resolution (Formula 2.3).

$$I(X) = I(0)e^{-\mu_L x} \tag{2.3}$$

2.2.3 Raman Micro-Spectroscopy

Within the last years the application of spatially resolved vibrational spectroscopy (like Raman micro spectroscopy and Fourier transformed infrared spectroscopy) on bone tissue increased remarkably. Their ability to gain manifold information on the chemical composition of the

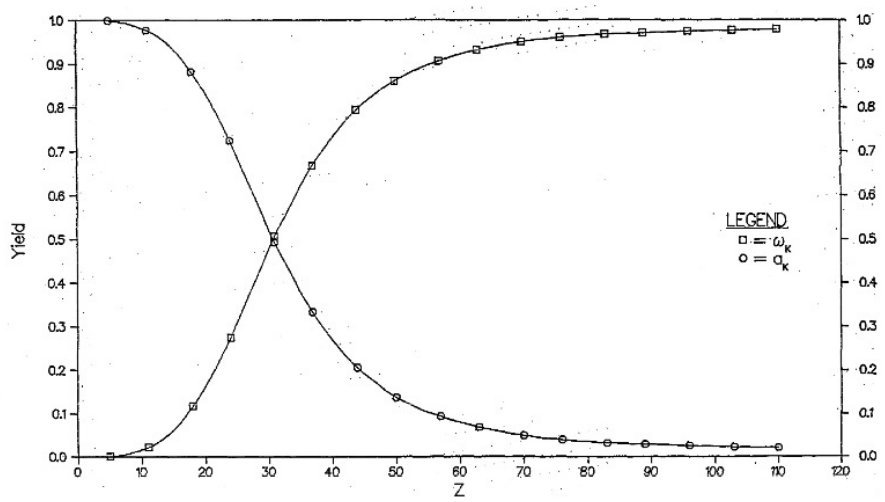

Figure 2.13: X-ray fluorescence yield ω_K and Auger electron yield σ_K depending on the atomic number of a target material. Reprinted from Reference [104] with permission from AIP Publishing LLC.

sample in a non-destructive way, contributed significantly to the understanding of composition and organization of the organic and mineral constituents of bone.
In contrast to X-ray fluorescence as described above, Raman spectroscopy makes use of electromagnetic radiation ($\Delta E = E_i - E_f = h\nu$) emitted after vibrational transitions of the target's molecules.

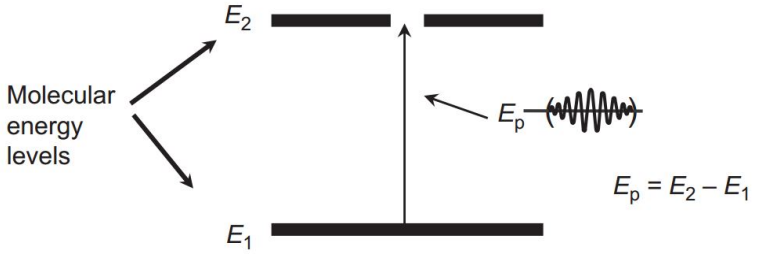

Figure 2.14: Illustration of molecular energy absorption with a primary laser energy E_P: Photons with at least the energy $E_p = E_2 - E_1$ have the ability to excite the molecule to a higher energy state. Reprinted from Reference [105] with permission from Elsevier.

The excitement to transient vibrational stages can be described classically as done in Reference [105]. An external electromagnetic field (E, incident laser beam) induces a dipole moment (μ) according to formula $\mu = \alpha E$ with α depicting the polarizability. Since both E and α can vary in time, the amplitude of the resulting dipole moment is most likely not constant but modulated due to the superposition of these two components. Splitting the time dependency of the resulting μ into its steady-amplitude components provides an illustrative description of Rayleigh, Stokes and anti-Stokes scattered radiation as shown in Figure 2.15.

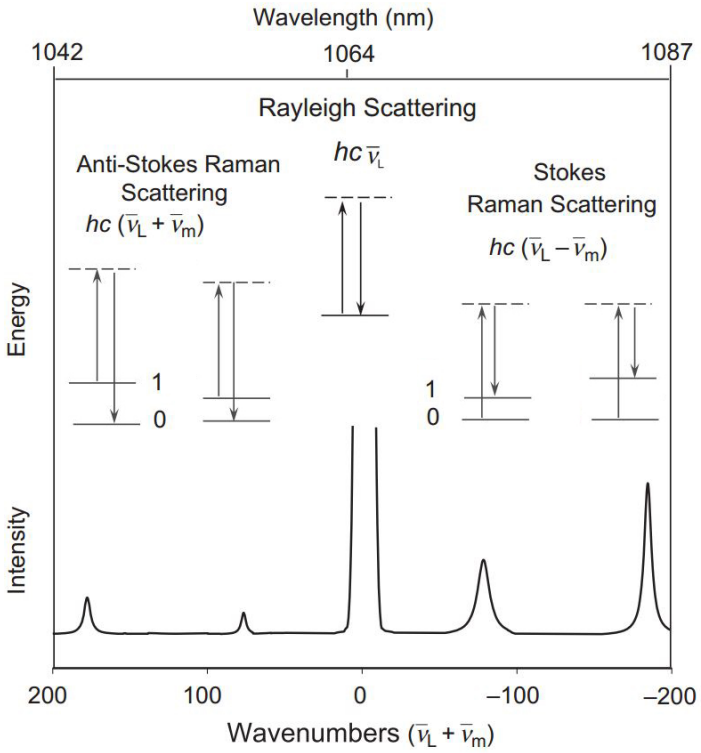

Figure 2.15: Illustration of Stokes and anti-Stokes scattering: ν_L depicts the excitation frequency (upward arrows) while the downward arrows represent the scattered photon energy, which remains unchanged for Rayleigh scattering. Dashed lines indicate virtual states. Reprinted from Reference [105] with permission from Elsevier.

Vibrational modes

The vibrational frequency of the molecule ν and a possible not-induced molecular dipole moment (which is not included in this simple description) are different for various molecules. The resulting energy levels E_i and E_f and consequently also the transition energies between these levels ($\Delta E = E_i - E_f$) are characteristic for the molecule composition.
Due to the considerations made above, the analysis of the gained Raman spectrum provides information on the present vibrational energy states and therefore on the molecules present in the sample. The number of possible vibrational modes of a molecule is linked to its degrees of freedom (n) and amounts to $3n - 6$ modes for non-linear molecules (like H_2O) and to $3n - 5$ for linear molecules (such as CO_2). Not all of these vibrations can be observed in the Raman spectrum, but therefore the analysis of the absorption spectrum of the primary beam provides complementary information as done in infrared spectroscopy. In general, symmetric or in-phase vibrations of non-polar groups can be studied by Raman while asymmetric or out-of-phase vibrations of polar groups are most easily studied by infrared spectroscopy [105].

Raman spectra consist of peaks of higher (anti-Stokes scattering) and lower (Stokes scattering) wavelengths compared to the coherent (Rayleigh) scattered primary beam as illustrated in Figure 2.16. Rayleigh scattering is most probable (about a factor 10^{-3} smaller then the excitation intensity) while this factor is about 10^{-6} for Raman scattering. Usually, peaks in the Stokes spectrum are more intense compared to the anti-Stokes region, but the exact ratio depends on the occupation of thermally excited states and thus on the temperature. A classical description of the Raman scattering process can be found in [105] and [106].

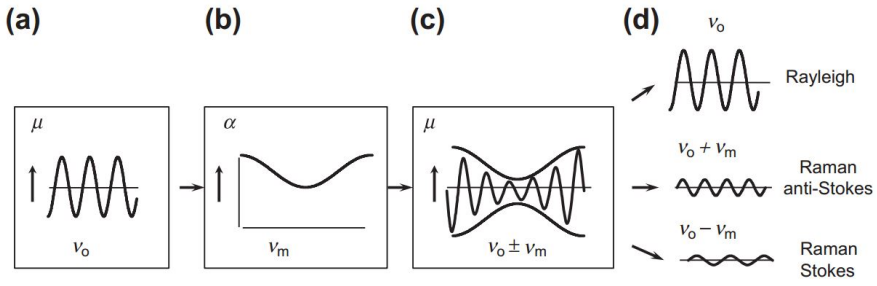

Figure 2.16: The classical scheme shows the induced dipole moment μ caused by and external electromagnetic field (a), the induced variation of the polarizability α (b), and their superposition (c). In (d) the contributions of steady amplitudes are shown, splitting the vibration into their three relevant components. Reprinted from Reference [105] with permission from Elsevier.

Peak intensities

The intensity of a peak in the Raman spectrum is proportional to the number of the corresponding vibrational units. Hence, intensity differences of a certain peak area between different locations or samples correlate with concentration of the number of contributing bindings, thus allowing a semi-quantitative analysis. Deriving quantitative information of the presence of certain molecules is much more complicated, because every vibrational mode has its characteristic Raman tensor, which is linked with the yield and the polarization of the emitted photons. Raman tensors might be modified by their chemical environment, thus making their general descriptions difficult. The Raman scattering intensity I_s is given by Formula 2.4 if a single or multiple molecules are taken into account [107].

$$I_s = I_0 \left| \vec{l_{g'}} \alpha' \vec{l_g} \right|^2 \quad \text{and} \quad I_s = I_0 \sum \left| \vec{l_{g'}} \alpha' \vec{l_g} \right|^2 \tag{2.4}$$

l_g and $l_{g'}$ are the direction cosines of incident and scattered beam respectively (g and g' signify the polarization), and α' is the Raman tensor of a certain vibration. Figure 2.17 shows a typical Raman spectrum for bone.

As used for the studies in this thesis the development of confocal Raman micro spectroscopy facilitates high lateral resolution ($< 5\ \mu m$), depending on the used optics. For further information see Reference [108]. This setup features the combination with other non-destructive on-Block methods like confocal laser scanning microscopy (CLSM), backscattered electron microscopy, energy dispersive X-ray analysis, nano-indentation and others. Especially establishing a routine for Raman measurements between fluorescent labels as introduced in Chapter 2.1.2 opened great possibilities for an advanced interpretation when comparing the same tissue age of different samples. Beside the *mineral/matrix* ratio as discussed below, also parameters linked to Proteoglycans, Lipids, PMMA, and other can be obtained [109].

The *mineral/matrix* ratio

The *mineral/matrix* peak area ratio is frequently used to characterize matrix mineralization.

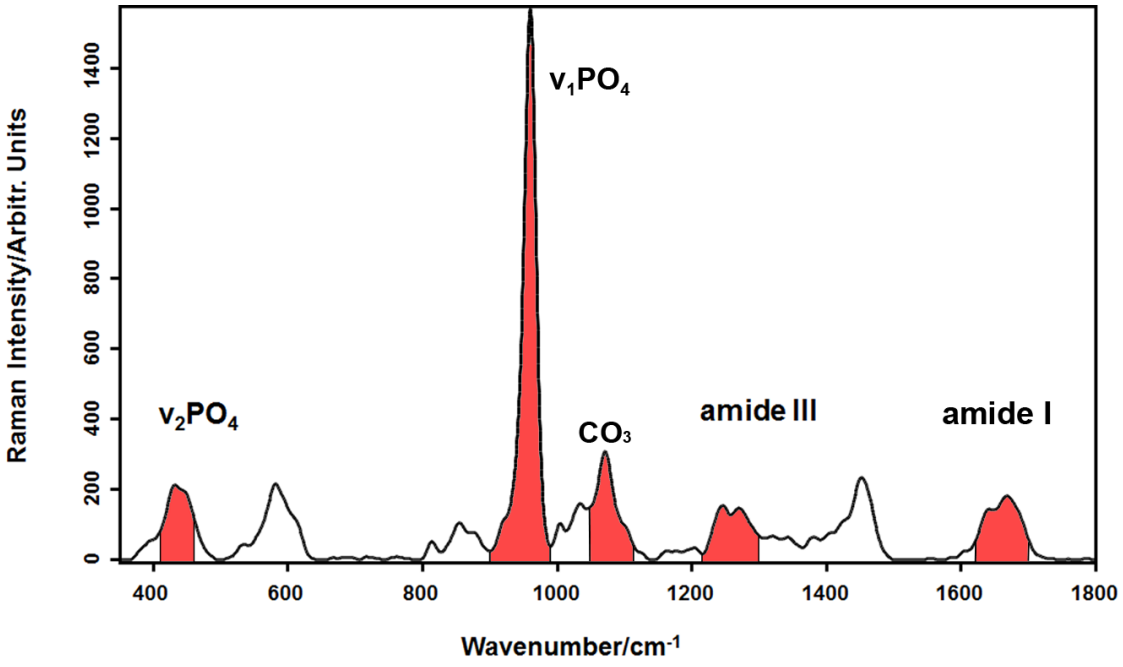

Figure 2.17: Example of a typical Raman spectrum obtained in mineralized bone tissue. Peaks related to the mineral phase (PO_4) and the organic matrix (*amide*) are labeled. The CO_3 peak is linked to Carbonat substitution.

The correlation of this parameter with the qBEI outcome is in the focus of a recently published study performed in the frame of this thesis ([46], Chapter 4.1). Hence, it is reasonable to have a closer look to the nature of this parameter.

The term *mineral/matrix* denotes the ratio of integrated peak areas under Raman peaks caused by a vibrational mode of the PO_4 group like the $\nu_1 PO_4$ peak at a wavelengh of 961 cm^{-1}) or $\nu_2 PO_4$ (430 cm^{-1}) or ($\nu_4 PO_4$ 589 cm^{-1}) and one of the amide bands representing the organic matrix ($amideI$ ($1620 - 1700$ cm^{-1}) or $amideIII$ ($1240 - 1320$ cm^{-1})) [15]. Hence, *mineral/matrix* is a parameter frequently used to characterize matrix mineralization and to describe alterations in bone material quality [110, 82, 111, 112]. Also a combination of Raman micro spectroscopy and fluorescence microscopy was established to place measurement points between fluorescent labels as introduced in Chapter 2.1.2, providing normalization for tissue age and thus allowing more precise interpretation independent of bone turnover [55, 53, 56, 113].

In previous studies the orientation dependency of the peaks corresponding to the PO_4 groups was analyzed systematically in human osteonal bone. It was shown that the peak intensity, corresponding to the $\nu_1 PO_4$ stretching vibration, strongly depends on the orientation of the bone lamellas and therefore on the alignment of the collagen fibrils. In contrast no orientation dependency was observed when examining the $\nu_2 PO_4$ and the $\nu_4 PO_4$ Peaks [114].

Since the predominant part of PO_4 is bound to HAP crystals, the intensity of the correspond-

ing peaks is linked to the amount of HAP present in the measurement volume. Amongst others, deviations might be due to type B carbonation when CO_3 groups substitute PO_4. This is expected for about $2-5$ % of HAP present in human bone [115].

The *amideI* and *amideIII* peaks can be used to characterize the collagen matrix. The *amideI* peak is associated with the $C=O$ double binding (present in the peptide groups of collagen and other organic constituents) and involves mainly stretching of the carbonyl group [16]. According to its orientation dependency, this vibration offers the ability to study the alignment of the collagen fibrils by using a linear polarized excitation beam. In contrast to that, the *amideIII* peak is caused by a stretching vibration of the $C-N$ in combination with a $N-H$ binding vibration of a peptide group. Opposing polarization contributions of perpendicular and parallel components of the *amideIII* peak yield to orientation independent results when analyzing the whole peak [114]. As done for our study, this spectral region can be used if an influence from the collagen alignment is not desired.

In general, the intensity of the Raman peaks is correlated with the number of vibrational units (in our case mainly PO_4 or $C-N$, $N-H$ groups) in the measurement volume. Factors, like orientation dependency, matrix effects, inhomogeneity of sample composition, fluctuations in laser intensity or wavelength and unknown detector characteristics complicate a quantitative analysis. Additionally, as discussed above, the estimation of the Raman-tensors (describing the response of a certain vibrational unit) is not trivial. The Raman-tensor of the *amideI* band is well documented for the trans peptide group of an aspartame single crystal and there is evidence that it hardly changes when the peptide group is incorporated within a long alpha helix, as present in collagen [116]. Tsuboi et al. also investigated the Raman tensor for the *amideIII* vibration using an aspartame single crystal [116], but to the best of our knowledge there are no further studies on the transferability to polypeptides as they occur in the collagen matrix of bone. Concerning the mineral phase, there was no appropriate documentation of the PO_4 Raman tensor found in the literature. According to the complexity of a quantitative analysis, peak area ratios are more suitable to characterize and compare bone samples. Hence, for our studies, the orientation independent $\nu_2PO_4/amideIII$ integrated peak area ratio ($mineral/matrix$) was used. The considerations made above confirm that the mineral/matrix ratio provides a robust orientation-independent parameter when using the $\nu_2PO_4/amideIII$ bands characterizing bone mineralization with a resolution of about $< 5\ \mu m$ when using in a micro spectrometry device.

2.2.4 Confocal Laser Scanning Microscopy (CLSM) of Stained/Labeled Bone Samples

The introduction of fluorochromes to characterize bone material offered new possibilities to gain dynamical histomorphometric parameters as already established in a large number of laboratories for routine-analysis. Recently developed applications exceed these standard analysis methods thus allowing imaging of three dimensional structures or to make use of the fluorescent signal to predefine measurement regions for other methods. Modern CLSM systems provide great advantages in terms of image contrast and spatial resolution compared to con-

ventional fluorescent microscopes. Contrary to conventional microscopes, these devices use lasers with different wavelengths as light sources, and a confocal setup assures a defined measurement volume in x, y and z direction.

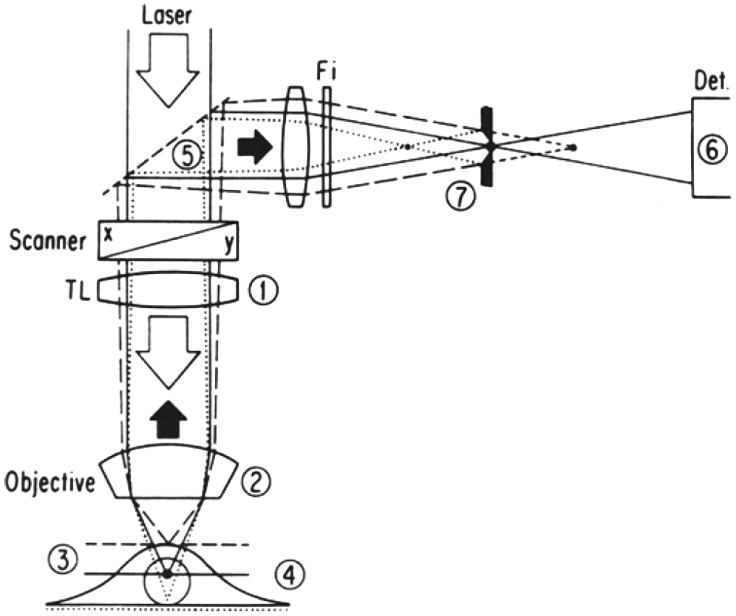

Figure 2.18: Illustration of the beam path in a confocal laser scanning microscope: (1) filter (2) objective, (3) out-of-focus layer, (4) in-focus layer, (5) beam splitter, (6) detector, (7) pinhole; Reprinted from Reference [117] with permission from Springer-Verlag GmbH.

Technical setup

Figure 2.18 illustrates the beam path in a CLSM. The beam-splitter (5) can be designed as a simple half reflective mirror or a wavelength sensitive mirror optimizing illumination and detection properties. The objective lens focuses the beam on the sample. According to the confocal setup, the emitted signal is guided back to the beam splitter and further focused with a convex lens on a pinhole plane (7). The measurement setup is executed in a way, that the focal plane at the pinhole represents the desired focal plane on the sample (4). Thus, signals that originate from sample regions below or above (3) the focal plane are projected in front of or behind the pinhole plane. Consequently, the pinhole size defines the information volume and thus the origin of the florescent radiation that is further processed at the detector. In a CLSM usually one or more photomultipliers are used as detectors exhibiting an acceptable sensitivity (about 40 % quantum efficiency), high countrate processing capabilities and therefore good signal to noise ration.[117]

Resolution

To find the optimal compromise between high spatial resolution and signal to noise ratio, besides setting laser intensity and detector gain (voltage applied in the photomultiplier). The adjustment of the pinhole size is crucial as follows. The lateral resolution is defined as the smallest distance between two points, that still allows identifying them as separate objects.

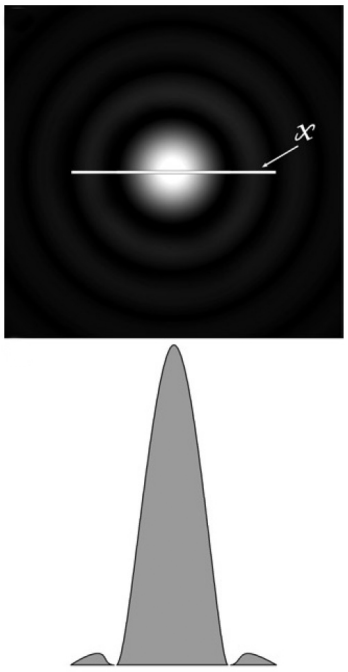

Figure 2.19: Intensity pattern after diffraction. The Airy 1 pinhole setting cuts the distribution at its first minimum, thus giving a compromise between intensity and resolution. Reprinted from Reference [118] with permission from Elsevier.

Lateral image blurring due to diffraction can never be fully avoided. Thus the image of a perfect point on the sample corresponds to a disc with a certain radius at the pinhole plane, the so-called Airy disc, or more exactly the Airy pattern if further orders of intensity maxima are taken into account (Figure 2.19). The Airy disc contains about 97 % of the total light while the first halo contains with 1.7 % the majority of the remaining intensity. Consequently, regarding the resolution vs. intensity issue, for most cases it makes sense to set the pinhole in a way that it fits the Airy disk while higher order maxima are excluded in the beam path. As a matter of fact it is not possible to make statements on the shape of objects smaller than the Airy disk, and also the disc radius r determines the smallest distance for distinguishing two objects and thus defining the lateral resolution. Formula 2.5 is a result of an estimation for the Airy radius for confocal microscopy. λ depicts the fluorescence wavelength. The opening angle ϕ and the refraction index of the lense n refer to the objective parameters and can be summarized to the numerical aperture (NA). Depending on the numerical aperture, with high quality optics about $20 - 25$ % of the emitted photons can be collected.

$$r_{confocal} = 0.4 \cdot \lambda \cdot (sin(\varphi) \cdot n) = 0.4 \cdot \frac{\lambda}{NA} \tag{2.5}$$

The resolution can be somewhat increased by reducing the pinhole size to diameters lower than the Airy 1 value, but this is accompanied by a strong decrease in intensity. On the other hand, if there are only minor requirements for the lateral resolution also big pinholes might be sufficient. For our device the pinhole sizes reach from 10 μm − 600 μm.

Basics of fluorescence

To find the optimal measurement setup for CLSM measurements of samples labeled with fluorochromes, some fundamental knowledge on the physics of the emission of fluorescence radiation is helpful as detailed described in in the textbooks (e.g. [118] and [117]). A fluo-

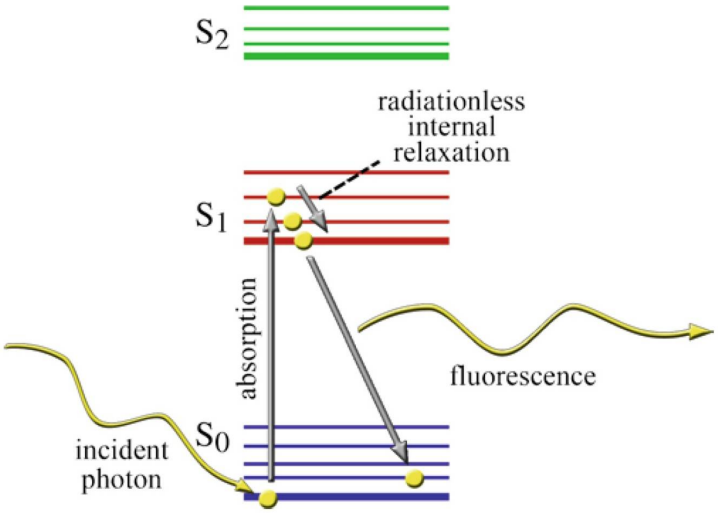

Figure 2.20: Jablonksi diagram illustrating the principle of fluorescence radiation generation. S_0, S_1 and S_0 label the main energy shells of the involved molecule. Reprinted from Reference [118] with permission from Elsevier.

rochrome molecule has the ability to absorb light of a defined wavelength thus performing an electronic transition to an excited state. ($S_0 \rightarrow S_1$). During a delay time (some picoseconds) non-radiative transitions might occur until the system reaches the lowest vibrational energy level of the excited electronic state (internal conversion). Subsequently, the molecule relaxes to the ground state S_0, which is accompanied by the emission of a fluorescence photon, featuring a wavelength larger than the excitement radiation as illustrated in the Jablonksi diagram in Figure 2.20. The energy of the fluorescent radiation is below the exaltation energy (Stokes shift), thus making it possible to discriminate between reflected or scattered primary photons and fluorescence (Figure 2.21).

Applications
According to the molecule's electronic and vibrational states, the fluorescence spectrum but also the excitation spectrum differ for different fluorochromes[1] (See Chapters 3.4 and 4.2.2). In a CLSM characteristic spectral properties of different dyes like Tetracycline (for humans) and Calcein or Alizarin (for animals) allow to separate the signal from the unspecific auto fluorescence and further to map the location of the various fluorochromes independently.

The mentioned substances refer to those, which are most commonly used to label mineralizing bone tissue. Of course there are manifold other fluorochromes designed for various applications providing insight into biological systems in vitro and in vivo as described in the literature [117].

Recently, a method was established to visualize the osteocyte-lacuna-canaliculi network making use of the fluorescent character of Rhodamine6G. Kerschnitzki et al. showed that a Rhodamine solution can be used to stain all inner and outer surfaces of the tissue, like cortical and trabecular surface and borders of the haversian channels, osteocyte lacunae, and canaliculi [85, 119]. Making use of the 3D imaging capabilities of the CLSM, a routine was developed

[1] http://www.lifetechnologies.com/at/en/home/life-science/cell-analysis/labeling-chemistry/fluorescence-spectraviewer.html

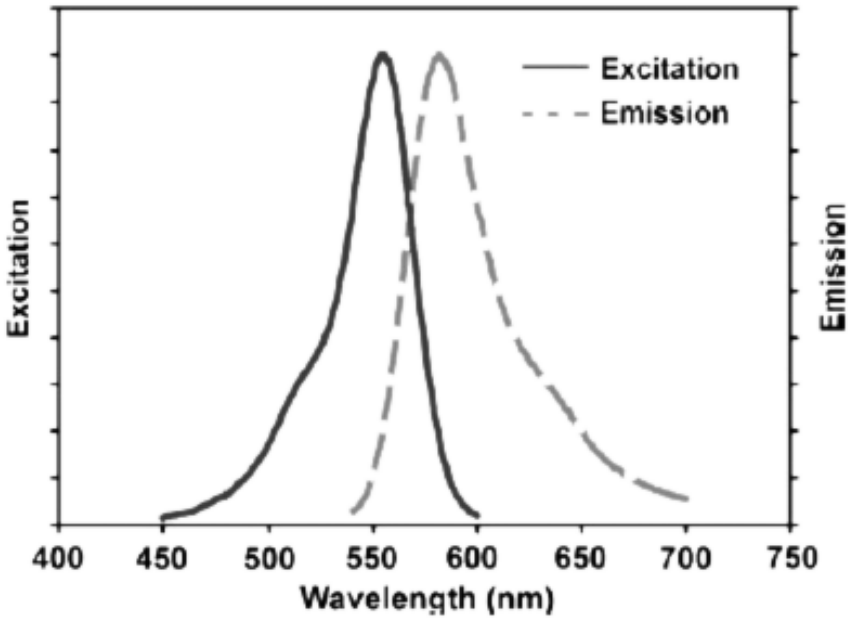

Figure 2.21: Excitation and emission spectrum of Tetramethylrhodamine isothiocyanate (TRITC) in methanol; Reprinted from Reference [118] with permission from Elsevier.

to produce volumetric images of the OLCN and further to use a skeletonization and quantification routine to gain network density and other parameters [85].

Additionally, we found that Rhodamine has an unspecific but high affinity to the organic matrix. This offers comprehensive information, when investigating mineralization defects, which include regions that exhibit no contrast to the embedding material in qBEI (Chapter 3.7).

Chapter 3

Material, Methods and Methodological Developments

3.1 Routine Sample Preparation

All specimens used in the present studies are undecalcified bone samples dissected from femurs of humans or mice, embedded in polymethylmethacrylate (PMMA) using an established protocol [14, 93, 120]. Murine distal femurs were fixed in 70 % ethanol immediately after dissection while human samples were frozen ($\approx -20°C$) for storage and put in 70 % ethanol before to sample preparation.

Prior to the embedding procedure, water was removed by a dehydration series of 70 % - 80 % - 95 % - 100 % ethanol and residual fat was removed by putting the dehydrated sample in acetone over night. If desired a Rhodamine6G (AppliChem, St.Louis, USA)-staining procedure as described in Chapter 2.2.4 was performed at this point. Subsequently, the sample was placed in PMMA and the hardening process was initiated in an incubator during careful control of the temperature (for more details see Reference [90, 95, 93]).

The PMMA blocks were then trimmed and a low-speed diamond saw (Buehler Isomet, Lake Bluff, Illinois) was used to cut the embedded bone samples in the desired orientation.

Murine femurs were cut either in longitudinal direction (Figure 3.1a) facilitating measurements at the cortical bone of the femoral midshaft (blue), the metaphyseal (red) and epiphyseal (orange) cancellous bone or in transversal direction at the diaphysis of the femur (perpendicular to the long axis of the bone). While longitudinal sections exhibit cancellous and cortical bone, growth plate and articular cartilage, transversal sections of the diaphysis gain access to the whole femur cross sections but include no trabecular bone structure (Figure 3.1b). Consequently, various cutting directions provide access to different histological regions. Thus, to decide the cutting orientation, the addressed problem needs to be taken into account.

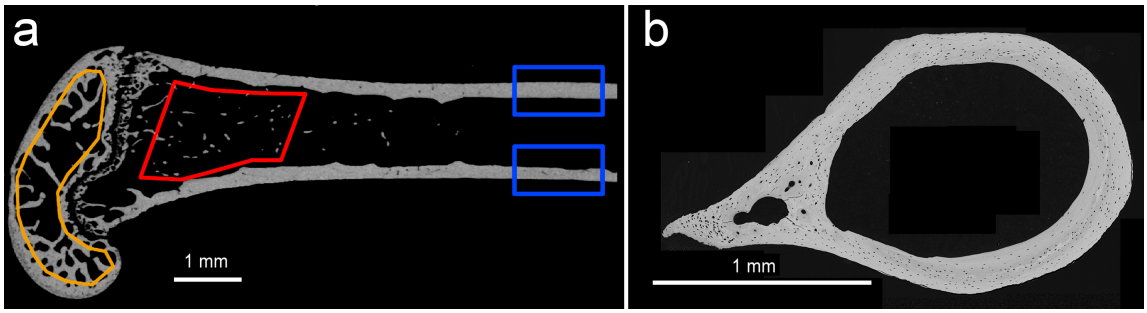

Figure 3.1: Example of longitudinal (a) and transversal (b) cutting direction of a mouse femur. Three compartments are considered for evaluation: diaphyseal cortical bone (blue), metaphyseal spongiosa (red), and epiphyseal spongiosa (orange)

3.2 Samples

Samples for studies on human bone, Chapters 4.1, 4.3, and 4.4
Femur samples of 10 humans (6 adults and 4 children, sample #1-11 in Table 3.1) were dissected from the diaphysis and were cut in transversal direction to preserve the circular shape of the osteons and to have access to the maximum cross-sectional area. For most of these samples, only half of the femur cross-section was available, but the lateral sites, which were used for the analysis, were always preserved (Figure 3.2). If desired, samples were stained with Rhodamine before embedding. The samples were provided by the Department of Forensic Medicine of the Medical University of Vienna and the study was performed in accordance with the ethic commission board of this institution (EK#: 1757/2013).

Samples used to study Sost-knockout (*SostKO*) mice (Chapter 4.2.2)
The speciments used in this study are sample sets #12-15 in Table 3.2. The paragraph is based on the corresponding section of the publication by N.Hassler, A. Roschger, et al. [18]. Details of the investigated mouse model have been published previously [74]. Four-month-old female wild-type (n=10) and *SostKO* mice (n=9) with a targeted disruption of the *Sost* coding region were maintained in cages with constant temperature of $25°C$ and a 12/12-hour light/dark cycle, fed a standard rodent diet (3302, Provimi Kliba SA, Switzerland) with water ad libitum. All animal experiments were performed in accordance with the Swiss federal law for animal protection under the control of the Basel-Stadt Cantonal Veterinary Office, Switzerland. The mice received in vivo fluorochrome double labels by subcutaneous injection. Prior to sacrifice of the animals, fluorochromes with a high affinity to Hydroxyapatite (HAP) were injected for four times at defined time-points. Two Calcein labels (green, 30 mg/kg; Fluka, Buchs, Switzerland)) were set 8 weeks before sacrifice with 10 days time interval, and Alizarin (red, 20 mg/kg; Merck, Zug, Switzerland)) was administered 5 and 15 days before sacrifice, labeling the very young tissue. This sort of multi-chromatic labeling of 4 time points is not done routinely, because for evaluation of dynamical histological parameters two labels of the same fluorochrome are sufficient. In our case the additional labeling of the 8 weeks old tissue together with the combination of material-characterization methods, provided substantial information on the mineralization kinetics and material development in the course of time in *SostKO* mice and wild-types. Femora were excised, fixed, dehydrated and embedded

Figure 3.2: A part of a native unembedded human femur dissected from the femur diaphysis prior to cutting and embedding. Lateral sites are avialable for analysis.

in PMMA as described above.

Samples used to evaluate the impact of sclerostin-antibody (SclAB) treatment in a mouse model of severe Osteogenesis Imperfecta (OI). (Chapter 4.2.3)
Samples described in this paragraph are the sample sets #16-23 in Table 3.2. The following text is based on the corresponding section of the publication by A. Roschger et al. [21].
Mice with a defined genetic mutation (in precise: the splice donor site of exon 9) of the collagen type I coding gene ($Col1a1$) were used, as previously described [121]. The mice (denoted as $Col1a1^{Jrt/+}$ mice) were bred on a FVB background [1] and were generously provided by Dr. J. Aubin, University of Toronto. Animals were housed in the Animal Care Facility of the Shriners Hospital Montreal. The project was approved by the McGill University Institutional Animal Care and Use Committee. Male wild-type and $Col1a1^{jrt'/+}$ mice were randomly assigned to SclAB treatment or control injections, starting at either 4 weeks (phase of rapid growth, 'pediatric model') or 20 weeks of age ('adult model') with $n = 8$ per group. SclAB (designation as BPS804; developed in a collaboration between Novartis Inc and MorphoSys Inc) or control antibody was used. The control antibody was an unrelated antibody that had been raised against chicken lysozym. Antibodies were injected intravenously at a dose of 100 mg/kg BW, based on prior studies by Novartis Inc. The total injection volume was 50 μL. Injections were given once per week over a period of 4 weeks. Mice were euthanized at the end of the 4 week intervention period, i.e., at the age of 8 weeks and of 24 weeks, respectively. To enable the analysis of dynamic histomorphometric measurements, each mouse received two intraperitoneal (into the abdominal cavity) injections of Calcein (25 mg per kg body weight) at 5 days and at 2 days (8 weeks old) and at 6 days and at 2 days before sacrifice (24 weeks old), respectively.

[1] "FVB" depicts an established mouse strain, that is commonly used for modeling of genetic diseases

Table 3.1: Overview over all human samples which were investigated in the frame of this thesis. The specimen were cut out of the femoral diaphyseal midshaft in transversal orientation.

sample#	group	internal ID	Rhodamine staining	age	sex
#1	adult	FM46	no	39a	f
#2	adult	FM30	no	29a	f
#3	adult	FM38	no	55a	f
#4	adult	FM04C	yes	50a	f
#5	adult	FM38r	yes	55a	f
#6	adult	FM40	yes	56a	f
#7	adult	FM48	yes	48a	f
#8	child	FM15	yes	1.5a	m
#9	child	FM21	yes	2.5a	f
#10	child	FM25	yes	1.5a	f
#11	child	FM28	yes	16m	f

Table 3.2: Murine samples used in the projects described in Chapter 4.2.2 and Chapter 4.2.3

sample (set) Nr.	genotype, treatment	internal ID	sample site	orientation	flourochrome labeling	age	sex
#12	CL57BL/6 wild-type	So 1, 4, 7, 10 ,13, 16, 19, 22, 25, 27, 28	femur	longitudinal	no	16w	f
#13	CL57BL/6 *SostKO*	So 3, 6, 9, 12, 15, 18, 21, 24, 30	femur	longitudinal	no	16w	f
#14	CL57BL/6 wild-type	So 31 - 40	femur diaphysis	transversal	4 labels	16w	f
#15	CL57BL/6 *SostKO*	So 41 - 49	femur diaphysis	transversal	4 labels	16w	f
#16	FVB wild-type	To 1 - 8	femur	longitudinal	2 labels	8w	m
#17	FVB $Col1a1^{Jrt/+}$	To 9 - 16	femur	longitudinal	2 labels	8w	m
#18	FVB wild-type +SclAB	To 17 - 24	femur	longitudinal	2 labels	8w	m
#19	FVB $Col1a1^{Jrt/+}$ +SclAb	To 25 - 32	femur	longitudinal	2 labels	8w	m
#20	FVB wild-type	To 33 - 40	femur	longitudinal	2 labels	24w	m
#21	FVB $Col1a1^{Jrt/+}$	To 41 - 48	femur	longitudinal	2 labels	24w	m
#22	FVB wild-type +SclAB	To 49 - 56	femur	longitudinal	2 labels	24w	m
#23	FVB $Col1a1^{Jrt/+}$ +SclAb	To 57 - 64	femur	longitudinal	2 labels	24w	m

3.3 Quantification of the Calcium Content of Bone using a Field-Emission Scanning Electron Microscope

In the scope of this thesis, established characterization techniques for bone were extended, combined with other methods, or newly developed. This facilitates new approaches in characterizing bone tissue, exceeding the routinely applied methods in terms of a more comprehensive micro architectural and chemical analysis of the same samples in an almost non-destructive way.

As introduced in Chapter 2.2.1, outgoing from the observation that the intensity of backscattered electrons mirrors the degree of mineralization [92], quantitative backscattered electron imaging (qBEI) became a validated tool for the quantification of local Ca concentration of undecalcified PMMA embedded bone samples [95, 93]. For the last 15 years, qBEI measurements were performed at the Ludwig Boltzmann Institute for Osteology, Vienna, Austria, with high consistency, contributing significantly to the understanding of bone matrix mineralization in health and disease [14, 96, 122, 123, 124]. The current operating device, a Zeiss DSM962, (Oberkochen, Germany), will be replaced soon by a Zeiss Supra40 (Oberkochen, Germany) last-generation field emission cathode scanning electron microscope (FESEM). Therefore, the previously established measurement and quantification routines need to be adapted to the new device with special respect to measurement reproducibility, stability of primary beam and detector, counting statistics, beam damage of the sample and last but not least comparability of the results to the old device. Table 3.3 compares the two devices and depicts the main differences.

For reliable quantitative measurements, stability of primary electron beam and detector electronics are crucial to guarantee correct gray value information once the calibration routine is performed as described in Chapter 2.2.1.

For both devices the specimen current is monitored using a faraday cup (mounted on a regular sample holder) before and after quantitative measurements to assure that variations in the beam current do not account for more than $\pm$ 1 value deviation from the original value.

Table 3.3: Comparison of the two scanning electron microscopes, which were used in the scope of the reported work: The (about 15 years) old device (DSM962) will be soon replaced by a state of the art field emission scanning electron microscope (FESEM - Supra40))

	Carl Zeiss - DSM962	Carl Zeiss FESEM - Supra40
Cathode Type	Tungsten Hairpin Cathode	Schottky field emission electron gun with zirconium envelope
specimen current	110 pA	280 pA - 310 pA
optimized working distance	15 mm	10 mm
backscattered electron detector	4-quadrant solid state detector	4-quadrant solid state detector
vacuum requirements	10^{-5} - 10^{-6} $mbar$	$<10^{-5}$ $mbar$ in the sample chamber $<10^{-9}$ $mbar$ in the gun chamber
operating high voltage for qBEI	20 kV	20 kV
image format	512×512 px - .pic	1024×768 px - .tif
field of view	1144×901 μm^2 at pixel size 1.76 μm^2 (100×) 572×451 μm^2 at pixel size 0.88 μm (200×)	1802×1351 μm^2 at pixel size 1.76 μm (65×) 901×676 μm^2 at pixel size 0.88 μm (130×)
Operating Software	DSM962 - Software package v2.1 on MS-DOS 5.00	Smart Sem (version 05.05.00) on MS WindowsXP

Primary beam stability

While a tungsten-hairpin cathode as used in the DSM962 microscope allows a precise fine-tuning of the extractor current to maintain a constant specimen current, the electron flux of the field emission cathode in the Supra40 system varies during its lifetime of more than 1000 h. Within the timespan of some hours this drift revealed to hardly affect the calibration. To prohibit significant alterations of counting statistics and beam damage due to long-term changes in the beam intensity, the allowed specimen current bandwidth was restricted to $280 - 310$ pA. Additionally, after enabling the high voltage at the beginning of a measurement day, it takes the electron beam about 15 minutes to reach stable conditions where no quantitative measurements can be performed.

Detector stability

Surprisingly, the stability of the backscattered electron detector (or more precisely of the detector's preamplifier) revealed to be a major issue. We noticed that the amplifier electronics exhibited a significant temperature dependency adulterating the outgoing signal depending on the room temperature (Figure 3.3). In addition, a memory effect was observed leading to brighter gray value images subsequent to measurements on high Z materials (Figure 3.4).
It was possible to overcome these problems by testing various preamplifiers. The original component was replaced the by one that did not exhibit any detectable memory effect and only showed a minimal sensitivity to changes of the environmental temperature. In addition, the closed cycle cooling system was extended to include the detector's preamplifier and a

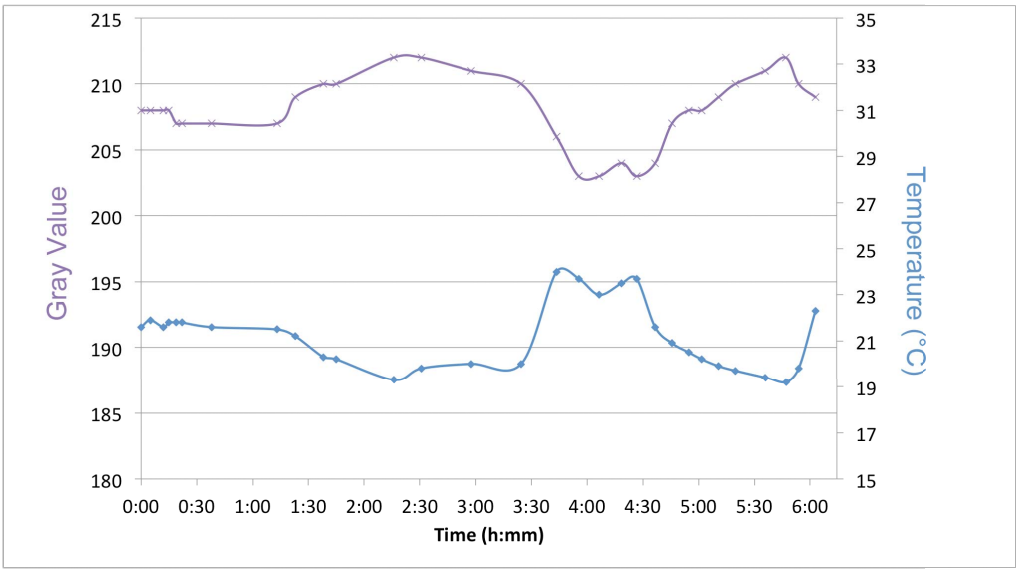

Figure 3.3: Temperature dependency of the original backscattered electron detector preamplifier: The impact of a change in the room temperature on the measured gray values was highly reproducable.

thermoconducting fleece was mounted on the circuit board to assure constant temperature of the most sensible electronic parts.

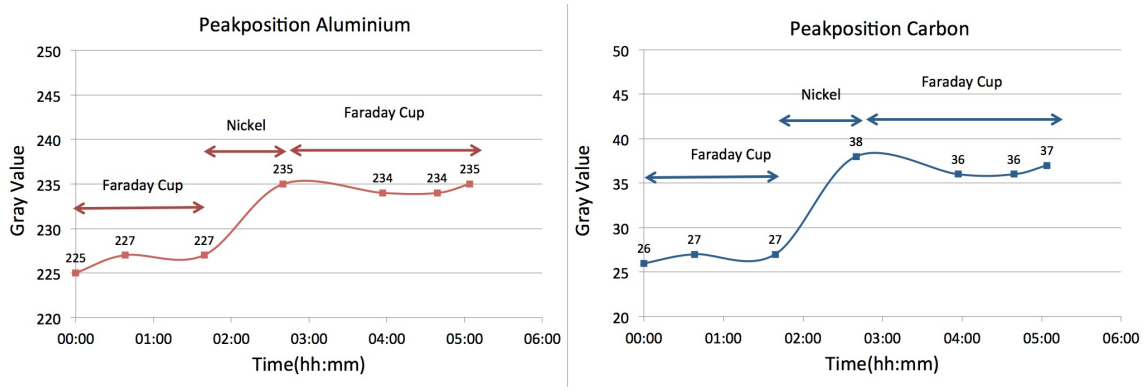

Figure 3.4: The diagrams of a Al/C reference material (the same as shown in Figure 3.7) reveal a distinct memory effect. While gray values were stable during scanning a Faraday cup (no signal at the detector) an offset was observed after scanning a Ni sample(high electronic signal).

Counting Statistics and Beam Damage

When interpreting bone mineralization density distributions (BMDD) as described in Figure 2.11, not only the peak position is taken into consideration, but also the width (full width at half height (FWHH)) of the BMDD curve, being a parameter of the heterogeneity of mineralization. It was previously shown that beside the mineralization pattern of the bone, also the counting statistic and therefore the resulting noise in the images account for about 5 %

of the BMDD's FWHH [125]. Since the counting statistics depend on multiple (and partly unknown) parameters like primary beam intensity, working distance, detector area, detector design and electronics, the best way to compare the characteristics is to have a look at peak shapes of reference materials with both microscopes, rather than to calculate the detected electrons. This is done in Figure 3.5 where the dashed line represents the calibrated measurements in the standard setup with the DSM962 on an Aluminum (Al) standard material while the colored lines belong to Supra40 measurements with various scan-speeds on the identical region of interest.

Scan Speed 11 (90 s $image$) exhibited a FWHH value closest to the reference curve of the validated device. As expected broadening of the distribution was observed with increasing scan speed due to increased noise as a result of lower count rates.

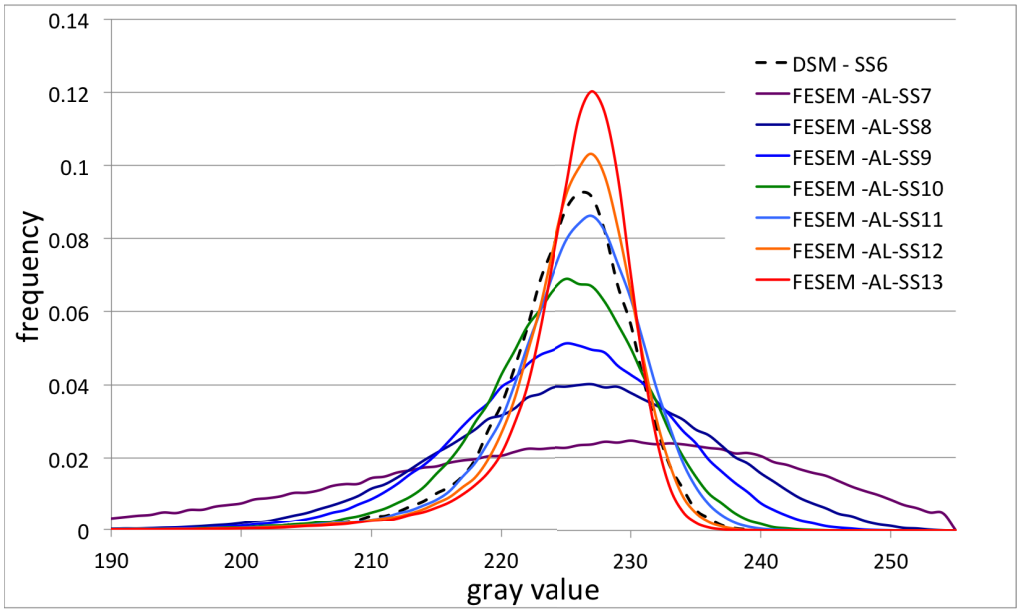

Figure 3.5: Measurements on an *Al* sample with various scan speeds (acquisition times): The dotted line was the result of a standardized measurement using the old DSM962 device while the other lines correspond to histograms obtained with the FESEM Supra40 device.

As for the Supra40 system scan speed 11 (90 s $image$) revealed to lead to comparable counting statistics for the two microscopes the question arises if the beam damage is also similar. In Table 3.4 these calculations are performed for different resolutions with respect to similar pixel size. According to the increased pixel number per image of the new device, the field of view is enlarged (and thus the magnification decreased) for a given pixel size.
In Table 3.4 the electron exposure per m^2 (ke m^2) is introduced as a measurement for the beam damage and is supposed to correlate strongly with the real damage caused by bombardment of electrons. It is suggested that the main beam damage effect is linked to burning of C and O [126, 127]. That is consistent with our observations . This likely leads to a loss of light elements in the target material and consequently to an increase of the average atomic number; thus the yield of backscattered electrons increases in the exposed regions as

Table 3.4: Estimation of the beam damage (electron exposure) using optimized measurement parameters for the microscopes: The magnification of the FESEM Supra40 system was chosen with respect to the pixel size of images gained at the DSM962 device. (FOV = field of view)

	Specimen I (pA)	Pixel (x)	Pixel (y)	Resolution (m px)	FOV (x) (m)	FOV (y) (m)	meas Time (s)	e exposure ke (m^2)
DSM962 (100)	110	650	512	1.76	1144	901.12	90	60
DSM962 (200)	110	650	512	0.88	572	450.56	90	240
Supra40(65)	300	1024	768	1.76	1802.24	1351.68	90	69
Supra40(135)	300	1024	768	0.88	901.12	675.84	90	277

a function of exposure time and electron flux. Even though the introduced parameter for the beam damage seems to be reasonable, no information is included about the time course of exposure. It is reported that the change of the chemical composition of bone is not the same for continuous and intermittent electron bombardment [126, 127]. Nevertheless, according to the analogue measurement routine and the fact that the electron exposure is similar for both routines, comparable beam damage is expected for both devices as long as measurement parameters are preserved as described above. In Figure 3.6 the result of 8 subsequent calibrated measurements on bone and PMMA with measurement parameters typical for the investigation of human bone is shown. While there is no impact on the peak related to mineralized bone tissue (a) the gray value of PMMA increased by one within the course of the measurements (b). Thus, we conclude that for qBEI measurements beam damage is not a problem even if the same region is scanned for multiple times.

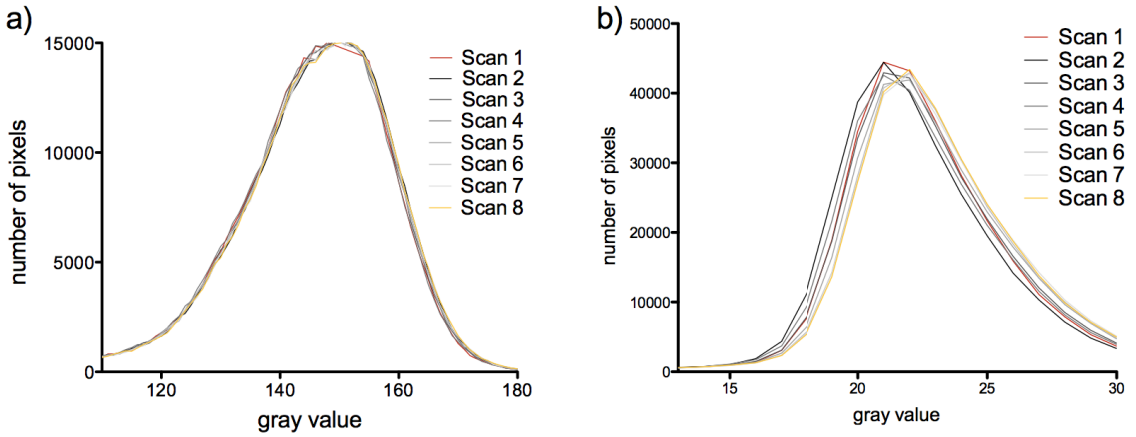

Figure 3.6: Histograms of eight repeated measurements performed on the same region of an embedded bone sample exhibiting mineralized matrix and PMMA with common measurement parameters: No drift is observed at the gray values of the bone region (a) while a minor beam damage effect is present at PMMA (b).

Calibration routine

The calibration routine for measurements with the Supra40 SEM is done analogously to the routine reported for the DSM962 [93]. Using 65 magnification (1 76 m^2 pixel size corresponding to $100x$ magnification at the DSM962) a C, Al dual element reference sample is continuously measured with the Supra40 device. Simultaneously the gray value histogram is calculated automatically and imaged as shown in Figure 3.7. By adjusting the detector's gain and offset (contrast and brightness of the image) peak positions are set to the grey values 25 (C) and 225 (Al). 1 grey level (corresponding to 0 17 $wt\%Ca$ [93]) deviation is tolerated. Once this is done, brightness and contrast parameters are stored and must not be changed. After some measurements (typically 20 minutes) the reference sample is re-measured to monitor the instrument stability. As long as the reference measurements before and after taking qBEI images are consistent, the images are considered for further evaluation.

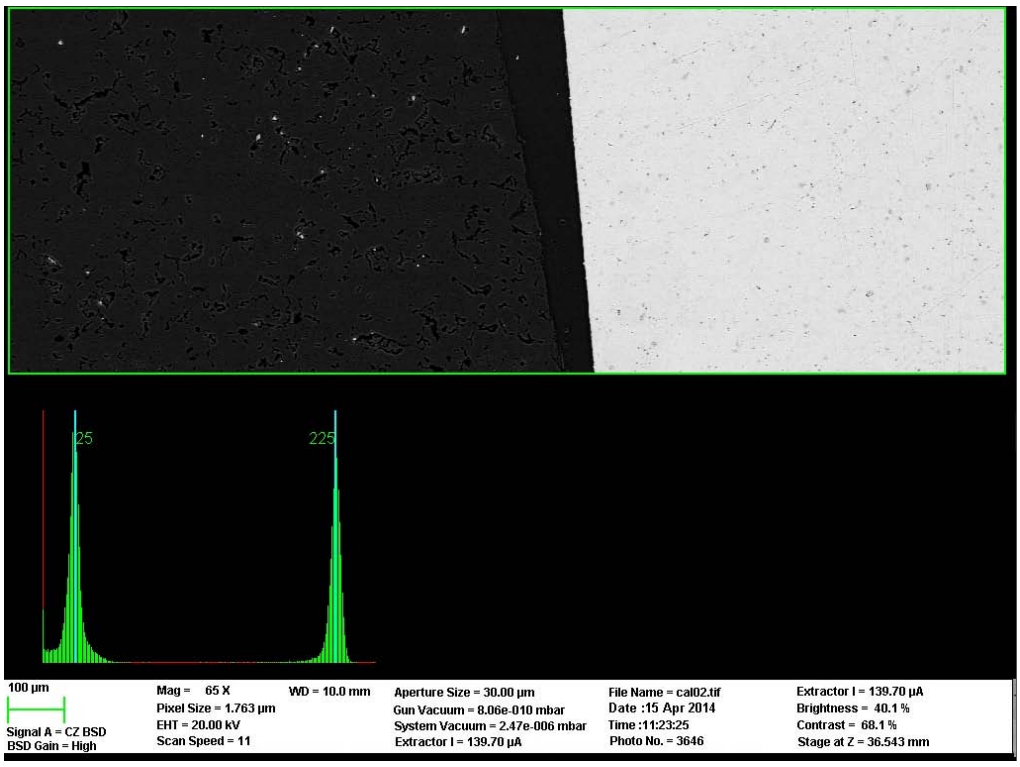

Figure 3.7: Calibration routine using an Al - C reference sample: The upper panel shows the backscattered electron image of the dual reference sample (C: left, Al: right). In the lower panel, the current histogram is shown in real time during the continuous scanning process. Brightness and contrast of the image is adjusted to fit the peak positions of the histogram to 25 (C) and 225(Al)

Direct comparison of the devices

After the considerations made in this chapter, beam and detector stability, image quality, beam damage and the calibration routine seem to be under control in the new Supra40 SEM and the results are supposed to be comparable to the validated and established DSM962 device. Thus measurements with both devices were performed covering the same regions of

interest on the same sample (human cortical bone) with 1.76 μm^2 pixel size (65× and 100× magnification respectively). Figure 3.8 opposes the calibrated measurements with the previously determined parameters.

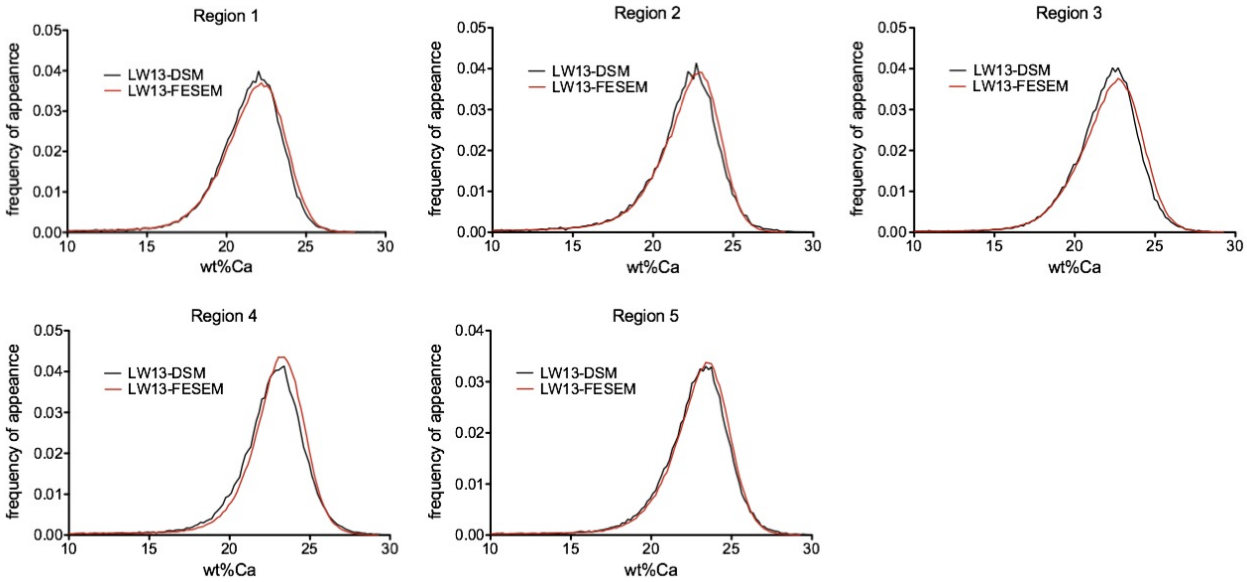

Figure 3.8: Calibrated qBEI measurements of the same ROIs with standardized measurement parameters using the DSM962 and the FESEM Supra40 device: In none of the five analyzed regions notable differences between the two histograms are observed.

It can be seen that the BMDD histograms for all 5 selected regions are nearly identical for both systems. Thus we conclude that the results are comparable and it is allowed to compare measurements made on the Supra40 microscope to the previously published reference values of healthy human people measured at the DSM962 system [128].

3.4 Determination of the Calcium Content at Defined Tissue Age

One strength of the qBEI method is the ability to gain information on mineralization of large bone areas (e.g. of human bone biopsies). Thus a BMDD curve as shown in Figure 2.11, contains information of the whole measured surface. In healthy bone low mineralized regions (left tail of the BMDD curve) likely correspond to young regions where the early mineralization process occurs while old, interstitial bone packets are normally higher mineralized and thus refer to the right tail of the curve. In spite of these considerations, in principle information on the spatial distribution of mineralization and on the age of the investigated tissue is not contained in the BMDD measurement as described in Chapter 2.2.1. Thus, if deviations from a reference BMDD curve are observed, they are difficult to be interpreted without additional information on bone turnover, which can be obtained by histomorphometry (dynamic indices

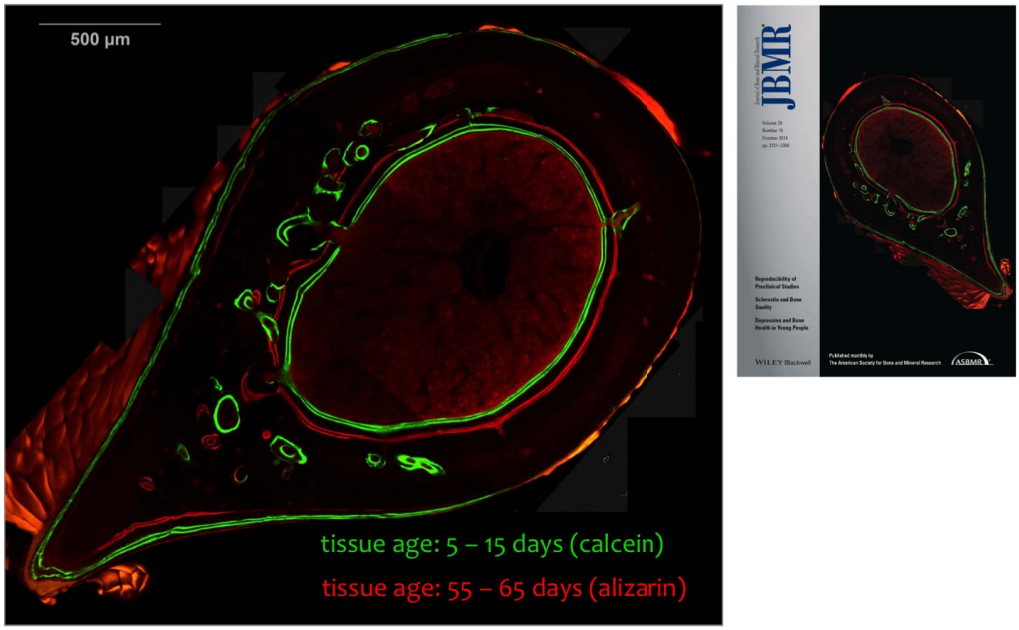

Figure 3.9: Confocal laser scanning microscopy (CLSM) image of a *SostKO* mouse with two double labels: Alizarin and Calcein fluorochromes were injected at defined time points into the living mouse to mark regions of active bone formation. The image was chosen for the cover page of the an issue (October 2014) of the Journal for Bone and Mineral Research (JBMR)

of bone formation). Hence, it was part of this thesis to develop a routine to use qBEI for collecting information on bone matrix mineralization of defined tissue ages and so to create a tool designed to reveal potential changes in the mineralization kinetics. This was done on the occasion of a mouse model of *SostKO* mice representing a stage of drastically increased bone apposition published by N. Hassler A. Roschger et al. [18] (Chapter 4.2.2).

Animals used for this study (see Table 3.2) were labeled with fluorochromes as introduced in Chapter 2.2.4) for four time points. The first double label (Alizarin-red) was set 8 weeks and the second one (Calcein - green) two days before sacrifice (Figure 3.9). Within the double labels there was a time difference of 10 days. As the fluorochromes bind to HAP, they deposit in the mineralizing tissue short after injection. If the dissected tissue is then investigated using a confocal laser scanning microscope (CLSM), narrow green and red bands mark tissue of known age.

A routine was developed making use of the simultaneous acquisition of fluorescent and reflection images of the sample surface using the CLSM as follows: As reflection, fluorescence and SEM signals originate from the same sample surface, reflection images are used to determine the transformation parameters (translation, flip and rotation) between CLSM and SEM. Sharp edges and features like osteons and osteocyte lacunae facilitate precise superposition with an uncertainty of about three m. The transformation parameters are stored and then applied to the corresponding fluorescent image. This procedure facilitates matching of the

backscattered electron signal and fluorescent labels, in a quality which could not be achieved without taking the reflection images into account.

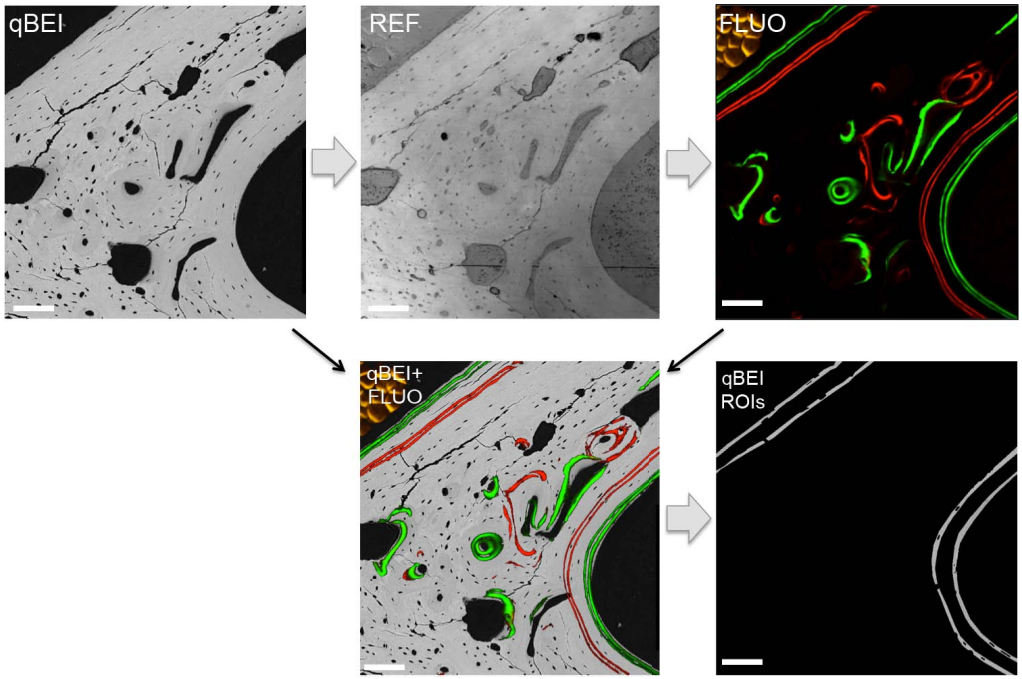

Figure 3.10: Matching of quantitative backscattered electron images (qBEI) with fluorescence images (FLUO): Reflection images (REF) obtained simultaneously with the fluorescent images facilitating precise superposition and thus tissue age information can be transferred to the qBEI image (qBEI ROIs).

In the following, the positions of the labels are marked, stored, and denoted with respect to their location and fluorochrome type using ImageJ (NIH, v1.48c). They are then transferred to the qBEI image where exclusively the regions within the double labels are considered for further evaluation (Figure 3.10). After clearing the images from cracks and osteocyte lacunae, the gray values are converted into $wt\%Ca$ values according to the standard routine.

Regarding the current project, this new procedure helped to determine the degree of mineralization at two defined time points in $Sost \quad KO$ and wild-type mice providing information on the mineralization kinetics and also new possibilities in comparison with other established methods like Raman micro spectroscopy [18] .

3.5 Energy Dispersive X-ray Analysis (EDX) to Characterize the Composition of Bone

As introduced in Chapter 2.2.2 EDX is a spectroscopic method, which facilitates qualitative and quantitative characterization of the distribution of major and minor elements in a target material like bone. For these measurements a field-emission electron microscope (Supra40,

Zeiss, Oberkochen) was equipped with a silicon drift energy dispersive X-ray detector (SDD) (Oxford instruments, $X - Max^n 80$) with 80 mm^2 sensor area. Sensor cooling is provided using a two staged Peltier element. A polymer-window as well as a vacuum environment allows also the measurement of low Z materials like C, N and O. For the current studies, an EDX measurement routine was developed to characterize mineralized bone matrix with special respect to the Ca/P ratio. As mentioned in Chapter 2.1.3 and Chapter 4.1.3 the majority of Ca and P is bound to the mineral phase. Thus, changes in the corresponding elemental ratio likely indicate alterations in the crystal composition as it is already reported for bone diseases like Osteogenesis Imperfecta [129]. Literature is spare comparing the Ca/P ratios in healthy bone within various histological compartments.
Despite the power of this method (fast data acquisition, well-defined information volume according to the high lateral resolution, low information depth, and low background noise) some considerations need to be made to estimate the limits of the method as discussed below.

Optimization of the measurement setup
A series of measurements was performed to determine optimal parameters, taking into account acceptable beam damage, detector dead time (signal processing time), count rate, and the elements of interest. Compared to settings optimized for qBEI measurements, the device is now operated in the high current mode using a 60 μm pinhole featuring a beam current of about 1.5 nA. The acceleration voltage is reduced from 20 kV to 10 kV to reduce the sampling volume and the countrate, and to increase the sensitivity for low Z elements. In principle these modifications allow high-resolution mapping of elemental distributions with a resolution below 1 μm, but for that a long acquisition time (and thus increased beam damage) is needed. Thus for the purpose of quantitative EDX measurements where no high-resolution is needed, a sample region of 39.1×29.3 μm^2 was scanned (3000× magnification). The sampling time was set to 30 s lifetime ($\approx$ 40 s realtime) using the process time index 4 (INCA software package, v4.15, Oxford Instruments, Oxfordshire, UK). Longer acquisition times or longer process times showed only minor improvements of the spectrum quality.

Quantification routine
Using these parameters, the quantification was performed using the INCA software package. As for most commercially sold quantification software, the underlying mathematical algorithms are unknown prohibiting customized fitting and correction algorithms. The software includes an automated peak identification, a pile up correction and a correction for the thickness of the carbon coating. A so called quantoptimation with a reference material (Ni), is done before each measurement series, thus performing an energy calibration fine-tuning and fluorescence radiation flux measurement which are needed later during quantification.

The quantification routine of the INCA software also incudes a database of measured standard reference materials allowing a fully automated quantification. Nevertheless, as the main aim of our quantitative approach was the determination of the Ca/P ratio of bone, fluorescent parameters gained from a house-made HAP pellet were added to the database and used for all consecutive quantifications of Ca and P. Additional to the calibration standards, the quantitative results are influenced by parameters like the considered elements, the thickness of the carbon coating and its inclusion in the evaluation, and the assumption of a so called

"dark matrix" which is added if the total fluorescence intensity is less than expected from the quantoptimation. The implementation of these parameters is up to the operator and thus limits the explanatory power of the quantitative statements. While the comparisons with quantitative results based on other methods and devices must be done with caution, measurements of similar regions of interest under unchanged excitation and quantification conditions on the same device feature high comparability.

We found that the Ca P ratio, which is of special interest for our considerations, seems to be a robust parameter regarding changes in the quantification parameters while this is not the case for Ca and P absolute values as shown in Figure 3.11

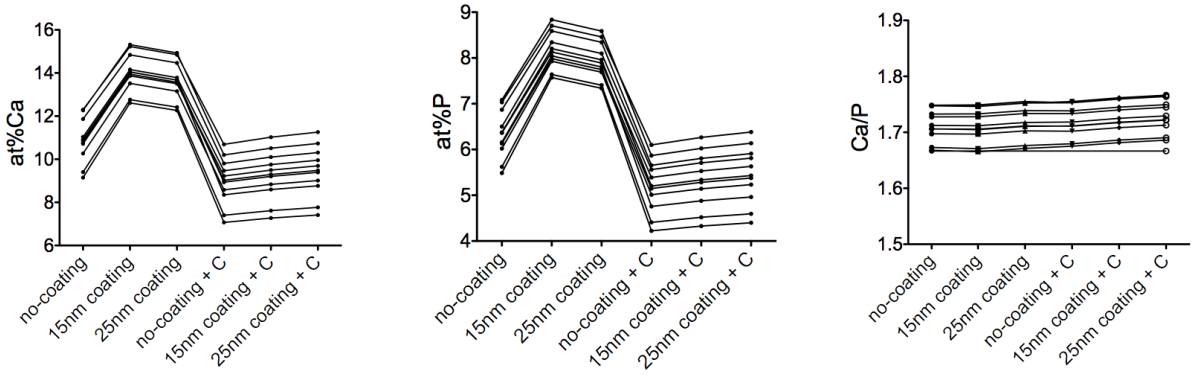

Figure 3.11: Results of the quantification procedure with different parameters for Ca, P and Ca P: C - coatings with variable thicknesses are assumed in a model with and without C considered as "dark matrix".

For the measurements in our study, calculations were performed assuming a Carbon coating of 20 nm thickness and also C was used to characterize the dark matrix. For all elements beside Ca and P, fluorescent parameters from the original INCA database were used for quantification.

Beam damage

After these considerations, the effect of the electron-induced beam damage can be elaborated for the standardized measurement and quantification parameters as they are used for the analysis of the samples in the studies.

To do this, ten regions of interest (ROIs, 44 59 m^2, 2000 magnification) were located inside various bone structural units as shown in Figure 3.12. EDX spectra of each ROI were consecutively obtained 20 to 130 times with 20 s lifetime resulting in an electron exposure time of 28 s (about 40 % dead time).
According to the consecutive measurements of the same ROI, the beam damage can be evaluated by monitoring results of the quantification for each element. This is done in Figure 3.13 by plotting elemental concentration vs. electronic exposure time (=real time).

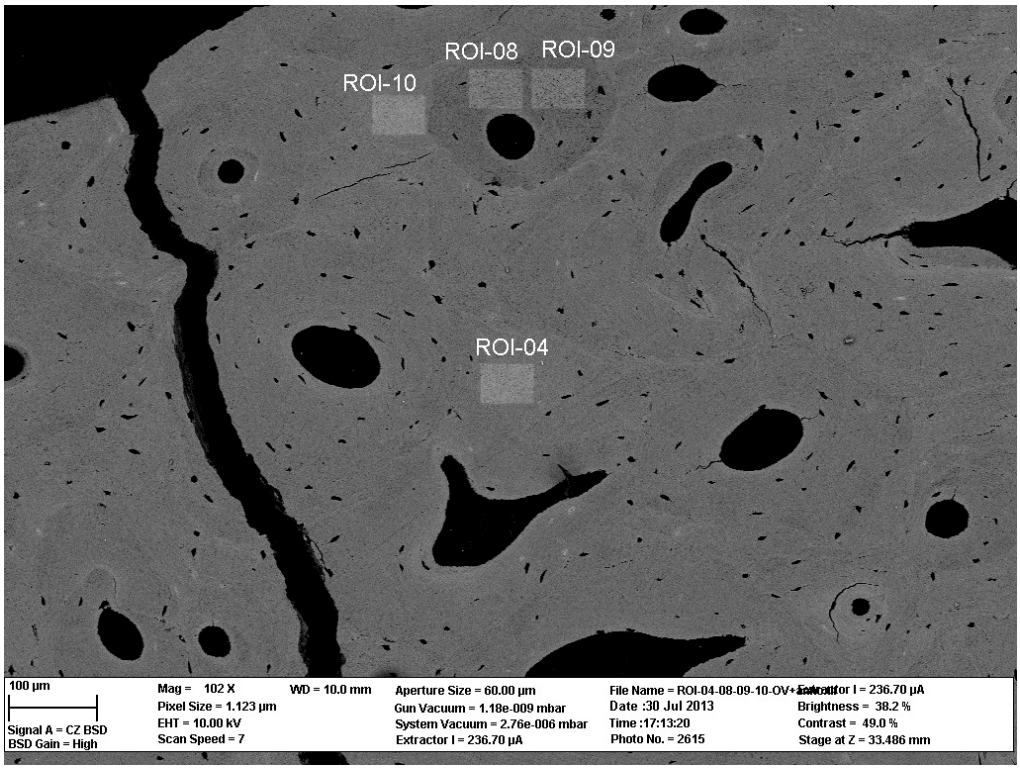

Figure 3.12: Backscattered electron image of human cortical bone (femur midshaft), which was taken after the EDX measurements: The exposed regions ($44 \times 59\ \mu m^2$) appear lighter due to the damage caused by the electron bombardment.

The results of these measurements are crucial for the interpretation of the quantification. While the apparent concentration of Ca and P distinctly increase in the course of electronic bombardment (Figure 3.13a,b), this is only to minor extent the case for Mg and Na. (Figure 3.13e,f). The loss of C is consistent with literature where "burning" of low Z elements due to beam damage is described [130, 131]. Importantly, the $at\%Ca/at\%P$ ratio does not depend on the exposure time and therefore on the beam damage (Figure 3.13c). As long as a standardized routine had been performed, the relative comparison of all quantification results seems to be adequate. The dotted lines in Figure 3.13 represent the points of estimated beam damage after a single measurement with standardized parameters as described above (magnification (3000×), exposure time ($\approx 40\ s$), pinhole ($60\ \mu m$)). The lines are located at the 95 s mark, which is due to shorter measurement time and lower magnification of these test measurements.

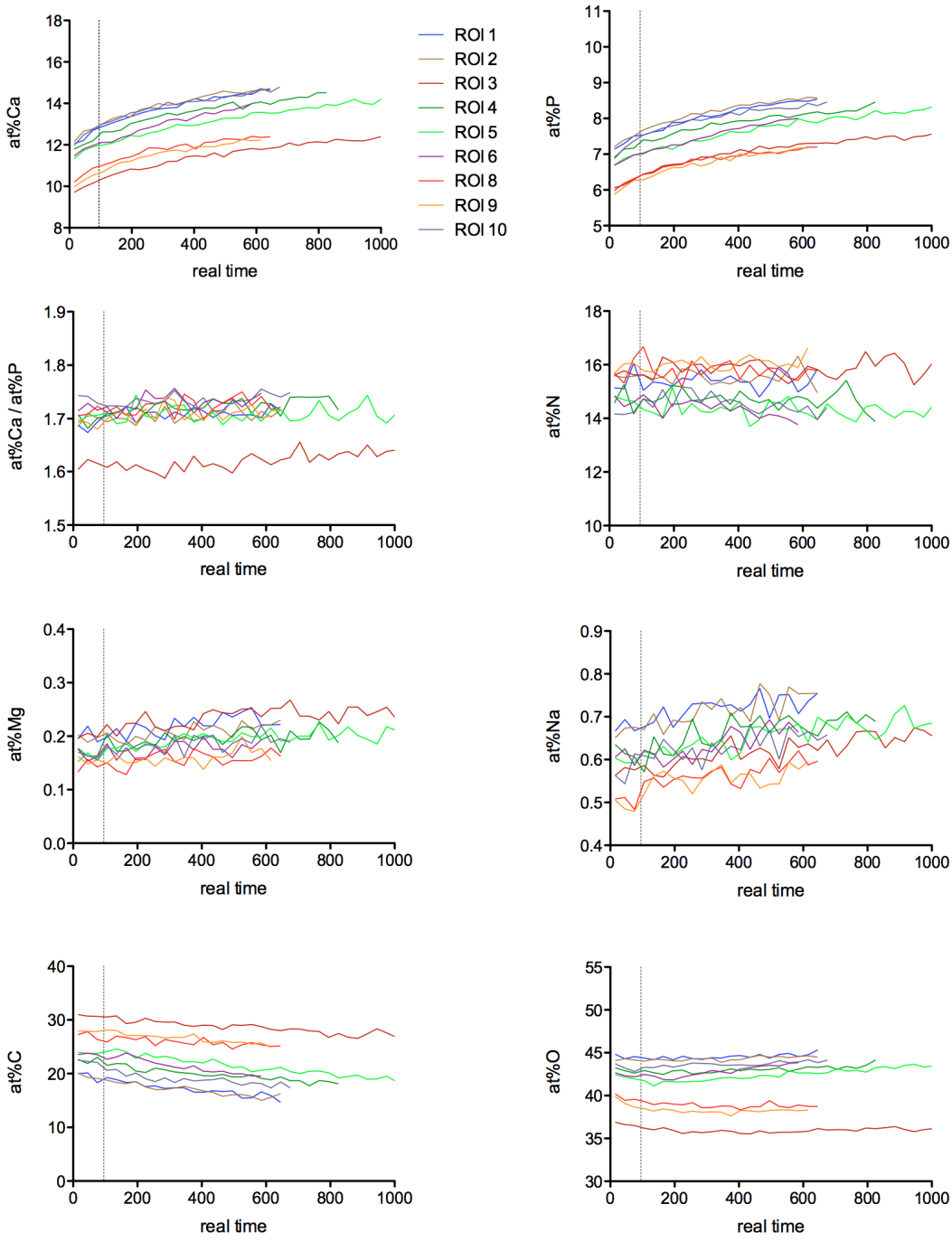

Figure 3.13: Evaluation of the beam damage for different elements caused by the electron exposure during EDX analysis: Each line corresponds to consecutive measurements performed on the same 44 59 m^2 area as shown in Figure 3.12. The dotted line represents the beam damage which is expected for the standardized measurement routine and is located at the 95 s mark.

3.6 Visualization of the Osteocyte Lacunae Canaliculi Network (OLCN)

Within the last years, studies revealed the involvement of the osteocytes and the OLCN to play a major role in bone matrix mineralization [5, 4]. It was also shown that through its large surface, the OLCN provides global access to mineralized regions inside the bone matrix, making a direct interaction between the network and bone quality parameters plausible [85, 22]. To gain more information on the OLCN structure, a technique was developed to stain all inner and outer bone surfaces using Rhodamine staining of native samples [85, 119]. This approach facilitates the visualization of osteocyte lacunae and the OLCN by using a CLSM. Until yet the staining and imaging routine was applied to undemineralized, unembedded bone samples by putting the sample into a Rhodamine6G - saturated aqueous solution prior to CLSM measurements.

Adaptation of the staining procedure
One aim of our studies was to locally correlate features of the OLCN (measured with CLSM) with the composition of the bone matrix gained from qBEI and EDX. Hence, it was necessary to modify the staining routine to make it compatible with the standard PMMA embedding procedure as described in Chapter 3.1 and thus to avoid the use of water for staining purposes. A tests series was performed comparing staining qualities using a PMMA-Rhodamine mixture and an ethanol-Rhodamine mixture. According to the findings, we decided to stain the samples using a mixture of ethanol and Rhodamine (1.25 g Rhodamine per 300 ml ethanol) which was applied after dehydration and prior to embedding as described in Chapter 3.1. Tubes containing samples and staining fluid (40 ml) were mounted overnight on a homemade low-speed spinning wheel, facilitating permanent fluid flow and thus ideal penetration. For human samples the staining fluid was renewed for three times while for mice bone a single fluid exchange was sufficient due to the lower bone volume. Afterwards, embedding, hardening, and further sample preparation steps were performed as usual and seemed to be unaffected by the staining. Network visualization was performed on the polished and uncoated blocks using a CLSM (CTS SP5, Leica, Wetzlar, Germany).

Standardized parameters for the investigation of bone samples
Human osteonal bone regions were investigated using a 40 $\times$ magnification oil immersion objective (Leica, HCX PL APO 40$\times$ $NA = 1.25$) and the image resolution was set to 1024 $\times$ 1024 px (field of view:388 $\times$ 388 μm^2 pixel size: 378 nm^2). Images were taken with a 543 nm laser combined with a Substrate beam-splitter. The reflection signal of a 488 nm laser beam was simultaneously collected making use of a separate photomultiplier.

Overview images were generated by using an automated grid scan (pinhole: 67.9 μm) and subsequent stitching, performed by the operating software (Leica LAS AF v2.6.4.8702) resulting in 2-dimensional high-resolution images covering the whole sample reaching file sizes of up to 1.2 GB per .tif image.

Using the parameters mentioned above, except for the airy1 pinhole (67.93 μm), consecutive

images where obtained of different layers in vertical (z) direction with a step size of 300 nm up to a depth of around 60 m below the surface resulting in about 200 single images. In the course of such an image stack acquisition, a predefined continuous adjustment of laser intensity and photomultiplier gain voltage was performed to correct for laser and fluorescence radiation attenuation and thus to maintain constant image quality.

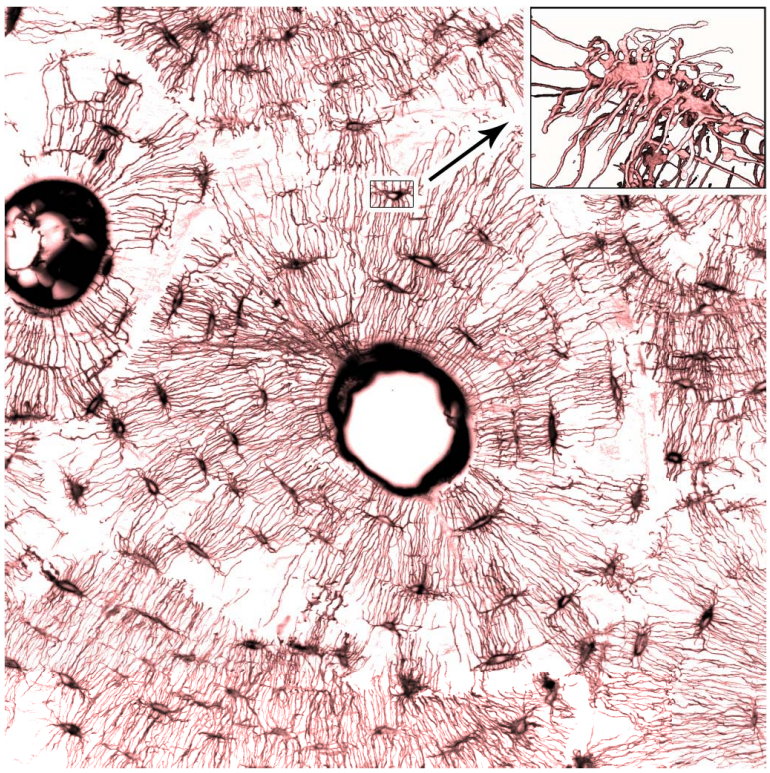

Figure 3.14: Confocal laser scanning microscopy (CLSM) image of the Rhodamine stained osteocyte lacunae canaliculi network (OLCN) in human osteonal bone: The osteocytes are aligned circumferentially around the Haversian canal and are interconnected by a dense canaliculi network. Image dimensions are 388 388 m. The insert shows a 3D-reconstruction of a single osteocyte lacuna obtained with the same technique.

The gained data contains 3-dimensional information on the course of the canaliculi and also on density, shape and distribution of the osteocytes. A projection of 10 such images (3 m volume depth) is shown in Figure 3.14. The data can be evaluated and quantified using a house-made software package developed by Felix Repp (Max Planck Institute of Colloids and Interfaces, Potsdam, Germany) and Philip Kollmannsberger (Max Plank Institute of Colloids and Interfaces, Potsdam, Germany and ETH Zürich, Zürich, Switzerland) which includes a standardized adaptive threshold, a skeletonization algorithm, cell recognication and evaluation, and network analysis (density, orientation, knot distribution,...).

When investigating stained mouse femora we decided to use a 63 oil-immersion objective (HCX PL APO 63x/140-60 OIL) with an airy1 pinhole of 95 51 m and a z-step size of 150 nm according to the higher density of the OLCN compared to humans.

Interpretation of the reflection signal

As mentioned above, the reflection signal of a 488 nm laser beam was simultaneously recorded. This was done also from layers below the surface. Surprisingly, we found that this signal resembles the lamellar structure of the mineralized bone matrix as shown in Figure 3.15. A comparison with high resolution backscattered electron microscopy and light microscope images using a circular polarized differential contrast (CDIC) filter confirmed the position of the lamellar structure. This revealed that reflection-bright lamellae correspond to in-plane orientated collagen fibers. Comparable (but more accurate) data were observed making use of second harmonic generation in CLSM [132].

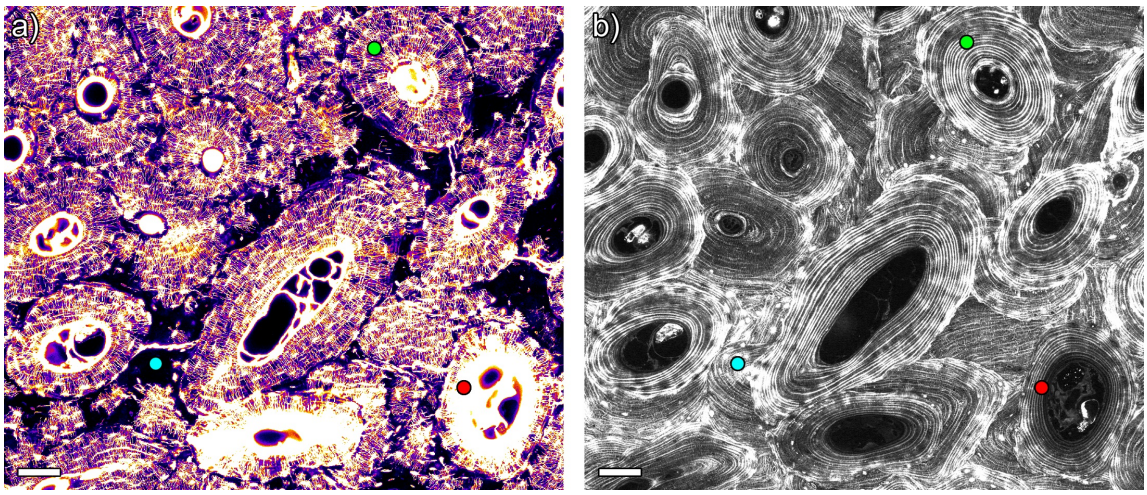

Figure 3.15: Confocal laser scanning microscopy (CLSM) image of a Rhodamine stained human osteonal bone in fluorescence (a) and reflection (b) mode: While the fluorescence image exhibits the OLCN, in the reflection image the lamellar structure of the osteons is visible. Regions which are nicely stained (green dot), non-stained (blue dot), and heavily stained (red dot) are marked (error bars = 100 μm).

It must be noted that the physical explanation for the reflection signal from below the surface is unclear. It might be caused by differences in the refractive index between the lamellae or might be due to multiple scatter events in the case of a beam path perpendicular to the collagen bundle orientation. Since the phenomenon is poorly understood, an accurate evaluation of the lamellae is not taken into account in the network evaluation. Nevertheless, the consistency with the known lamellar structure of bone is striking, thus we used the reflection signal to distinguish between adjacent bone structural units or regions of osteonal and periosteal bone apposition.

Limitations

Despite the power of the Rhodamine staining procedure some limitations need to be discussed in this context. One might have the idea to use the Rhodamine fluorescence signal to measure the diameter of single canaliculi. Unfortunately, this is problematic due to the resolution less

than the canaliculi diameter ($> 378\ nm$ vs. about $200 - 300\ nm$ diameter [35]). Thus in all of our images, the signal originating from a canaliculi appears blurred and broadened making the investigation of the lateral canalicular dimensions impossible.

Another question arises when evaluating the overview images as shown in Figure 3.15. Beside osteons and other regions with a properly stained network (green dot), there are bone packets exhibiting no Rhodamine signal (blue dot). Considering the fluorescence images, it is hard to decide if these areas resemble regions without network, or if the network there is somehow isolated from the blood vessels (or the bone surface) so that no staining fluid penetrates during sample preparation.

On the other hand, some regions exhibit outstanding intense and diffuse fluorescence signals (red dot) making a clear identification of canaliculi impossible. We found that these regions correspond to non-mineralized or very low mineralized bone areas which let us speculate that these are sites where the mineral content (and thus the matrix density) is too low to prevent the ethanol/Rhodamine mixture from penetrating the interfibrillar matrix, resulting in a blurred diffuse signal.

Non-stained regions as well as those with too intense staining are sites where obviously no network analysis can be performed, but nevertheless they resemble sites with exceptional biological conditions providing some information on the mineralized matrix and thus must not be seen as simple staining artifacts.

In the frame of the limitations it should be noted that until yet Raman spectroscopy was not performed on Rhodamine stained samples. It is likely that especially at sites of new bone formation the fluorescence signal superimposes the Raman scattering signal and thus impairs an analysis.

3.7 Visualization of Osteoid using Rhodamine Staining

Beside the characterization of the OLCN, Rhodamine staining revealed to be a tool to visualize non-mineralized tissue like osteoid. As we found that the Rhodamine strongly accumulates in the osteoid, the idea raised if it might be useful to label mineralization defects (e.g. osteomalacia) occurring in various bone diseases and states like hypophospatasia, hypophosphatemia or vitamin D deficiency [133, 134, 135].

Backscattered electron microscopy is an established tool to image the mineralized matrix, but reaches its limits when also the non-mineralized tissue is of interest. Even a simple quantification of the amount of osteoid is usually not possible due to the low contrast between purely organic matrix of osteoid and PMMA. As shown in Figure 3.16, staining with Rhodamine as described in Chapter 3.6 and subsequent imaging with a CLSM, revealed to be comprehensive and compatible to routinely performed backscattered electron microscopy. Both methods can be performed on the same sample surface, even if the sample is coated with carbon. Since,

also the osteocyte lacunae located in the non-mineralized matrix become visible (black voids in Figure 3.16b) and the staining routine seems not to interfere with conventional fluorescent labeling, this approach is planned to be applied on samples where a characterization of mineralization defects is required.

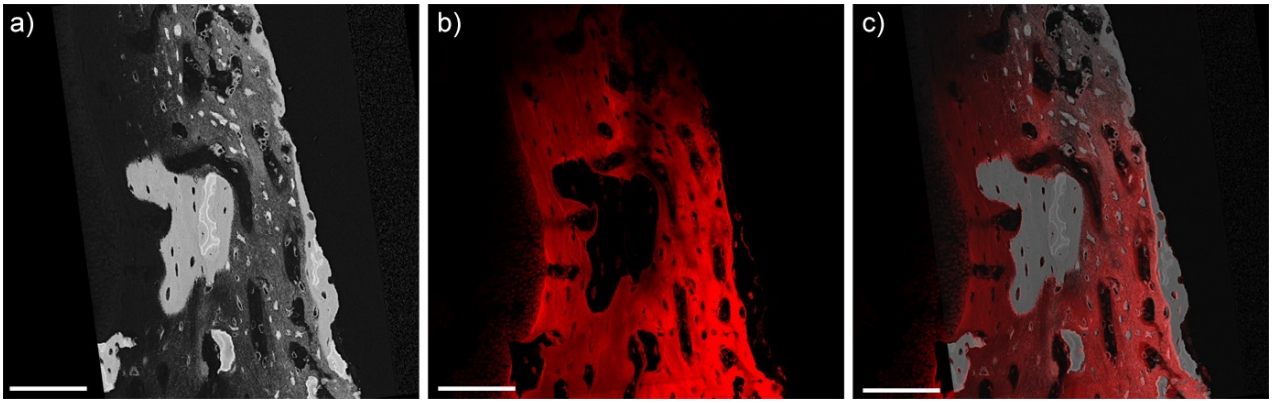

Figure 3.16: Visualization of the non-mineralized bone matrix of a severe mineralization defect in the cortical region of a mouse femur: In the backscattered electron image (a) only the mineralized parts of the defect region are visible. The Rhodamine signal obtained with the confocal scanning laser microscope (CLSM) (b) can be used to characterize the amount of non-mineralized matrix. In (c) both signals are superimposed (error bars = 100 μm).

Chapter 4

Results and Discussion

Methodical developments as described in Chapter 3 were performed to gain new insight into the bone mineralization process in health and disease. The comprehension of bone development and composition is critical for the characterization of physiological and pathophysiological processes. Analyzing bone samples from animal models (in our case Sost-knockout (*SostKO*) mice and a model for Osteogenesis Imperfecta treated with Sclerostin antibodies (SclAB)) with established and newly developed methods yields to valuable data focusing on bone quality properties additionally to information on bone mass and architecture. The presented combination of quantitative backscattered electron microscopy (qBEI), Raman microspectroscopy, energy dispersive X-ray analysis (EDX) and confocal laser scanning microscopy (CLSM) provides access to the degree of mineralization and mineral crystal properties, the composition of organic matrix, and the elemental composition at predefined regions of interest (ROI) [16, 14, 18]. Pathological conditions or treatment potentially alter these quantities, thus causing changes in the quality of the bone material independent of the overall bone mass and structure [50, 25]. As it is reported bone quality essentially contributes to bone strength and is thus is closely linked to fracture risk [50, 25].

For the development of new therapeutic drugs it is essential to monitor not only the change in bone quantity, but also to focus on the properties of bone to help estimating long-term or side effects. In this sense also the examination of the osteocyte lacuna canaliculi network (OLCN) of human bone samples will lead to important information as this network is reported to play a major role in mechanosensation, for the reaction to changes in systemic ion concentrations, and for the endocrine character of bone [4, 80, 79, 23].

This motivates the application of newly developed/extended and established methods to characterize basic mechanisms of bone matrix mineralization of human and murine bone samples. For a common interpretation of qBEI and Raman outcomes, in the frame of this thesis for the first time a head-to-head comparison of these two methods was performed on the same ROIs. This approach revealed a fundamental relationship between the Ca content as determined by qBEI and the $mineral/matrix$ ratio elucidated by Raman spectroscopy. The so gained relationship is the topic of Chapter 4.1 where identical secondary mineralized osteons and interstitial regions were analyzed with both methods.

There is some evidence that these very early stages of bone formation are crucial for a normal development of organic matrix and for a proper mineralization of it [136]. Thus, another focus of this thesis is on the tissue close to these regions, where a rapid increase in mineral content is reported [14]. The corresponding approach using EDX is described in Chapter 4.4 where mineralization fronts and the adjacent tissue were analyzed with respect to the local concentration of major and minor elements. The investigated sites are regions of new bone apposition and thus reflect a critical state for bone development. However, these sites resemble only a minor fraction of heterogeneous bone tissue.

Taking into account that on the micron scale, bone is not homogenous, it becomes obvious that for the comparison between samples the way of selecting the regions of interest must be chosen with respect to the addressed questions. qBEI measurements at regions normalized for tissue age as done in our study on SostKO mice (Chapter 4.2.2) revealed changes in the mineralization kinetics (N. Hassler*, A. Roschger*[1] et al. [18]).
In contrast to this approach, whole bone area qBEI mappings and evaluation led to results depending on the bone turnover with a maximum of explanatory power on the current mineralization pattern. In this sense the analysis of our study on SclAB treated mice was performed (A. Roschger et al. Bone 2014 [21]) (Chapter 4.2.3).

In these two studies mineralization is characterized in conditions of increased bone formation due to elevated osteoblastic activity and in the case of the second study also a model of Osteogenesis Imperfecta is included.

As described in the introduction (Chapter 2.1.4) the role of osteocytes cannot be neglected when discussing matrix mineralization. Beside others the osteocyte network is supposed to play a major role in Ca and Phosphate homeostasis due to their suspected ability to alter the bone composition of their environment [22]. For this reason another study was performed focusing on the local distributions of major (Ca, P) and minor (Mg, N, K, S, Cl) elements with respect to various OLCN types in human compact femoral bone (Chapter 4.3).

4.1 Correlation of Bone Matrix Mineralization Measured by Quantitative Backscattered Electron Microscopy (qBEI) and Raman Micro-Spectroscopy

This chapter describes the comparison between the *mineral/matrix* parameter measured by Raman micro-spectroscopy and weight percent Ca as determined by qBEI. The study is a fundamental work helping to interpret the two variables in the context of each other and is already published in the Journal of Biomedical Optics by A. Roschger et al. [17]. Figures, selected paragraphs and considerations presented in this chapter are also part of this publication.

[1] Both authors contributed equally to this paper and are listed in alphabetical order.

Raman spectroscopy and vibrational spectroscopy in general became a powerful tool for the investigation of bone material and offers access to chemical properties of the collagen matrix and the mineral phase. The physical basics of Raman spectroscopy are described in Chapter 2.2.3.
Despite the fact that there are also other methods with similar spatial resolution providing data closely connected to the degree of mineralization (like EDX and qBEI) a head to head comparison of Raman micro-spectroscopy and these methods was not performed yet. In the current project we applied both, Raman micro-spectroscopy and qBEI, to identical ROIs in healthy human compact bone undergoing secondary mineralization to elucidate the principal relationship between the $mineral/matrix$ ($\nu_2PO_4/amideIII$) ratio (Raman) and $wt\%Ca$ (qBEI). The results will allow a more accurate interpretation for every study where qBEI and Raman spectroscopy are applied on the same spots. Hence, the addressed questions are:

1. How is the $mineral/matrix$ ratio linked with the Ca content as measured by qBEI?
2. Can the technical variation be separated from biological heterogeneity?
3. What is the statistical power of each technique?

4.1.1 Selection of Measurement Regions

To answer these questions, we analyzed 99 ROIs of $20 \times 20\ \mu m^2$ located inside osteons of the femoral midshaft of three healthy women with respect to a large variation in mineralization between the ROIs (Table 3.1 Sample #1, #2, #3). The samples were provided by the department of Forensic Medicine of the Medical University of Vienna and were prepared as described in Chapter 3.1 and [95]. The same ROIs were analyzed with both methods and an average $wt\%Ca$ value was derived for every ROI using qBEI (DSM962, Oberkochen, Germany) while 25 measurement spots were acquired to determine the $mineral/matrix$ Raman parameter as shown in Figure 4.1.

4.1.2 Results

Recording and evaluation of the Raman spectra was performed by colleagues in our institute supervised by Elephterios Paschalis, PhD. A precise description of the measurement protocol and the statistical analysis can be found in [95]. Additionally to the measurements also theoretical estimations were performed to derive the expected correlation between the gained parameters as follows:

Theoretical considerations to derive an estimated correlation between qBEI and Raman parameters
Figure 4.1d shows the correlation between the $mineral/matrix$ and the $wt\%Ca$ parameters. The fact that a linear extrapolation of the data misses the origin of the graph by far, let assume that the overall relationship between these parameters is not directly proportional. To check if this observation is expected from a theoretical point of view, mathematical estimations

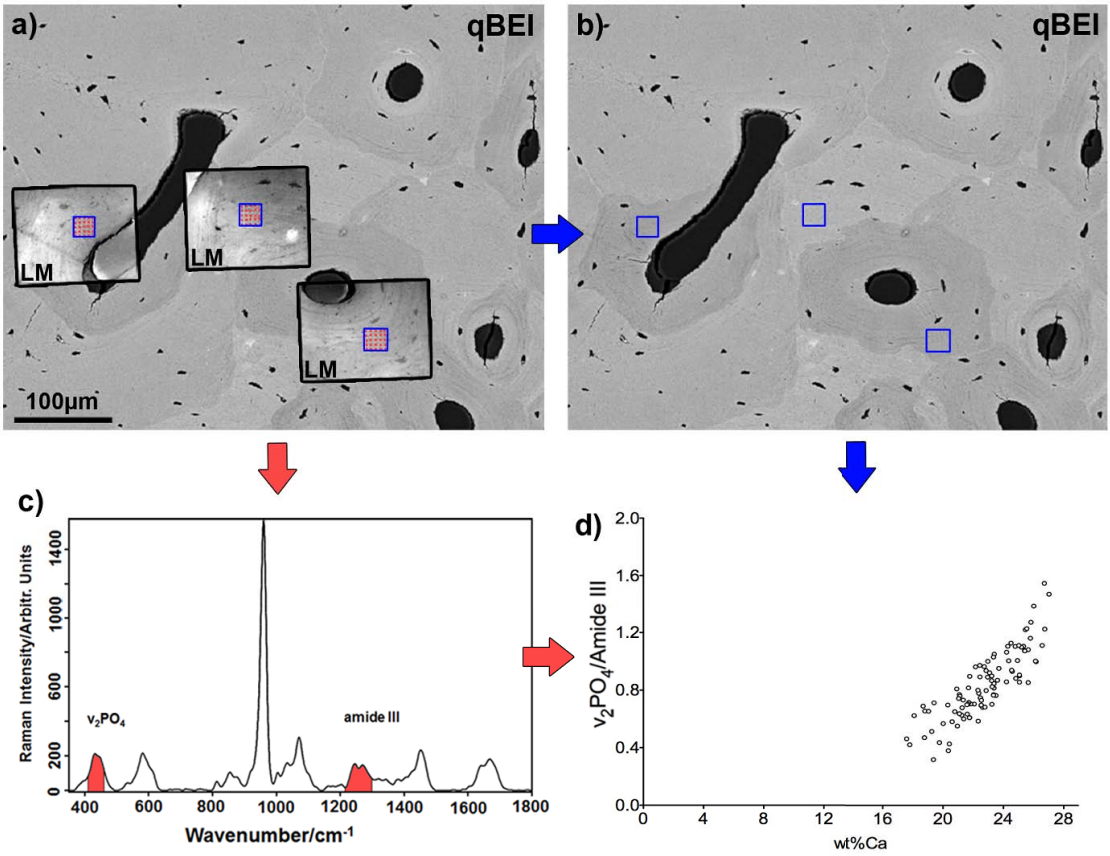

Figure 4.1: (a) Overview of a quantitative backscattered electron imaging (qBEI) image with overlaid light microscope images: Light microscope images (LM) were taken at the Raman device for the documentation of measurement points (red dots). The blue boxes designate the regions of interest (ROI) for qBEI analysis. (b) qBEI analysis: Orientations and positions of the blue boxes were transferred from (a) to mark the exact positions of the ROIs that were considered for qBEI analysis. (c) Raman analysis: representative Raman spectrum of human bone; the $_2\ PO_4$ and the $amideIII$ peaks (red) were used to derive the $mineral\ \ matrix$ ratio. (d) Comparison of Raman and qBEI results: $mineral\ \ matrix$ assessed by Raman versus $wt\%Ca$ measured by qBEI. Each circle represents the average value of one $20\quad 20\quad m^2$ ROI (blue boxes in (a) and (b)).

were performed taking into account the different natures of Raman and qBEI parameters and following simplifications:

1. For all estimations the PMMA content is neglected. This seems to be reasonable since the volume of PMMA-filled canaliculi account for less than 1% of the mineralized matrix [85]. Also only PMMA peaks close to the detection limit were observed in the Raman spectra.

2. For this first approximation the Ca/P ratio is assumed to fit the theoretical value of pure Hydroxyapatite (HAP) ($Ca_{10}(P0_4)6(OH)_2$) of 1.67.

3. All the Phosphate (PO_4) and Ca content is assumed to be bound in HAP implying that Ca and PO_4 contributions from phosphorylated non-collagenous proteins or protein-bound Ca only account for minor quantities.

In the following a set of abbreviations is used:

- N_{PO_4}: number of the PO_4 groups per unit volume
- $N_{amiedIII}$: number of the $C-N$, $N-H$ groups per unit volume
- $m_{mineral}$: mass of mineral per PO_4 group
- $m_{amideIII}$: mass of organic matrix per $C-N$, $N-H$ group
- $wt\%mineral$: weight percentage of the mineral crystal
- $R_{amideIII}$: molecule-dependent parameter, including all constants and vibrational properties of the $amideIII$ group
- R_{PO_4}: molecule-dependent parameter including all constants and vibrational properties of the PO_4 group

According to simplification (1), bone is considered to be a two-component system, consisting of a mineral and an organic phase. Hence, $wt\%mineral$ is defined as the mass of mineral per volume ($N_{PO_4} \cdot m_{mineral}$) divided by the total mass (Formula 4.1). Simplification (3) includes that a direct conversion between $wt\%Ca$ as measured by qBEI and $wt\%mineral$ is straightforwardly calculated as in Reference [95] ($wt\%mineral = 2.51 \cdot wt\%Ca$).

$$2.51 \cdot wt\%Ca = wt\%mineral = \frac{N_{PO_4} \cdot m_{mineral}}{N_{PO_4} \cdot m_{mineral} + N_{amideIII} \cdot m_{amideIII}} \tag{4.1}$$

This can be transformed to

$$\frac{wt\%mineral}{100 - wt\%mineral} = \frac{N_{PO_4} \cdot m_{mineral}}{N_{amideIII} \cdot m_{amideIII}} \tag{4.2}$$

The left side of the equation (Formula 4.2) can be derived from qBEI measurements and corresponds to a ratio between the mineral phase ($wt\%mineral$) and the non-mineral (organic)

matrix ($100 - wt\%mineral = wt\%organic$). The right side includes parameters depending on the vibrational units accessible by Raman spectroscopy. Thus the goal is to derive a relationship between this term and the $mineral/matrix$ Raman ratio:

The intensity of Raman scattered light $I(v)_R$ is proportional to the primary beam intensity I_0 and the number of scattering molecules N:

$$I(\nu)_R = \frac{2^4\pi^3}{45 \cdot 3^2 \cdot c^4} \cdot \frac{I_0 \cdot N \cdot h(\nu_0 - \nu)^4}{\mu \cdot \nu(1 - e^{-h\nu/kT})} \cdot \left[45(\alpha_a)^2 + 7(\gamma_a)^2\right] \tag{4.3}$$

All other terms, including the speed of light (c), Planck's constant (h), molecular vibration frequency (ν), laser excitation frequency (ν_0), reduced mass of the vibrating atoms (μ), Boltzmann constant (k), absolute temperature (T), mean value invariant of the polarizability tensor (a_α), and the anisotropy invariant of the polarizibility tensor (γ_a) can be summarized to the molecule-dependent parameters $R_{amideIII}$ and R_{PO_4}, respectively. These definitions allow simplifying the $mineral/matrix$ ratio as shown in Formula 4.4. According to the confocal experiment setup, the measurement volume V can be treated as constant.
Hence it follows for a defined vibration x:

$$I_x = I_0 \cdot V \cdot R_x \cdot N_x \tag{4.4}$$

and consequently

$$\frac{mineral(\nu_2 PO_4)}{matrix(amideIII)} = \frac{I_{PO_4}}{I_{amideIII}} = \frac{I_0 \cdot V \cdot R_{PO_4} \cdot N_{PO_4}}{I_0 \cdot V \cdot R_{amideIII} \cdot N_{amideIII}} = \tag{4.5}$$

$$= \frac{R_{PO_4} \cdot N_{PO_4}}{R_{amideIII} \cdot N_{amideIII}} = \frac{R_{PO_4} \cdot m_{amideIII}}{R_{amideIII} \cdot m_{mineral}} \cdot \frac{N_{PO_4} \cdot m_{mineral}}{N_{amideIII} \cdot m_{amideIII}} \tag{4.6}$$

Hence, we derived the desired association between Raman and qBEI parameters:

$$\frac{mineral(\nu_2 PO_4)}{matrix(amideIII)} = Slope \cdot \frac{wt\%mineral}{100 - wt\%mineral} \tag{4.7}$$

with

$$Slope = \frac{R_{PO_4}/R_{amideIII}}{m_{mineral}/m_{amideIII}} \tag{4.8}$$

The value of the slope remains unknown. $R_{amideIII}$ and R_{PO4} include unknown contributions from the optical parameters, Raman tensors, and measurement geometry, which are hardly accessible. Also regarding $m_{amideIII}$, detailed information on the composition of organic matrix is missing. Thus the slope-value cannot be derived numerically. Nevertheless, the theoretical consideration made above lead to two remarkable predictions as also described in Reference [17]:

1. A linear correlation between the $mineral\ \ matrix$ ratio (Raman) and $wt\%mineral\ \ 100\ \ wt\%mineral$ (qBEI) is expected. The mathematical transition from $wt\%mineral\ \ 100\ \ wt\%mineral$ to $wt\%Ca$ includes a conversion from a ratio to a fraction. Therefore, linearity is not preserved when deriving a theoretical correlation between $mineral\ \ matrix$ and $wt\%Ca$.

2. Linear direct proportionality between the $mineral\ \ matrix$ ratio and $wt\%mineral\ \ 100\ \ wt\%mineral$ is expected as a result of the absence of an additive constant (offset) in Formula (4.7). Thus, a mathematical extrapolation of the measurements is expected to go through the origin after transforming the x-axis of Figure 4.1d from $wt\%C$ to $wt\%mineral\ \ 100\ \ \ wt\%mineral$.

Regarding "Prediction 1" we found consistently that linearity of the measurement distribution slightly increased due to the described transformation to the x-axis.
As expected from "Prediction 2" we found that the x-axis transformation from $wt\%Ca$ to $wt\%mineral\ \ 100\ \ \ wt\%mineral$ leads to linear direct proportional correlation. The mathematical extrapolation of the regression line goes through the origin within the 95% confidence bands (Figure 4.2). These behaviors of the qBEI and Raman parameters are in excellent agreement with the theoretical considerations made above.

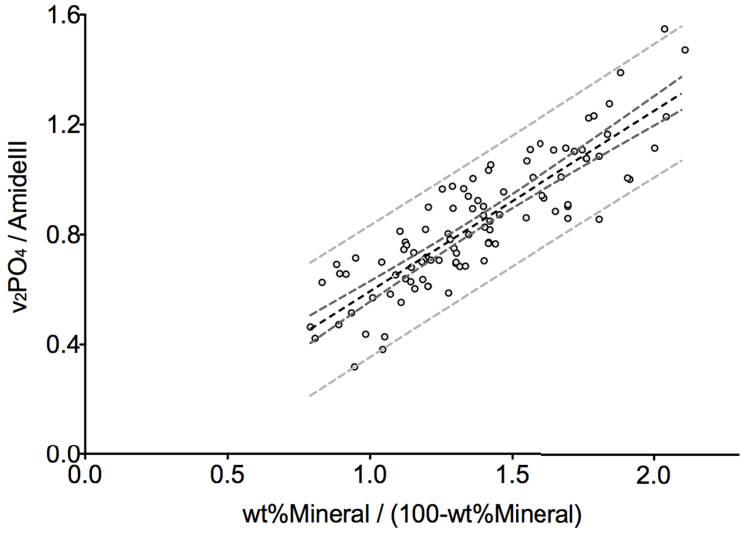

Figure 4.2: Correlation of $mineral\ \ matrix$ ($_2PO_4\ \ amideIII$) assessed by Raman and $wt\%mineral\ \ 100\ \ \ wt\%mineral$ measured by qBEI: Each data point refers to a ROI. Additionally, the linear regression line (black dashed line), the 95 % confidence bands of the slope (dark dashed line), and the 95 % prediction bands (bright dashed line) are shown. As predicted by theoretical estimations, the plotted data are correlated linearly ($R^2 = 0\ 75$).

Calculations on the influence of the *Ca/P* ratio of bone mineral

From a theoretical point of view it is possible to estimate changes in the $mineral\ \ matrix$ ratio in the case of a changed mineral composition (assuming relatively unaltered organic matrix)

like the influence of other mineral phases or the degree of the apatitic crystal lattice ion substitutions. Extending Formula 4.7, we now introduce a parameter ϕ, which depends on a hypothetical mineral composition and describes the relation between $wt\%Ca$ and $wt\%Mineral$. ϕ equals 2 51 for pure HAP and changes due to the properties of the mineral [95].

$$\frac{mineral(\ _2PO_4)}{matrix(amideIII)} = \frac{wt\%Ca\ \ \phi}{100\ \ \ wt\%Ca\ \ \phi}\ \ _R\ \frac{m_{amideIII}}{m_{mineral}} \quad \text{with} \quad _R = \frac{R_{PO_4}}{R_{amideIII}} \tag{4.9}$$

The last term of Formula 4.9 can be summarized to the factor K.

$$K = \ _R\frac{m_{amideIII}}{m_{mineral}} \tag{4.10}$$

Figure 4.3 illustrates the *mineral matrix* ratio calculated from arbitrarily chosen $wt\%Ca$ values for three different K. K_2 was chosen to fit the results of our measurements. Resulting from the approximation that mineral consists of pure HAP ($Ca\ \ P = 1\ 67$), the range between the two dashed lines reflects the difference between a hypothetical 1:1 mixture of HAP and Octacalciumphosphate ($2Ca_4H(PO_4)_3\ \ 2\ 5H_2O$) ($Ca\ \ P = 1\ 5$, $K_1 = 0\ 63$, $\phi = 2\ 70$) and type B-carbonated HAP with $Ca\ \ P = 1\ 9$ ($Ca_{9\ 5}(PO_4)_5(CO_3)(OH)_4$), $K_3 = 0\ 54$, $\phi = 2\ 49$).

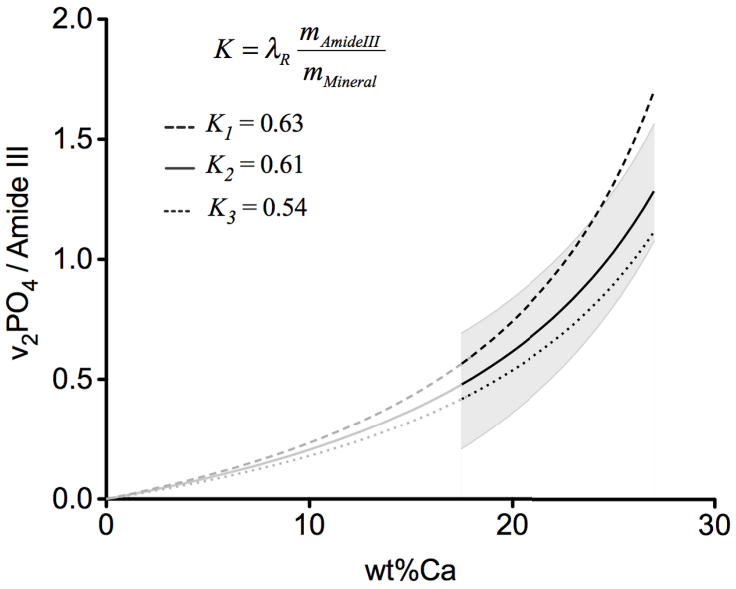

Figure 4.3: *mineral matrix* ($_2PO_4$ *amideIII*) calculated from arbitrary $wt\%Ca$ values with variations in K. The K-value includes unknown parameters like $R_{amideIII}$ and R_{PO_4} and the exact composition of the collagen and the mineral phase. K_2 was chosen to fit the measurements. Using the approximation that bone consists of pure HAP, the bandwidth between the two dashed lines reflect the difference between a 1:1 mixture of Octacalcium Phosphate ($Ca\ \ P = 1\ 5$) and carbonated HAP with $Ca\ \ P = 1\ 9$. The gray region reflects the converted 95 % prediction bands. The validity of these graphs for the low mineralized regions remains unclear.

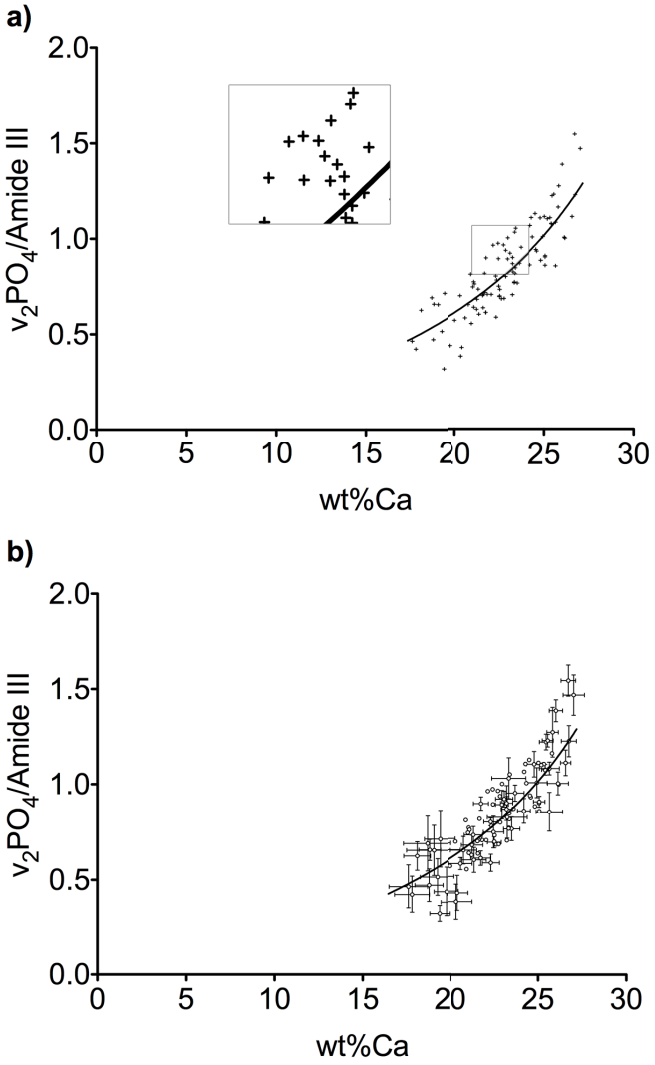

Figure 4.4: (a) Technical variability: *mineral matrix* ($_2PO_4$ *amideIII*) versus *wt%Ca*. The bars of the crosses are 2 of the technical variation. The technical variations were derived for both methods by obtaining the same region for approximately 20 times. (b) Intraindividual variability within a 20 20 *m* ROI. Crosses symbolize the observed standard deviations (SDs) within each measurement field for Raman and qBEI. To improve legibility not all data points are shown with error bars.

Technical variations vs. biological variations

Despite the high linear correlation, the question lingers whether the deviations from the regression line in Figure 4.2 are due to technical variations of the measurement setup, or due to biological heterogeneities influencing Raman and qBEI signals in different manner. To determine the influence of these factors, in Figure 4.4 error bars are added to the data points representing 2 (Raman: 0 0088 *mineral matrix*, qBEI: 0 099 *wt%Ca*) of the technical variation as described in Reference [17]. For both, Raman and qBEI, the technical variability causes only minor uncertainties. Thus we conclude that the technical variations are too low to substantially contribute to the deviation of the data points from the regression line.

In Figure 4.4b the error bars illustrate the measured standard deviation (SD) within each ROI. Therefore, error bars in the y-direction represent the SD of the *mineral matrix* ratio of the 25 measurement points of the corresponding region. To achieve comparable statistics between Raman and qBEI, within every ROI average gray values of all 5 5 pixel bins were

used to calculate the standard deviations for qBEI. Hence, for Raman and for qBEI 25 values per ROI are used to determine the biological variances, but nevertheless the statistical power is different. This is due to the fact that for qBEI each value itself is the average over a field of 5×5 pixels. As a consequence, this procedure reduces the noise in the qBEI causing reductions of the SDs and the coefficients of variation (COV).

The comparison of measured variations with technical fluctuations (Figure 4.4) leads to the conclusion that the variations within a $20 \times 20\ \mu m^2$ ROI are predominantly due to a biological variation rather than fluctuations caused by the measurement process.

A more accurate analysis of the SDs strongly suggests a dependency on the degree of mineralization ($wt\%Ca$) for both qBEI and Raman. Low mineralized ROIs ($< 21\ wt\%Ca$) have significantly higher SDs in both methods ($p < 0.0001$) compared to the ROIs with a Ca content between 21 and 26 $wt\%$. Interestingly, for high mineralized ROIs ($> 26\ wt\%Ca$) the SD deviation in $wt\%Ca$ remains unchanged ($p = 0.528$), while the SDs of the $mineral/matrix$ values increase significantly compared to those with medium mineral content ($p = 0.014$). The results of this analysis are shown in Table 4.1. When the COVs are calculated, the significant differences of the variations between the low and the medium mineralized regions remain ($p < 0.0001$) while the COVs of the medium and high mineralized regions are equal for Raman ($p = 0.708$) and qBEI ($p = 0.959$) (Table 4.1).
The significances for the qBEI outcome were also calculated with the same results for the $wt\%mineral$-ratio as introduced in Formula 4.2, so that changes due to the conversion to $wt\%Ca$ can be excluded as confounding factors.

Table 4.1: Median standard deviations (SD) and coefficients of variation (COV) within the regions of interest for Raman and qBEI measurements for three ranges of different mineralization: The values of the SDs correspond to the error bars indicated in Figure 4.4.
* $p < 0.0001$ vs. low mineralized ($< 21\ wt\%Ca$), ° $p < 0.05$ vs. high mineralized ($> 26\ wt\%Ca$)

$wt\%Ca$ (qBEI) - Range	$< 21\ wt\%Ca$ ($n = 19$)	$21 - 26\ wt\%Ca$ ($n = 73$)	$> 26\ wt\%Ca$ ($n = 7$)
Raman - SD ($I_{\nu_2 PO4}/I_{amideIII}$)	0.0924	0.0482 * °	0.0815
qBEI - SD (wt%Ca)	0.796	0.426 *	0.427
Raman - COV	0.1807	0.06096 *	0.06035
qBEI - COV	0.042	0.018 *	0.016

Interindividual variations of the regression slopes
The statistical evaluation (linear regression analysis) of the inter-individual differences showed that neither slope nor intercept with the y-axis of the linear regressions were significantly different for all three samples.

4.1.3 Discussion and Conclusion

In agreement with the theoretical evaluation, no direct proportionality between $wt\%Ca$ (measured by qBEI) and $mineral/matrix$ (measured by Raman) was found, but as expected this was the case for $wt\%mineral/(100-wt\%mineral)$ (derived from $wt\%Ca$) and $mineral/matrix$ in bone regions undergoing secondary mineralization. All the presented data as well as the correlation refer to these regions and may not extrapolate to regions with low mineral content close to the mineralization front as discussed below. It is demonstrated that the deviations from the linear regression line are predominantly due to biological heterogeneity. Therefore we now address the various sources of these uncertainties:

Variability between the ROIs
Our study links the $mineral/matrix$ ratio ($\nu_2PO_4/amideIII$) measured by Raman microspectroscopy with $wt\%Ca$ as assessed by qBEI, in healthy human bone, exclusively in the secondary mineralization phase. The Ca content of the analyzed measurement fields ranges from 17.6 $wt\%Ca$ up to 27 $wt\%Ca$ covering most of the Ca concentration range present in human bones (Figure 4.1d). The narrow regions of primary mineralized bone, that occur next to active mineralization fronts, were excluded from this study. A transformation of the x-axis from $wt\%Ca$ to $wt\%mineral/(100-wt\%mineral)$ (termed $wt\%mineral$ ratio) results in Figure 4.2. The linear correlation and its intercept with the x-axis close to the origin (which lies in the 95% confidence band) are in agreement with a theoretical estimations when approximating the mineral phase using pure HAP (Figure 4.2).

When comparing the technical and the observed variability for both methods, we found that the scattering of the data points in Figure 4.2 is primarily related to the biological heterogeneity of bone material. Even within a $20 \times 20\ \mu m^2$ region of interest (ROI), that was placed inside a single bone structural unit, the material appears heterogeneous, causing variations in the measurements higher than the technical uncertainties (Figure 4.4). As a consequence, the deviation from the regression line is caused by local changes in the material properties. Therefore the question remains, as to what extent do changes in the sample composition influences the results.

Influence of the Ca/P of bone mineral
Often, the Ca/P ratio is used to characterize the mineral composition but for human bone tissue, Ca/P values vary between 1.6 and 1.7 [137]. Other studies using EDX measured Ca/P weight percent ratios between 2.1 and 2.2, which corresponds to the Ca/P ratio range mentioned above [138, 130]. This variability is likely due to changes in the apatite composition due to type A and type B carbonate substitutions as well as Mg, Na or K ones, or even the presence of Ca-ion lattice vacancies in the apatite crystal [139, 140, 141, 142]. Of course, alterations in the mineral composition or phase change both, Raman and qBEI outcomes. The expected range of the measurements according to changes in the Ca/P ratio are estimated in Section 4.1.2 for a hypothetical 1:1 mixture of HAP and Octacalcium Phosphate ($Ca/P = 1.5$), as well as for type B-carbonated HAP ($Ca/P = 1.9$).

The Ca/P ratios of 1.5 and 1.9 in this model may reflect exaggerated deviations in the mineral

composition from pure HAP and likely don't relate to appreciable phases occurring in bone. Nevertheless, it reveals in which way changes in the mineral are altering the correlation between $wt\%Ca$ and $mineral/matrix$. Since the gray shaded region in Figure 4.3 corresponds to the 95% confidence interval from the measured scatter of $mineral/matrix$ and $wt\%Ca$ values in Figure 4.2, it can be speculated that the variability between and within the ROIs originates from distinct local changes of the mineral composition. However, the origin of these changes remains unclear. Fluctuations in the degree of carbonate substitution, the presence of mineral phases other than HAP, or Ca substitution with ions such as Mg, K are plausible explanations. This is in agreement with previous studies showing that the chemical composition of HAP changes as a function of the location (thus tissue age) within an osteon [112, 140].
Of course it cannot be excluded that changes in the organic matrix also contribute to the observed variability. For example, phosphorylated organic molecules potentially increase the local PO_4 content, and protein bound Ca may also contribute to our results.

Variability within a ROI
We observed a significant increase of the standard deviations (SD) in the lower mineralized ROIs for both methods (Table 4.1). These regions (< 21 $wt\%Ca$) were located in osteons with ongoing bone apposition (mineralizing surfaces), which were identified by a distinct gradient of mineral content down to the level of pure osteoid. In such young osteons the degree of mineralization increases as a function of distance to the Haversian channel. This causes a gradient of mineralization within the ROIs and therefore enhanced SDs for the outcome of both methods (Table 4.1). Also the local biological variance might be increased in very young bone. The fact that these differences remain significant when normalizing the SDs for the mean value and calculating the coefficient of variation (COV) supports these statements.
The variability of the Ca content within the ROIs in the high mineralized osteons or interstitial regions (> 26 $wt\%Ca$) remained unchanged. Interestingly, the variability of the $mineral/matrix$ ratio increased significantly in these regions. In contrast to that a statistical analysis of the COVs of these regions showed no significant differences between medium and high mineralized ROIs. Therefore, it can be assumed that for Raman the variability in the $mineral/matrix$ ratio is a function of degree of mineralization and tissue age, unlike qBEI.
Regarding qBEI, it was previously reported that there are slight variations in the mineralization and also in the mechanical parameters between adjacent lamellae of osteonal bone, likely contributing to the observed heterogeneity within a 20×20 μm ROI [32].

Interpretation of the Slopes
As the curves in Figure 4.3 correspond to straight lines with various slopes in the $mineral/matrix$ vs. $wt\%mineral$ diagram in Figure 4.2, distinct changes in the slope of the regression line would indicate fundamental changes in the tissue composition of the secondary mineralized regions. Therefore, this type of measurement may prove to be an extra tool for the investigation of bone quality in diseased bone as it is reflective of altered mineral composition, and may also prove to be a key factor bridging altered bone quality as assessed by Raman spectroscopy with altered bone mineral density distribution. In future, together with the Raman evaluation of the $\nu_2 PO_4/CO_3$ ratio (a measurement for the degree of carbonate incorporation) and EDX (quantification of the Ca/P ratio and the Na and K content) we expect to be able to check whether an altered slope is due to a different mineral composition, or if abnormal composition

of the organic matrix must be considered.
In this study the variations in the slopes between the individuals showed no significant differences. However, due to the low sample number and the study design, slight changes in the slopes might not reach significance. The presented techniques can be used to obtain data from a larger healthy reference cohort to generate a more robust tool for clinical investigation. It must be noted that in this case, the acquisition settings must be the same for the measurements on different samples assuring comparability of the gained data.
Nevertheless, the comparison of measurements on diseased bone with the data shown in this study might help to understand changes in the mineralization process, if distinct deviations from the presented correlation are observed.

Raman measurements are often performed close to the regions of new bone formation, between fluorescent labels, marking young regions with strictly defined tissue age [55] - a tissue type that is not covered in the current study. The combination of Raman and qBEI as used in this study but closer to the mineralization front provides a promising topic for future investigation. Thus, the very early stages of bone formation can be analyzed. The base for such an analysis is an extremely precise matching of the points of measurements between both methods, which is still challenging (at least 1 μm accuracy). Superimposing optical and qBEI images can most likely not achieve this. Nevertheless, correlation of the Raman parameters with the tissue age or Ca concentration is expected to yield significant insights into the evolution of bone mineralization in health and disease.

The interpretation of the correlation between Raman and qBEI data close to the mineralization front is expected to become even more complicated because in these regions the chemical composition of the measurement volume changes systematically as a function of the location, and the makeup of the organic matrix is also rapidly changing. In these narrow bands the Ca content as measured by qBEI and also the $mineral/matrix$ ratio increase drastically with the distance from the osteoid surface [55, 113, 14]. How the regression curves (Figure 4.1d and Figure 4.2) behave in these interface regions, remains unknown. Deviations from the linear regression are expected according to an increase of the PMMA content linked to the higher microporosity. Additionally parameters like $protoglycan/amideIII$, mineral crystalinity or relative lipids content are reported to change at mineralization fronts as a function of distance to the Haversian canal [56]. Once a technique for precise matching of Raman and qBEI measurements is developed, such studies can help to elucidate underlying mechanisms of tissue mineralization.

Conclusion
Through combination of Raman micro-spectroscopy and qBEI $\nu_2PO_4/amideIII$ Raman intensities ($mineral/matrix$ ratio) data were linked to Ca content ($wt\%Ca$) data. A linear correlation of $mineral/matrix$ (Raman) with the transformed $wt\%mineral/wt\%(OrganicMatrix)$ (qBEI) was observed in healthy human bone matrix being in secondary mineralization phase. This type of correlation is in agreement with theoretical considerations. The local variability of both parameters inside bone structural units is caused by biological heterogeneity and was found to depend on the degree of mineralization. The combination of Raman and qBEI provides a novel approach for the detection of changes in composition of bone tissue that might

help to understand the physiological and patophysiological mineralization process of bone.

4.2 Bone Mineralization in Sclerostin Deficiency

Beside bone mass and architecture, properties of the organic matrix as well as bone mineralization seem to be key factors characterizing bone quality and mechanics [25]. Although these parameters are not easily accessible, especially for the development of new drugs to treat Osteoporosis and other bone diseases, the material properties need to be taken into account to give a comprehensive description of a drug, disease, or gene defect impact. In this sense, the focus of this chapter is on the material properties of two mouse models related to a novel approach for osteoanabolic treatment of Osteoporosis, Osteogenesis Imperfecta and maybe also other bone diseases, namely the administration of SclAB [143]. Significant results were gained using routines and methods developed during these studies as described in Chapter 3.4.

This chapter is based on a study presented as talks and posters on national and international conferences [2][3][4][5] and two further studies already published by N. Hassler*, A. Roschger*[6] et al.; J Bone Miner Res, 2014 [18] and A. Roschger et al.; Bone, 2014 [21]. Figures, selected paragraphs and considerations presented in this chapter were also part of these publications.

In the first of the studies the BMDD of *SostKO* mice was obtained in various anatomical sites using qBEI. For the interpretation of the so-gained observations, a more detailed analysis was required. This was done in the second study, which revealed altered mineralization kinetics and changed organic matrix properties in *SostKO* mice lacking sclerostin, at the endocortical site of the femoral diaphysis using qBEI and Raman spectroscopy as introduced in Chapters 2.2.3 and 4.1. The third study is a logical follow-up project, describing the mineralization pattern of transgenic and wild-type mice being a model for Osteogenesis Imperfecta treated with SclAB. These studies were performed in collaboration with Michaela Kneissel (employed by Novartis Inc, Basel, Switzerland) and Frank Rauch (Shriners Hospital for Children, Montreal, Canada) (Chapter 4.2.3). While qBEI measurements and image processing routines were performed in the frame of this thesis, Raman measurements and peak evaluation were done by colleagues in our institute (Ludwig Boltzmann Institute for Osteology) supervised by Eleftherios Paschalis, Phd.

[2] A. Roschger et al; The mineralization kinetics of endocortical bone is altered in Sost knockout mice; First LBG Meeting for Health Sciences; December 2013; Vienna, Austria; poster presentation (1.14)

[3] A. Roschger et al; Einfluss von niedrigem Sclerostin-Level auf die Knochenmasse und Knochenmaterialqualität; Osteologie 2013; March 2013; Weimar, Germany; invited talk

[4] A. Roschger: Combination of Quantitative Backscattered Electron Imaging with Confocal Laser Microscopy: A Powerful Tool for the Evaluation of Bone Matrix Mineralization Kinetics, XIIth Congress of the International Society of Bone Morphometry; American Society of Bone and Mineral Research; October 2012; Minneapolis, USA.; oral präsentation

[5] A Roschger: The Mineralization Kinetics of Endocortical Bone is Altered in Sost Knockout Mice; October 2012; Minneapolis, USA; poster presentation (MO0269)

[6] *Both authors contributed equally to this paper and are listed in alphabetical order.

4.2.1 Bone mineralization density distribution (BMDD) of *SostKO* mice

We analyzed longitudinally ($n = 9$) cutted blocks of the femur diaphysis of *SostKO* mice and corresponding sections ($n = 11$) of wild-type littermates by qBEI. A further description of the samples is given in Chapter 3.2 and in Reference [74]. These specimens were used to gain the BMDD in cortical and cancellous regions (Figure 4.5). A remarkable increase in bone mass in the *SostKO* mouse model was observed, which is consistent with previous descriptions [74, 77]. Figure 4.6 shows representative examples of BMDD distributions of cortical (a) and cancellous regions (b).

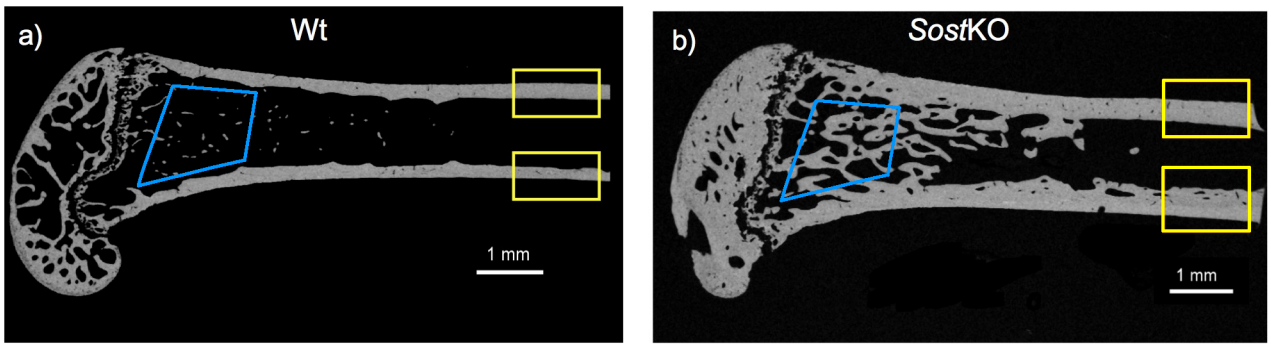

Figure 4.5: Longitudinal sections of distal femora of a wild-type mouse (a) and a *SostKO* mouse (b): The labeled regions were considered for quantitative backscattered electron analysis (qBEI).

While we observed a distinct shift of the BMDD histogram towards lower mineralization in the cortical bone of *SostKO* mice, the opposite was observed for cancellous regions for both parameters linked to the degree of mineralization (Table 4.2). Hence, the question lingers how these apparently contradictious observations can be interpreted. While the increase in mineralization in the cancellous region is supposed to be due to increased bone mass, and therefore to an elevated average tissue age, the reason for the shift towards lower mineralization in the cortical remains unclear so far. To address this point, transversal sections of another cohort was evaluated with respect to mineralization kinetics and organic matrix properties comparing regions of the same tissue age.

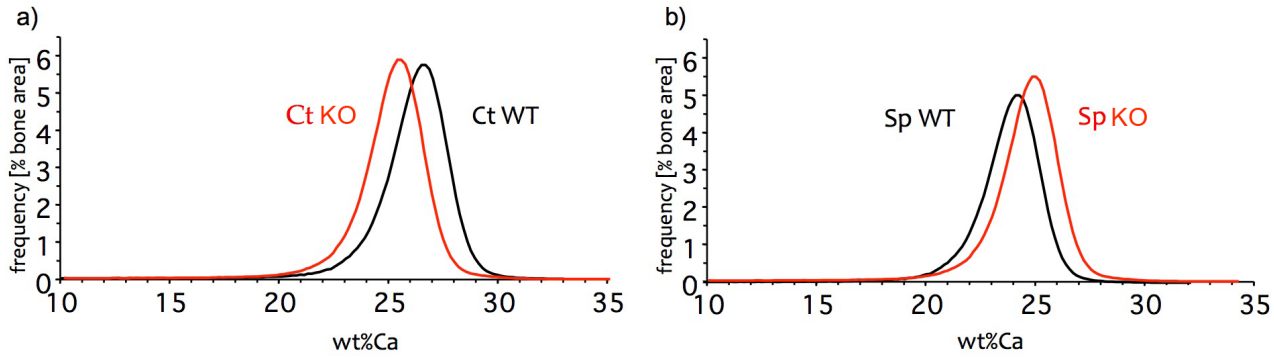

Figure 4.6: Bone mineralization density distributions (BMDD) of the cortical bone (Ct) and the spongiosa (Sp) of *SostKO* (-/-) and wild-type (WT) mice. In *SostKO* mice, in the cortical bone the distribution is shifted towards lower mineralization (a) while in the spongiosa the opposite is the case (b).

Table 4.2: Comparison of bone mineralization density distribution (BMDD) parameters between wild-type (WT) and *SostKO* mice: Ca_{Mean} and Ca_{Peak} characterize the degree of mineralization in cortical bone (Ct) and metaphyseal spongiosa (Sp). Ca_{Width} reflects the heterogeneity mineralization. The quoted numbers refer to mean values and standard deviation. $^{*}p < 0.05$, $^{**}p < 0.005$, $^{***}p < 0.001$

	Ct			Sp		
	WT ($n = 11$)	*SostKO* ($n = 9$)	Diff. %	WT ($n = 11$)	*SostKO* ($n = 9$)	Diff. %
Ca_{Mean}	25.63	25.14*	1.90	22.65	23.86***	5.30
$[wt\%Ca]$	0.44	0.45		0.55	0.38	
Ca_{Peak}	26.14	25.61*	2.00	24.04	24.63**	2.50
$[wt\%Ca]$	0.42	0.46		0.42	0.36	
Ca_{Width}	2.95	3	1.70	3.59	3.12**	13.10
$[wt\%Ca]$	0.23	0.15		0.34	0.21	

4.2.2 Mineralization kinetics and organic matrix properties of *SostKO* mice

In the recently published study, femoral diaphysis cross sections of *SostKO* ($n = 9$) and wild-type mice ($n = 10$) (described in Chapter 3.2) were investigated using the DSM962 microscope (Chapter 2.2.1) and Raman micro-spectroscopy (Chapter 2.2.3) [18]. Recording and evaluation of the Raman spectra were performed by colleagues in our institute supervised by Elephterios Paschalis, PhD. In this study a routine to combine the fluorochrome labeling technique and qBEI was developed (Chapter 3.4). This was done to gain information on the mineralization kinetics at the periosteal and the endocortical site of the femoral diaphysis. Additional, Raman measurement points were set between the fluorescent labels to reveal parameters like the *proteoglycan/matrix* ratio, the *mineral − maturity/crystallinity* of the bone mineral apatite crystallites (see Chapter 2.2.3). Tissue age normalized qBEI and Raman measurements were executed as shown in Figure 4.7. Unfortunately, this kind of analysis could not be performed at the cancellous regions in longitudinal sections according to rare trabecular structure in the wild-type group.

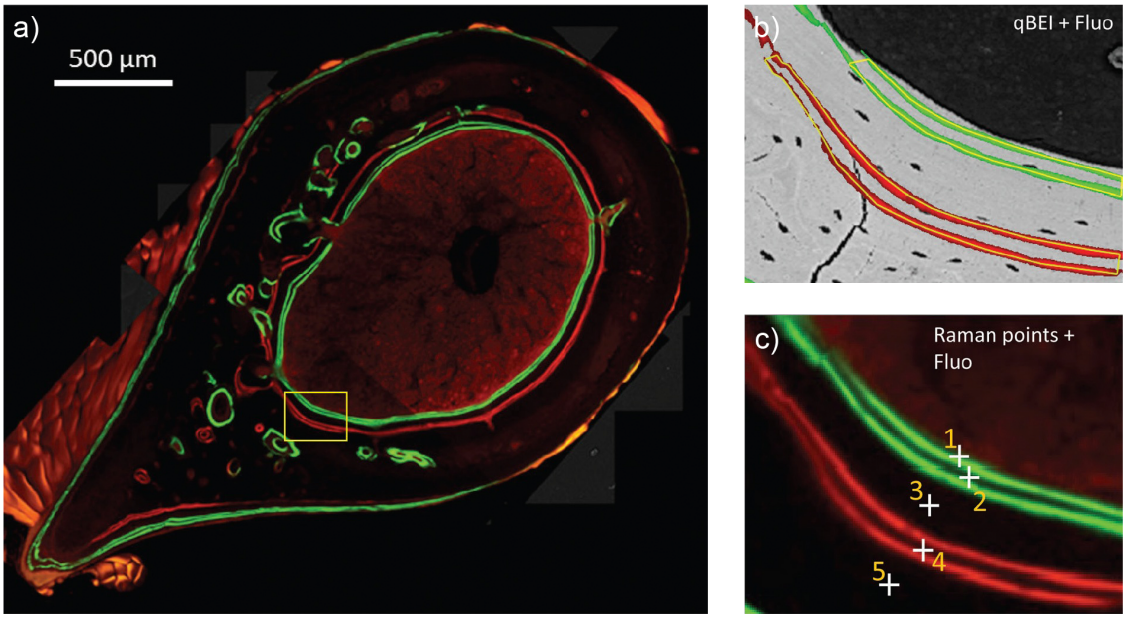

Figure 4.7: (A) Stitched fluorescent image from the confocal laser scanning microscope (CLSM) of transversal section of a *SostKO* mouse femur. Calcein double-labels (green) mark the young tissue (tissue age 5 to 15 days), Alizarin labels (red) mark the older tissue (tissue age 55 to 65 days). (B) Using reflection images obtained by CLSM, tissue age information (fluorescent labels) are overlaid on the qBEI image. The yellow-framed areas were considered for the analysis of mineralization at defined tissue ages. (C) Raman measurements were performed at five different tissue ages. The crosses mark the position of the measurement points. Marks #2 and #4 correspond to the regions considered for qBEI analysis.

It should be mentioned that in the scope of this study also samples from humans lacking

sclerostin (suffering Sclerosteosis) were analyzed with qBEI and Raman spectroscopy. Due to the rarity of this disease the sample number was low, thus limiting expressiveness. The corresponding results can be found in [18].

Quantitative backscattered electron imaging (qBEI)
2-way ANOVA revealed no interaction between genotype and tissue age (Table 4.3). At endocortical bone envelope the degree of mineralization in *SostKO* mice was significantly changed compared to wild-type mice at both tissue ages (Figure 4.8). Between calcein labels (5 15 day-old tissue) a decrease of the mineral content (1 9%, $p < 0\ 0001$) was found, as was the case within the alizarin double label (55 65 day-old tissue) (1 5%, $p < 0\ 05$).
No significant differences in mineralization were observed at the subperiosteal bone envelope between *SostKO* and wild-type animals (Table 4.3). Within genotype, the differences in mineralization ($wt\%Ca$) between the young and old tissue ages were significant at the endocortical (WT: +4 6%, $p < 0\ 0001$, KO : +5 6%, $p < 0\ 0001$)) and the periosteal (WT: +5 7%, $p < 0\ 0001$, KO : +4 8, $p < 0\ 0001$) sites (Figure 4.8).

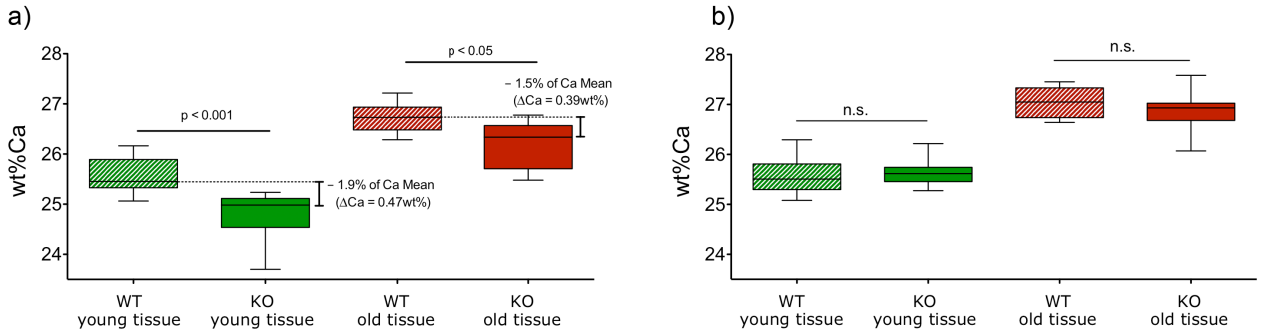

Figure 4.8: Degree of mineralization (wt%Ca) in *SostKO* and wild-type mice: (a) Regions of young tissue age (5 to 15 days) as well as older regions (55 to 65 days) exhibit significantly lower mineralization (1 9 % [0 47 $wt\%Ca$] and 1 5 % [0 39 $wt\%Ca$], respectively) at the site of endocortical bone apposition. (b) At the site of periosteal bone apposition no changes in mineralization were observed between *SostKO* and wild-type mice, when comparing the same tissue age. Consistently, older tissue is significantly higher mineralized than younger tissue in both genotypes (significance levels not indicated). 2-way ANOVA revealed no interaction between genotype and tissue age for both anatomical sites.

Raman measurements
2-way ANOVA analysis indicated that all monitored parameters depend on tissue age (Table 4.3) at both the endocortical and periosteal surfaces. On the other hand, *Sost* deletion affected these parameters only at endocortical surfaces. Specifically, the Proteoglycan content normalized to the amount of organic matrix was significantly higher in the *SostKO* animals at tissue ages 2 5 days, while the *mineral-maturity/crystallinity* values at endocortical surfaces were also dependent on genotype (per 2-way ANOVA analysis); subsequent individual unpaired t-tests between groups at each specific tissue age did not reveal any significant difference ($p > 0\ 05$).

Table 4.3: Results of 2-way repeated measurements ANOVA analysis of the quantitative backscattered electron analysis (qBEI) and Raman parameters. Significant values are bold.

	tissue age effect		genotype effect		interaction	
	end	peri	end	peri	end	peri
wt%Ca	**< 0.0001**	**< 0.0001**	**< 0.0001**	0.690	0.400	0.256
proteoglycan/matrix	**<0.0001**	**0.002**	**<0.0001**	0.214	0.132	0.689
min.maturity/crystallinity	**0.001**	**<0.0001**	**0.024**	0.574	0.295	0.139

4.2.3 Effect of Sclerostin Antibody Treatment (SclAB) in a Mouse Model of Severe Osteogenesis Imperfecta

After the characterization of bone mineralization and organic matrix properties of mice lacking sclerostin as presented above, the logical follow-up task is to describe the mineralization pattern of a mouse model treated with SclAB. Fortunately, we were able examine this in growing and adult wild-type mice and in a newly established mouse model of severe Osteogenesis Imperfecta as described in Chapter 3.2. This study is already published in Bone [21].

Longitudinal sections of the distal femur were analyzed using qBEI (DSM962). Additionally, blood serum data, mechanical properties and histological parameters were obtained, which are not presented, but are described in detail in the related publication [21]. Bone samples from growing (8-weeks-old) and adult (24-weeks-old) wild-type mice were analyzed with and without injection of SclAB (for more details see Chapter 3.2.

We found that in all analyzed anatomical sites (metaphyseal spongiosa (MS), epiphyseal spongiosa (ES) and cortical bone at the diaphysis (Ct)) BMDD exhibited a clear shift towards higher mineralization in the OI mice compared to the wild-type mice (see Figure 4.9). However, the impact of SclAB treatment on the BMDD was different with respect to skeletal sites, genotype and animal age. Further, there was a general increase in bone matrix mineralization from MS to ES to Ct and between 8 to 24-weeks-old mice (Figure 4.10 and 4.11). The BMDD parameters Ca_{Mean}, Ca_{Peak} , Ca_{Width}, Ca_{Low} and Ca_{High} were used to quantify statistically these differences in the BMDDs of the animal groups as introduced in Chapter [14].

The quoted p-values refer to 2-way ANOVA tests for factor genotype and factor treatment. No interaction terms were observed with exception of Ca_{Width} in the ES of the 8-weeks-old mice and Ca_{Low} of the Ct of 24-weeks-old mice. The written ranges of % changes in BMDD parameters correspond to the results of the post-hoc tests between the individual experimental groups displayed in Figure 4.10 and 4.11.

8-weeks-old mice (Figure 4.10)
Considering factor genotype, qBEI of the distal femur of 8-weeks-old mice showed higher matrix mineralization in OI. The most frequently occurring *Ca*-content were consistently increased at all three measured sites in OI mice compared to wild-type mice (Ca_{Peak} +5.2 to

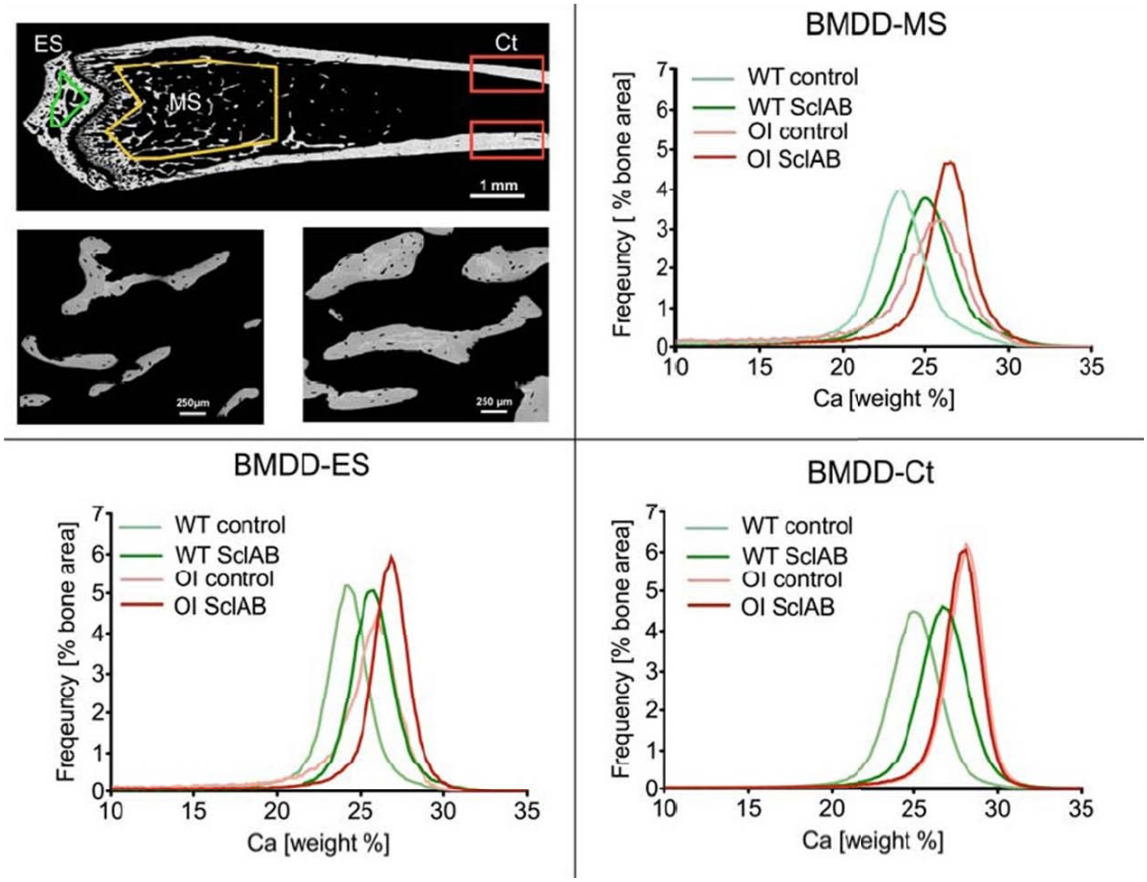

Figure 4.9: Backscattered electron image of the distal femur (longitudinal section) of 8-weeks-old mice: Untreated wild-types (upper panel) showing the three regions of interest in which BMDD analysis was performed: MS, cancellous metaphyseal bone; ES, cancellous epiphyseal bone; Ct, cortical midshaft bone. Metaphyseal cancellous bone of untreated (lower left panel) vs. treated (lower right panel) wild-types. Examples of BMDD histograms: Analysis at the three skeletal sites of the four experimental groups.

+8 3 %, $p < 0\ 0001$). The weighted mean Ca-content was increased in the cortical region (Ct) (Ca_{Mean} +6 7 to +7 0 % $p < 0\ 0001$). The heterogeneity of mineralization was decreased in OI compared to wild-type exclusively in the Ct (Ca_{Width} 20 0 to 22 5 %, $p < 0\ 0001$). The low mineralized portion of bone was increased in the MS and ES of OI mice (Ca_{Low} +45 2 to +106 5 %, $p < 0\ 0001$) while there was no difference in the Ct. The high mineralized portion exhibited elevated levels in the ES and Ct of OI (Ca_{High} +113 to +360 %, $p < 0\ 0001$).

Considering the factor "treatment", SclAB administration led to a shift towards higher mineralization in the cancellous bone regions compared to non-treated mice. Ca_{Mean} was increased in MS and ES (+2 9 to +4 1 %, $p < 0\ 05$). This was accompanied by a decrease of Ca_{Width} (0 7 to 17 4 %, $p < 0\ 05$) and a reduction of Ca_{Low} (19 7 to 34 8 %, $p < 0\ 005$) in these regions. Ca_{High} significantly increased in the MS (+31 6 to +49 0 %, $p < 0\ 05$), while at the other sites the same trend was present.

24-weeks-old mice (Figure 4.11)
In contrast to growing mice, treatment with SclAB of old animals did not change any BMDD parameters. Nevertheless, OI mice also exhibit a pronounced phenotype: Ca_{Peak} was increased at all sites (+2.8 to +6.1 %, $p < 0.0001$). Consistently, Ca_{Mean} was increased in the MS and the Ct (+1.7 to +5.4 %, $p < 0.05$). Ca_{Width} was reduced in OI at MS and Ct (−4.3 to −25.2 %, $p < 0.05$). Ca_{Low} (+4 to +111 %) and Ca_{High} (+34.1 to +360 %) were significantly elevated at all sites in OI. With exception of Ca_{Low} in the Ct where 2-way ANOVA revealed no significant difference, while post hoc test indicate a reduction. 2-way ANOVA revealed no interaction terms between the factors "genotype" and "tissue age".

Gain of bone mass
Regarding the increase of femoral bone mass (BV/TV and cortical thickness) as measured by μCT (performed by collaborators at the Shriners Hospital for Children, Montreal, Canada), it should be noted that there was a distinct response to SclAB treatment in growing and adult wild-type and OI animals. As expected within the same treatment and age group OI mice exhibited lower BV/TV and cortical thickness.

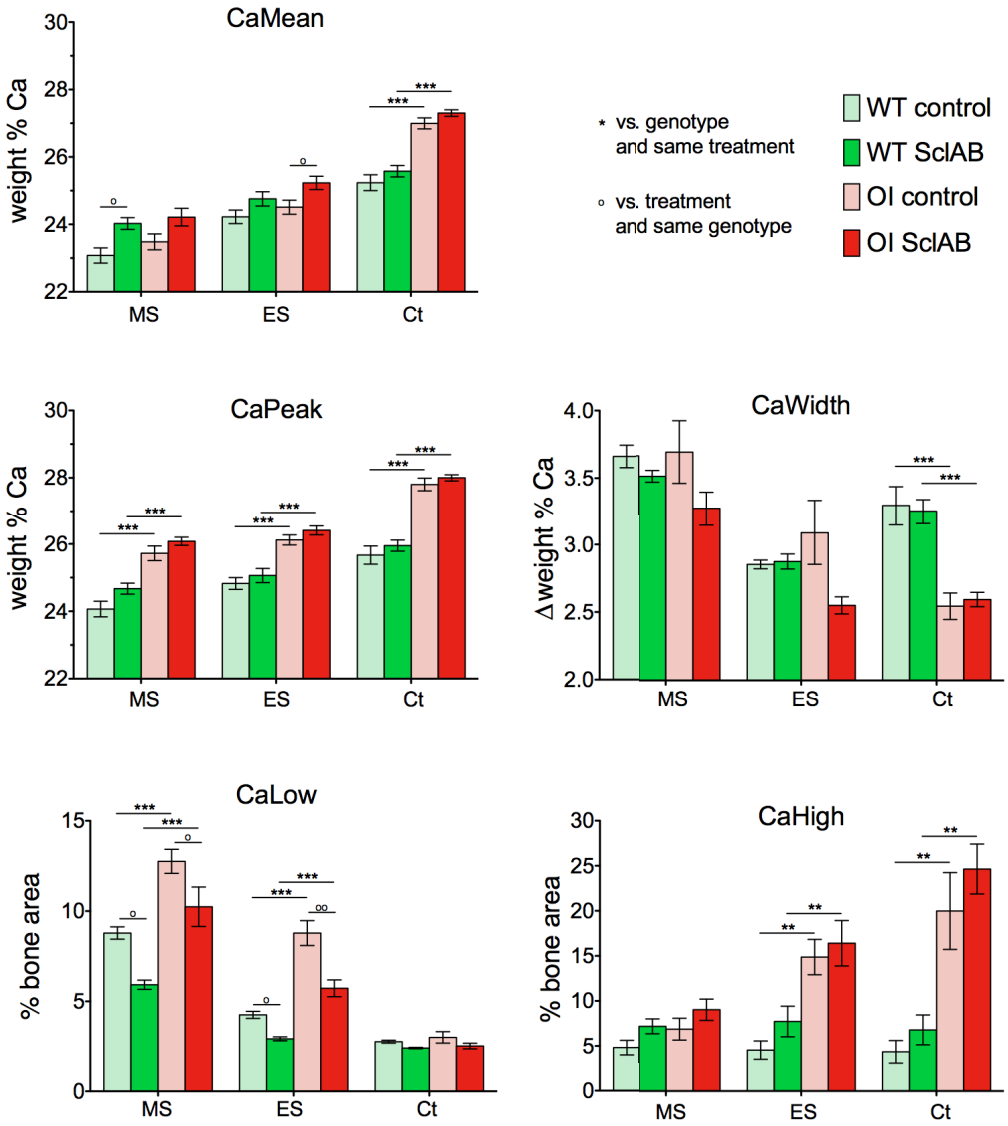

Figure 4.10: Results of qBEI analysis at the distal femur in 8-weeks-old mice of the metaphyseal spongiosa (MS), epiphyseal spongiosa (ES) and cortical bone (Ct): n = 8 mice per group. $^{***}p < 0.0001$, $^{**}p < 0.005$, $^{*}p < 0.05$ vs. genotype and same treatment; $^{°°°}p < 0.0001$, $^{°°}p < 0.005$, $^{°}p < 0.05$ vs. treatment and same genotype using Bonferroni post-hoc test.

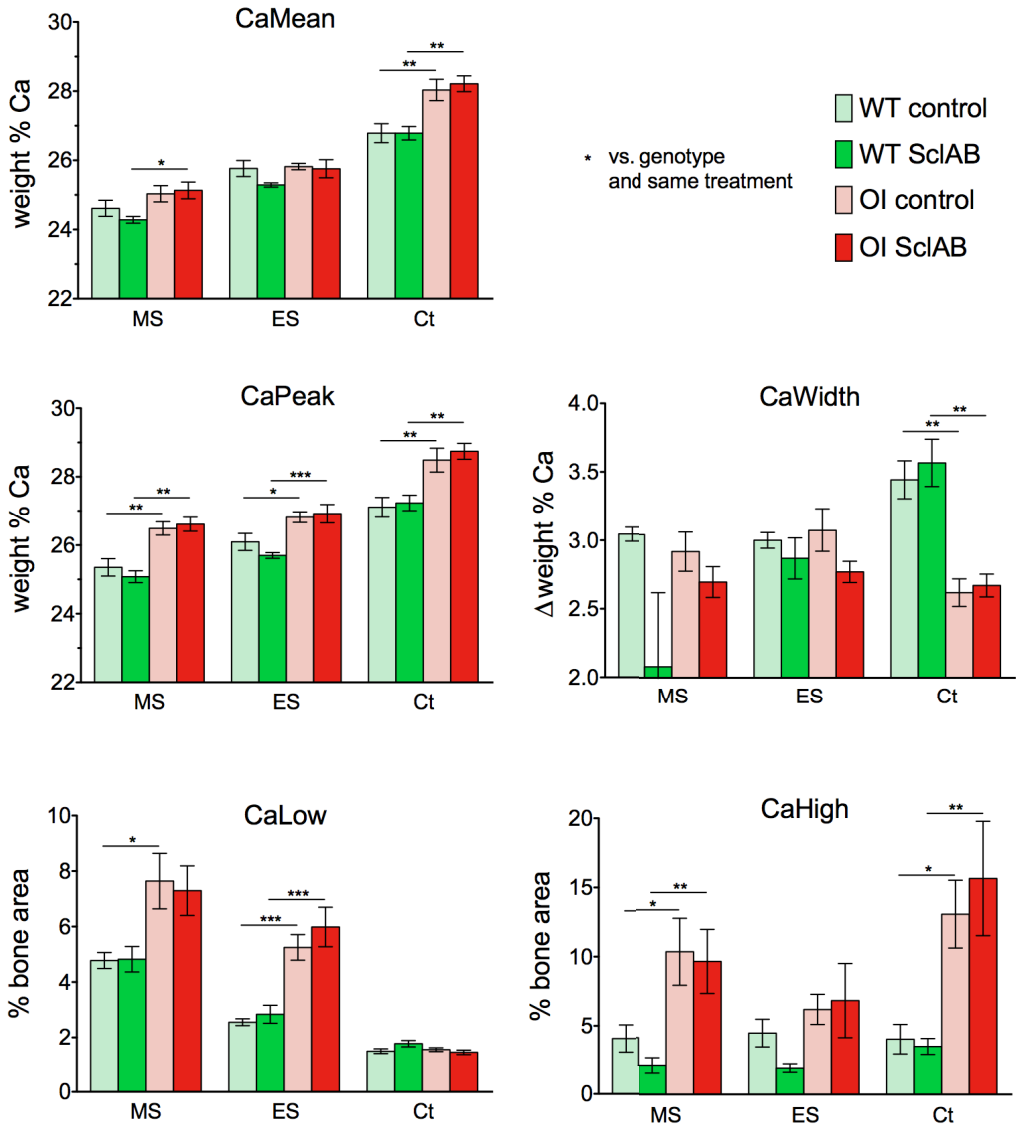

Figure 4.11: Results of qBEI analysis at the distal femur in 24-weeks-old mice of the metaphyseal spongiosa (MS), epiphyseal spongiosa (ES) and cortical (Ct): n = 8 mice per group. $^{***}p < 0\ 0001$, $^{**}p < 0\ 005$, $^{*}p < 0\ 05$ vs. genotype and same treatment; using Bonferroni post-hoc test.

4.2.4 Discussion

As already several studies associated reduced sclerostin activity with increased bone formation, within our studies and the presented projects we focused on the material science level to reveal possible changes in bone tissue composition. This aim is also of special clinical interest as the administration of SclAB is one of the most promising approaches for future Osteoporosis treatment.

BMDD of *SostKO* mice
When analyzing *SostKO* mice, routinely performed methods needed to be extended and combined with CLSM to gain information on the mineralization kinetics at endocortical and periosteal sites of bone apposition. BMDD analysis of longitudinal sections of *SostKO* mice revealed a differential effect of sclerostin deficiency between cancellous and cortical bone regions. The shift of BMDD towards higher mineralization in the cancellous region is supposed to be (at least partly) due to geometrical effects. As the femur metaphysis of the control mice (adult - 16-weeks-old) contains only few small trabeculae, the average tissue age is likely very low according to ongoing bone turnover. As mineralization needs some time to reach its plateau [14, 144, 145, 146] , the lower average tissue age causes an overall low mineral content. Without assuming any changes in the kinetics of mineralization, an overall elevation in mineralization is expected when the trabecular diameter increases and thus also the average tissue age. With increasing distance from the surface, bone regions are more likely to be protected from being remodeled and thus elevating the average time available for mineralization. Taking these considerations into account no statements can be made regarding the mineralization kinetics in these regions.

We assumed that according to the different geometry of the cortical bone this effect might be present to a much lower quantity. Nevertheless, the shift of the BMDD in this region towards lower mineralization appeared contradictious. As we had the feeling that this effect cannot be explained by the increase of newly formed bone matrix alone, change of the mineralization kinetics was hypothesised causing potentially lower mineralization at similar tissue age.

Mineralization kinetics of *SostKO* mice
This hypothesis was tested using a combination of CLSM and qBEI. The presented results revealed lower mineralization in the *SostKO* mice compared to wild-type at the same tissue age confirming our hypothesis made above. This result leads to the conclusion that there must be a change in mineralization kinetics in the very early stage of bone matrix mineralization. Interestingly, this effect was only present at the site of endocortical bone apposition while at the periosteal site, there were no significant differences observed. This is in line with the literature characterizing the corresponding human disease (Sclerosteosis) by an increase of endosteal osteolysis [20]. On the other hand Li et al. showed that *SostKO* mice exhibit a decreased endocortical but also an increased periosteal perimeter indicating that the lack of sclerostin effects both anatomical sites [77].

Proteoglycans in *SostKO* mice
Consistent with the changes in mineralization kinetics exclusively at the endocortical side,

Raman measurements revealed changes in the organic matrix at this side but not at the side of periosteal bone formation. Most interesting, the $PG/matrix$ peak area ratio was significantly increased in the $SostKO$ mice. PGs are reported to act as inhibitors for mineralization [45, 44]. Furthermore, it is known that PGs are enriched at border regions of the canaliculi [45] to prevent the void from mineralization. In this context it can be speculated that the significant increase in $PG/matrix$ might reflect alterations in the osteocyte canaliculi network.

A new approach for further analysis *SostKO* mice
Based on these results regarding the differential mineralization kinetics and PG content, possible working hypothesis for future investigations might be:

1. The lower mineralization and the increase in the $PG/matrix$ at defined tissue ages in the $SostKO$ mice are due to an increased microporosity, caused by a denser OLCN compared to wild-type.

2. The lower mineralization and the increase in the $PG/matrix$ at defined tissue ages in the $SostKO$ mice are due to an increased microporosity, caused by an elevation in the average canalicular diameter.

Hypothesis 1 can be tested using CLSM after Rhodamine staining as introduced in Chapter 3.6 with fluorochrome-defined tissue age as described in Chapters 3.4 and 4.2.2. This approach would allow characterization the of OLCN with respect to a specific tissue age. For the image acquisition of a sample stained with Rhodamine and labeled with Alizarin and Calcein it might be challenging to find measurement parameters to separate the three fluorescence signals. Figure 4.12 shows the results of a feasible study where a cortical region of a $SostKO$ mouse was imaged, visualizing the OLCN and the two double labels. With the evaluation of the OLCN with respect to the fluorochrome labels we assume to be able to test if there are structural differences in the OLCN in $SostKO$ compared to wild-type mice.

Regarding hypothesis 2, unfortunately the resolution of conventional CLSM is not appropriate to detect changes in the canaliculi diameter, making a verification of the hypothesis impossible with this technique. For the evaluation of canaliculi diameters other methods like synchrotron phase-contrast-tomography and focused ion beam (FIB) sputtering technique combined with SEM imaging appear more suitable, but also less accessible and more time consuming [147, 22]. Furthermore, to the best of our knowledge these methods are not established to measure at regions of defined tissue age until now.

Periosteal vs. endocortical regions in *SostKO* mice
Beside these hypotheses, the question lingers why changes in the mineralization kinetics and the $PG/matrix$ ratio were observed exclusively at the endocortical site. We speculate that decreased mineralization arises from a local Ca and/or PO_4 deficit due to the extensive rate of bone formation. Hence, it might be the case that the ion-supply at the less accessible endocortical site (where also the cancellous ossification is strongly raised) becomes insufficient causing a local mineral deficit. As the periosteal site of bone formation is closer connected to the metabolism, local Ca and/or PO_4 consumption might play a minor role. As discussed in Chapter 2.1.3 the early mineralization process is still poorly understood, but there is general

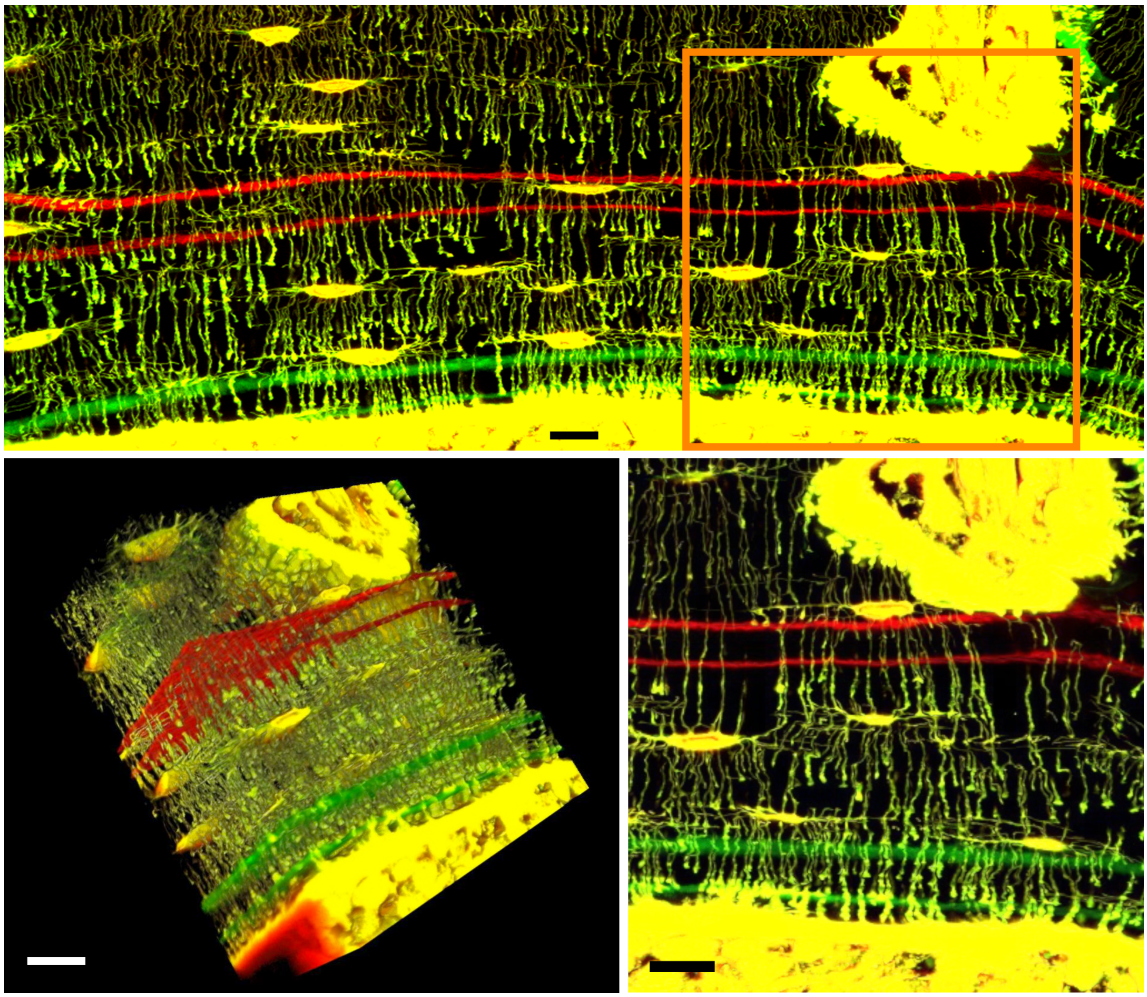

Figure 4.12: Result of a feasibility study with the goal to image the osteocyte lacuna canaliculi network (OLCN) together with fluorescent labels marking a specific tissue age (red: Alizarin, green: Calcein), using a confocal laser scanning microscope (CLSM). error bar: 10 μm

agreement that it is a critical and high controlled process. Thus it is reasonable that changes in the ion supply at the very early mineralization stage would have a significant impact on the properties of the matured bone matrix.

Periosteal vs. endocortical regions in *SostKO* mice

As the role of sclerostin in WNT signaling [11] is well documented and an increase in bone mass in *SostKO* mice is consistently reported in several studies, the question appears if the administration of SclAB has a similar effect on (i) treated and untreated wild-type mice and on (ii) mice suffering a severe bone disease. Hence, our study was designed to investigate changes in bone mass, mineralization, and plenty other parameters linked to bone fragility in wild-types and in a cohort of mice being a model for severe Osteogenesis Imperfecta.

Osteogenesis Imperfecta (OI) is a bone fragility disorder linked to a collage mutations causing

fragile bone tissue with an increased susceptibility for fracture. Up to now there are more than 1500 mutations known causing OI with phenotypes of highly variable severity (from mild to prenatal lethality) [11]. Usually OI patients and corresponding animal models exhibit low bone mass accompanied with increased bone matrix mineralization [148]. The present mouse model fits this pattern. The increased mineralization is indicated by a shift of BMDD towards higher mineral content. Thus Ca_{Peak} and Ca_{High} are consistently elevated in 8 and 24-weeks-old OI mice compared to wild-types at all investigated anatomical sites. The decrease of Ca_{Width} in the cortical bone of both age groups indicates a reduced heterogeneity in the mineralization pattern, which is also typical for OI [148].

4 weeks of treatment with SclAB had almost no effect on the mineralization pattern of the adult mice wild-type and OI mice. The effects observed for Ca_{Mean} (slightly increased) and Ca_{Low} (decreased) in the cancellous bone of growing mice cannot clearly be allocated to geometrical effects as discussed above or to possible changes in the mineralization process. Since 2-way ANOVA revealed no interaction terms between the factors "genotype" and "tissue age" for any age group or anatomical site, we conclude that SclAB treatment has a similar effect on mineralization in the analyzed OI and wild-type mice. This statement includes that the pathological collagen structure which likely leads to the hypermineralization in the OI mice remains the same for bone formed during SclAB treatment. Hence, it can be speculated that SclAB treatment of OI patients will not heal OI in terms of causing the synthesis of physiological bone matrix. But nevertheless, it is plausible that a higher amount of bone consisting of pathologically modified collagen matrix still improves the resistance to fractures.

4.3 Bone Mineral Properties with Respect to the Osteocyte Lacunae Canaliculi Network (OLCN)

4.3.1 Classification of the ROIs with respect to the OLCN

In Chapter 3.6 a method was introduced to stain the OLCN with Rhodamine, which is compatible with the standard embedding procedure as described in Chapter 3.1. This approach offers the possibility to gain information on the OLCN and the bone matrix composition of region of interests (ROIs) using EDX. These methodical developments were performed in the frame of this thesis and allow addressing the following question:

- Assuming that regions in human cortical bone can be classified with respect to the OLCN, how does the composition of the mineralized bone matrix depend on the canaliculi network type just below the sample surface of a sectioned area?

Femur cross sections from eight humans without reported bone or bone-related diseases were used for this study as described in Chapter 3.2. Figure 4.13 shows an overview fluorescence image of the OCLN of the lateral part of a human (adult) femur midshaft cross section. Studying such images we found 4 characteristic types of features, facilitating the classification of ROIs. As labeled in Figure 4.14, the following types of ROIs were taken into consideration:

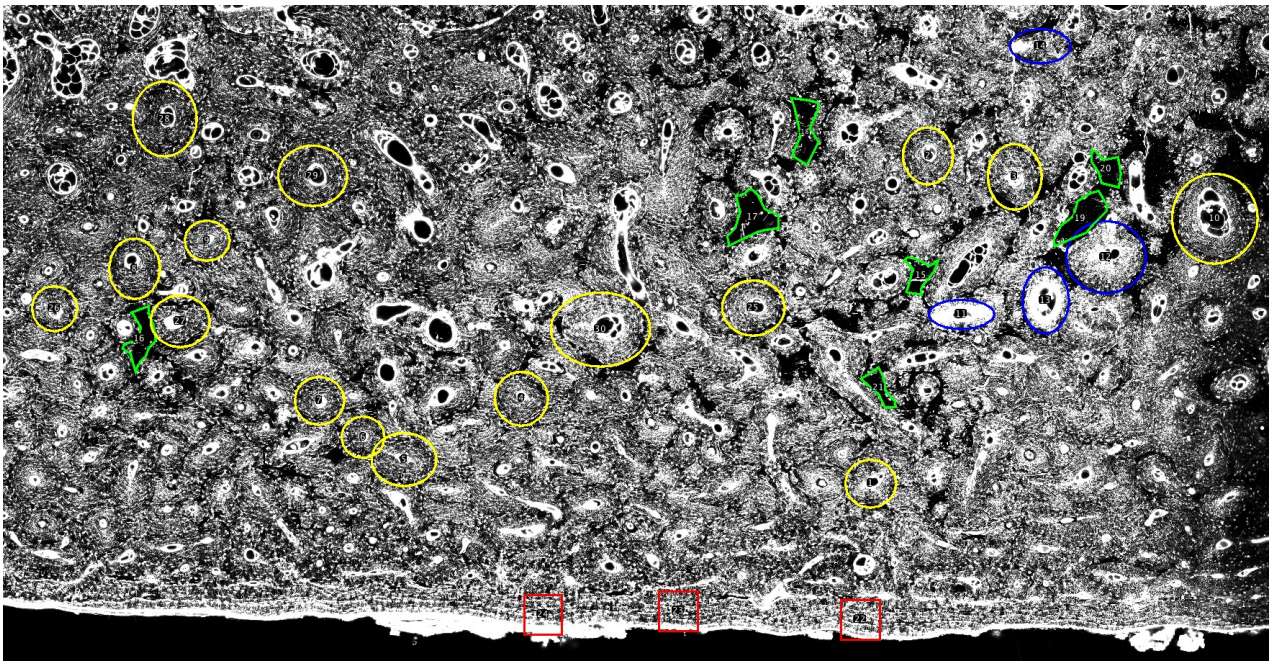

Figure 4.13: Overview fluorescent (Rhodamine) image stitched from single images taken at the confocal laser scanning microscope (CLSM): The labels mark various regions, which were considered for further evaluation. (yellow: nicely stained osteons, green: not stained regions, blue: regions with outstanding bright Rhodamine fluorescence, red: periosteal sites with parallel network)

1. Almost circular osteons with a well stained network (homogenously stained OLCN and separable canaliculi)

2. Regions exhibiting no fluorescence, appearing as black areas in Figure 4.13

3. Osteons exhibiting an outstanding bright fluorescence signal

4. Regions with a highly parallel network with an orientation perpendicular to the periosteal bone surface

ROIs classified due to these features were taken into consideration at the lateral sites of all eight femur cross sections. Table 4.4 gives an overview over the number of evaluated ROIs for each sample.

4.3.2 Measurement Procedure

For each ROI a depth scan was performed using CLSM with a standardized protocol as described in Chapter 3.6. In this way 3D information on the network structure was gained, which was not further analyzed within this project.

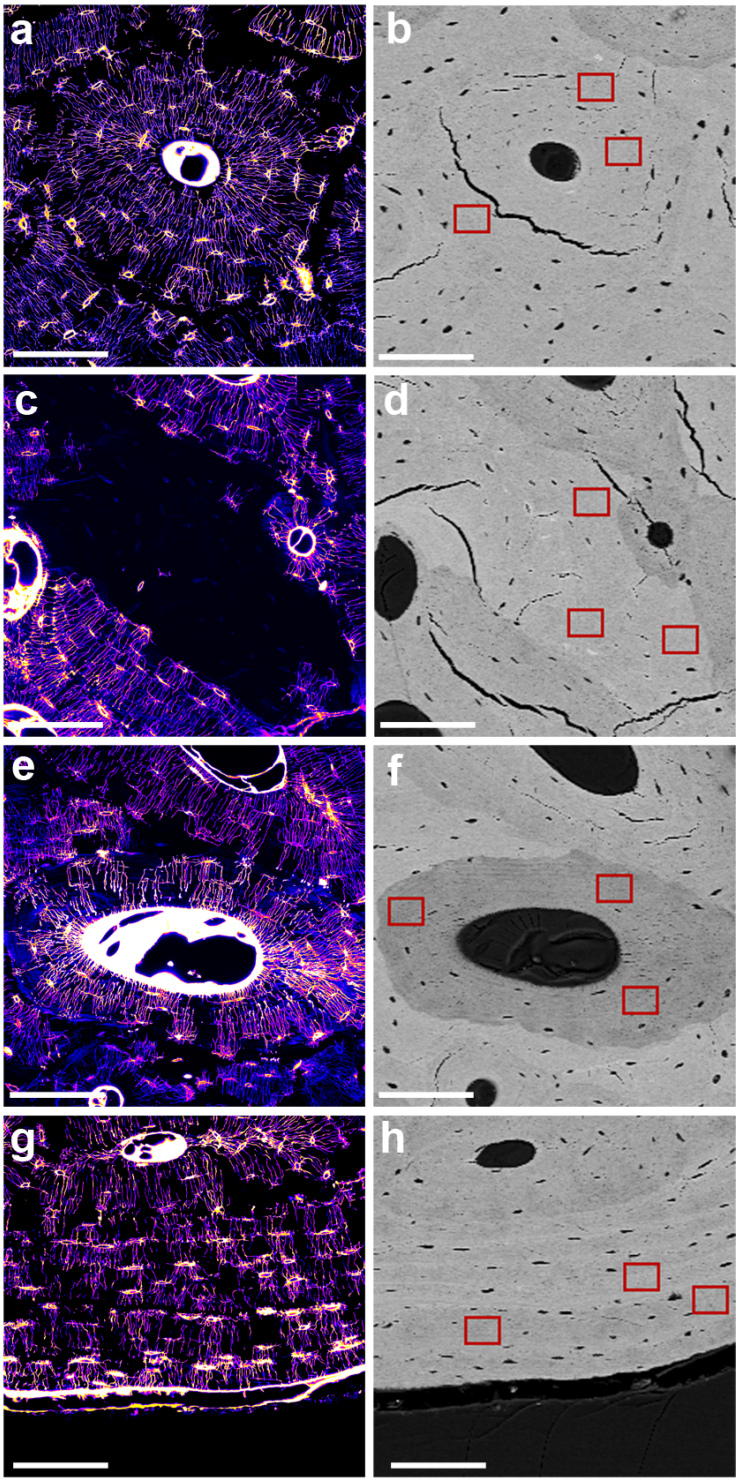

Figure 4.14: Fluorescent (Rhodamine) images and corresponding backscattered electron images of the four different regions of interest (ROI):
(a,b) Type 1: nicely stained osteons,
(c,d) Type 2: unstained regions,
(e,f) Type 3: regions with outstanding bright Rhodamine fluorescence,
(g,h) Type 4: periosteal sites with parallel network);
The red rectangles mark regions which were eventually considered for energy dispersive X-ray (EDX) analysis ($39.1 \times 29.3\ \mu m^2$).
scale bars: 100 μm

Table 4.4: Overview over the samples used in this project and the numbers of the measured regions of interest (ROI): For Each ROI an image stack of about 200 images was obtained (z-scan) with the confocal laser scanning microscope (CLSM). Three measurement fields per ROI were selected for energy dispersive X-ray analysis (EDX).

sample	age	sex	ROI Type 1 stained OLCN	ROI Type 2 unstained ROIs	ROI Type 3 heavily stained ROIs	ROI Type 4 ROIs exhibiting parallel network
FM04C	50J	f	15	10	6	4
FM38	55J	f	10	8	2	3
FM40	56J	f	10	8	5	0
FM48	48J	f	16	8	3	3
FM15	1.5J	m	7	0	10	8
FM21	2.5J	f	9	7	7	4
FM25	1.5J	f	1	0	8	4
FM28	16m	f	6	0	7	4
		total:	74	41	48	22

Subsequently, the samples were carbon coated (SEM Carbon Coater 108C, Agar Scientific, Essex, UK) and the ROIs were revisited with a field emission electron microscope (FESEM, Supra40, Zeiss, Oberkochen) for qBEI measurements using parameters as described in Chapter 3.3. This was done prior to EDX analysis. As indicated in Figure 4.14 in every ROI three EDX measurement fields were located ($39.1 \times 29.3\ \mu m^2$). Spectrum acquisition and the quantification of the elemental concentrations (Ca, P, S, N, Mg, K, Cl, O, C) were performed according to the protocol described in Chapter 3.5. Out of the three measurements per ROI the median value was used as entity for further statistical analysis. A typical EDX spectrum for bone is shown in Figure 4.15.

4.3.3 Results

Pooling the data from all samples, Figure 4.17a shows a linear correlation between the quantitative values for Ca and P ($R^2 = 0.97$, $P < 0.0001$). The Ca and P concentrations revealed to vary between 8.3 $at\%$ and 12.7 $at\%$, and 4.8 $at\%$ and 7.2 $at\%$ respectively. We found that the ROI classification, which was done with respect to the Rhodamine-related fluorescence signal of the OLCN, is reflected by different $at\%Ca$ and $at\%P$ values. Highly significant ($P < 0.0001$ - Mann Whitney test (non-parametric)) differences were found for $at\%Ca$ and $at\%P$ between nearly all classification types (Figure 4.16). No significant differences were only found between well-stained OLCN osteonal regions (ROI Type 1/yellow) and parallel orientated OLCN regions (ROI Type 4/blue) for both Ca and P. (Figure 4.16). Interestingly, a linear regression comparison analysis between these two ROIs (Type 1 vs. Type 4) revealed a similar slope ($p = 0.83$) but highly significant different intercepts of the regression lines with the y-axis ($p < 0.0001$) indicating elevated P levels for fixed Ca values.

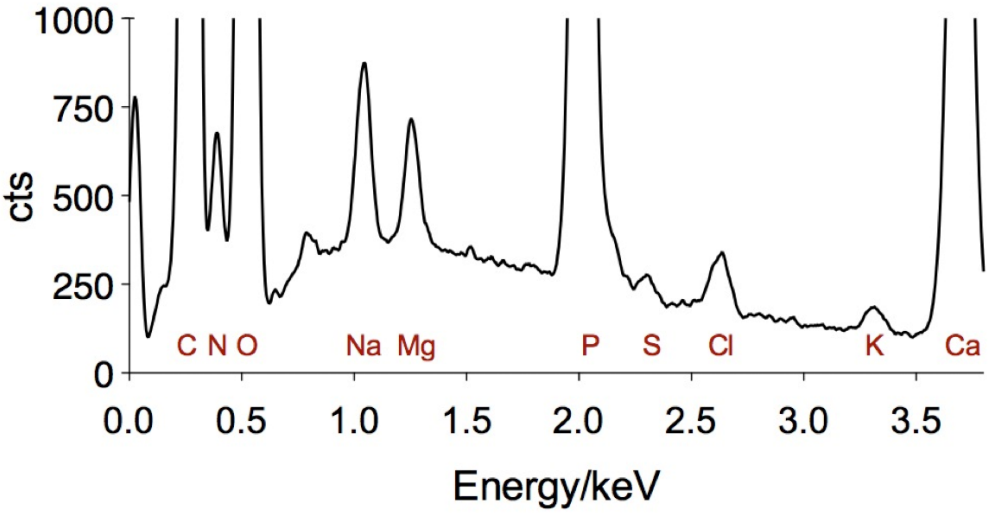

Figure 4.15: Typical spectrum of bone measured by energy dispersive X-ray analysis (EDX). Most of the peaks are separated so that peak intensities can be associated with the corresponding elements.

The Na concentration varied between 0 3 $at\%$ and 0 73 $at\%$. The overall slope of the linear regression line in the $at\%Na$ vs. $at\%Ca$ diagram was significantly different from zero ($p < 0\ 001$) as well as the slope for each single ROI Type (at least $p < 0\ 05$). This indicates a positive correlation between Na and Ca concentrations (Figure 4.17d).

The Mg concentration plotted versus $at\%Ca$ exhibits no significant slope ($p = 0\ 58$) (Figure 4.17d). Similar to Na the Mg concentration in Type 1 ROIs compared to Type 4 ROIs indicate an increase at sites with parallel network at the periosteal site compared to osteonal, well stained tissue.

Quantification of the S concentration revealed values around 0 05 $at\%$, which is too close to the detection limit of EDX to perform any statistical analysis. Also the quantitative values should be treated with caution. The data suggest that there is no dependency or only a slight decrease of the S concentration with the mineralization (Figure 4.17c).

When comparing the individuals, one sample (#4 Table 3.1) revealed to exhibit a higher $at\%Ca$ $at\%P$ ratio compared to the others (1 73 vs. 1 66 $p < 0\ 0001$), potentially adulterating results for the pooled data set. Thus, all statistical tests were also performed when excluding sample #4 leading just to numerical changes in the results.

Separating the two age groups (women 48 56 a, $n = 4$) and children (16 m 2 5 a, $n = 4$) we found that the ROIs chosen in the bone samples of the children were in general lower mineralized compared to adults ($p < 0\ 0001$). As shown in Figure 4.18 the Ca P ratio is reduced in children. Even when focusing on the Ca-range between 10 5 and 11 5 $at\%$ (where both age groups exhibit a distinct number of data points), the Ca P values separate ($p < 0\ 0001$

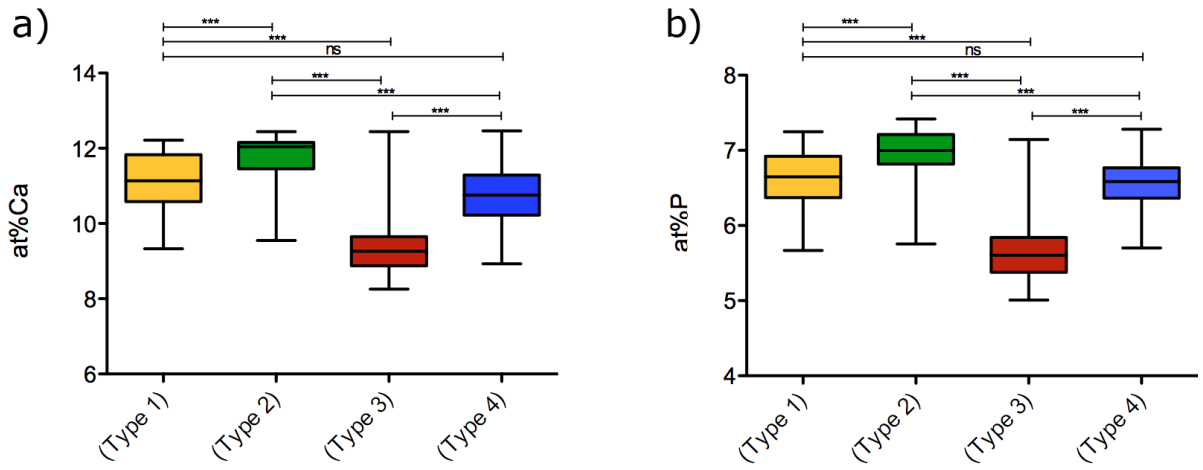

Figure 4.16: $at\%Ca$ (a) and $at\%P$ (b) content of the different types of regions of interest (ROI)
ROI Type 1: nicely stained osteons
ROI Type 2: unstained regions
ROI Type 3: regions with outstanding bright Rhodamine fluorescence
ROI Type 4: periosteal sites with parallel network
$***p < 0\ 0001$

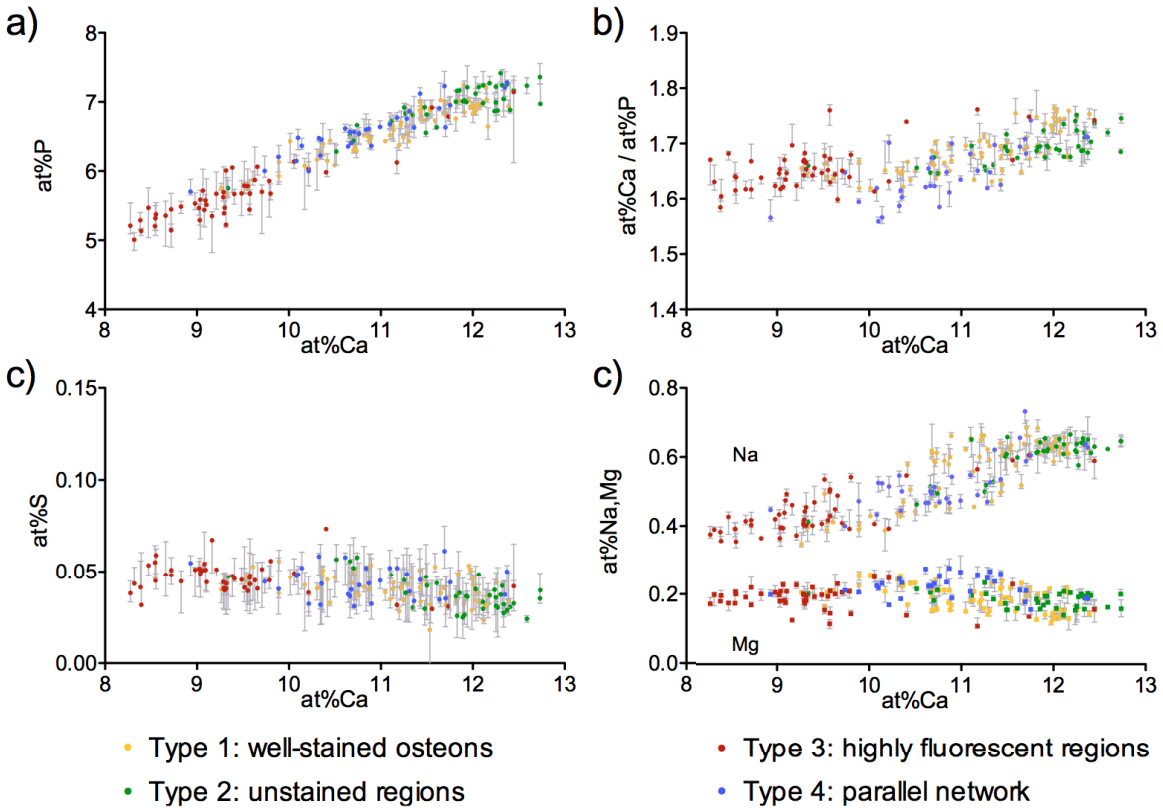

Figure 4.17: Elemental concentrations of P (a), S (c), Na (d) and Mg (d), and the Ca P ratio (b) vs. $at\%Ca$ being a parameter for the degree of mineralization measured by energy dispersive X-ray analysis (EDX): The dots are median values of the three measurements; the bars represent the range.

for pooled ROI types). Additionally, within this range also the Na concentration is distinctly reduced in children while the Mg content is elevated compared to the adult group ($p < 0\ 0001$ for pooled ROI types).

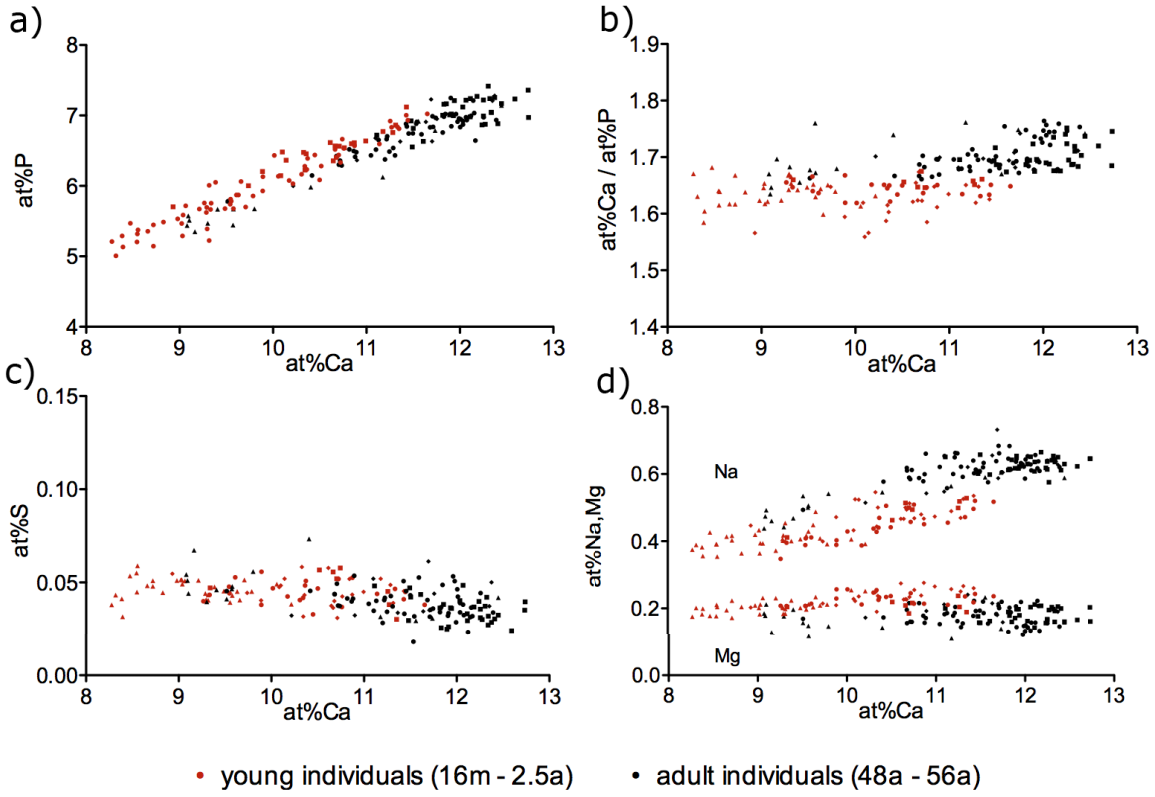

Figure 4.18: Median values of elemental concentrations of P (a), S (c), Na (d) and Mg (d), and the $Ca\ P$ ratio (b) vs. $at\%Ca$ being a parameter for the degree of mineralization measured by energy dispersive X-ray analysis (EDX): Significant differences are observed when comparing data points (P, $Ca\ P$, Na, Mg) of young and adult humans, even when restricting the $at\%Ca$ range to 10 5 11 5 $at\%$.

4.3.4 Discussion

The presented study was designed to investigate the correlation between the OLCN and bone composition of human femoral midshaft cross-sections. This approach targets indirectly the ongoing discussion about osteocytic osteolysis where an interaction between osteocytes and adjacent mineralized bone matrix is suggested. Manifold publications focus on the evaluation of the interaction between osteocytes and their proximate environment indicating that there are well-controlled mechanisms allowing the osteocytes to influence adjacent regions of the lacunae or those close to canaliculi [22, 84, 83, 4]. Recently it was shown, that the local bone density is distinctly increased close to the osteocyte lacunae wall. Similar, but less pronounced

observations were made close to the canaliculi [22].

The Ca/P Ratio

In this context the results of our study provide additional information. We were able to show, that for the investigated ROIs (very low mineralized regions at the mineralization fronts were excluded) $at\%Ca$ and $at\%P$ are highly linear correlated ($R^2 = 0.97$). The slope of the linear regression line reflects the $at\%Ca/at\%P$ ratio (Ca/P) which was determined to 1.672 which is close to the theoretical Ca/P value for pure HAP of 1.667. Hence, it can be concluded, that (i) the majority of Ca and P is bound to HAP while the quantities bound to the organic matrix like phosphorylated non-collagenous proteins seem to contribute only to minor quantities and that (ii) carbonatisation (CO_3 substitution of either Ca or PO_4) [115] or other elemental substitutions [40, 41, 42] do not affect the Ca/P ratio remarkably. Of course it cannot be excluded that (i) and (ii) appear to greater extent but cancel each other resulting in the observed Ca/P ratios. Nevertheless, in the literature, Ca/P values of bone are often reported to be close to 1.667 ($at\%$-ratio) or 2.222 ($wt\%ratio$) by using various techniques, confirming our results [138, 130, 137].

Based on these considerations the $at\%Ca$ value (or likewise $at\%P$) seems to be a reliable parameter to characterize the degree of mineralization. Therefore, in Figure 4.17 and Figure 4.18 the elemental concentrations are plotted against $at\%Ca$ to show the bone composition in the course of ongoing mineralization.

Mineralization in regions with different network types

Interestingly, we found significant differences in the degree of mineralization (defined as introduced above) between different ROI types. The distinctly lower mineralization of regions exhibiting an outstanding bright Rhodamine fluorescence is likely due to the increase in interfibrilar space which is not yet occupied by apatite crystals. We suppose that during the staining procedure (as described in Chapter 3.6) the ethanol - Rhodamine solution diffuses through the canalicular walls into the low mineralized matrix, and thus causing the outstanding bright and blurred signal.

In contrast to that, regions appearing dark in the fluorescent image (ROI Type 2) appeared to be the regions of highest mineralization. The majority of those ROIs were located in interstitial bone regions, encased by cement lines. Although no information is available about the 3D structure of these regions, it is obvious that the connection to the next blood vessel through the OLCN is worse compared to osteonal regions. Previous work documented that a cement line reflects a barrier for the majority of canaliculi, even if some of them manage to penetrate the cement line, thus building a bridge to the adjacent bone structural unit [149]. The lack of staining substance in the OLCN of these regions means that either (i) the connection to the next blood vessel/bone surface is to weak for the ethanol/Rhodamine solution to penetrate in noteworthy amounts or that (ii) according to the low nutrition supply the osteocytes died followed by partial ectopic mineralization of the remaining voids making a penetration of the staining fluid impossible. This would be in line with the observation, that qBEI images show an increased number of high mineralized osteocyte lacunae in these regions (no statistics performed, bright dots in Figure 4.14d). Previous work also focused on ectopically mineral-

ized osteocyte lacunae and showed their increased abundance in interstitial bone [150, 151]. Hence, it looks like these high mineralized regions, exhibiting a lack of staining, are rare of living osteocytes and thus of an intact OLCN. As a consequence, such regions would not (or at least less) contribute to mechanosensory, protein expression, ostoecytic osteloysis or other mechanisms, which are attributed to the osteocytes and their network. This should be taken into account when estimating the impact of the OLCN on bone as a biomaterial and/or an endocrine organ.

The finding that the degree of mineralization in well-stained osteons and periosteal regions is between those of the other ROI types, fits the considerations made above. Surprisingly, despite the fact that no difference in the Ca and P content of these two regions was observed, the Ca/P ratio revealed to be reduced at the periosteal sites exhibiting a parallel network. To the best of our knowledge this is not documented so far and might reflect differing mineralization mechanisms depending on the anatomical site. A detailed evaluation of mineralization fronts focusing on elemental concentrations with respect to the anatomical site is given in Chapter 4.4.

Concentrations of minor elements

There is only rare literature about the role of Na in bone metabolism or bone tissue. It is reported that bone might act as reservoir for Na (and also K) and may be remobilized if desired [139]. Interestingly, it was shown that low systemical Na levels (hyponatremia) lead to bone loss caused by increased osteoclastic activity [152]. The increase of Na concentration with ongoing mineralization as observed in our study cannot be explained so far. It remains unclear whether Na binds to the apatite crystals or is part of the organic matrix. However, the correlation with $wt\%Ca$ supports the first hypothesis.

In contrast, the role of Mg is documented in more detail. Mg is known to substitute Ca in the HAP [42, 153] and is known to occur as stabilizer of amorphous mineral phases as they might occur in early stages of mineralization [47]. Beside this, Mg is reported to be part of DNA-proteases, so it is probably also bound to organic matrix [154]. Hence, like for Na it remains unclear to which extent the observed Mg content is due to ions bound to mineral or to organic matrix. Since $at\%Mg$ revealed to be independent of the degree of mineralization reflected by $at\%Ca$, we suppose that the majority of Mg is bound to the organic matrix or incorporated in the HAP crystal during early mineralization without any further incorporation during crystal growth. However, from what we know from other elements (Pb, Sr) substituting for Ca in the HAP, such elements increase with the course of mineralization [155]. Hence, the reported Mg concentration might be due to Mg bound to organic components of the bone matrix. Interestingly, like the Ca/P ratio, also the Mg concentration exhibits differences between well-stained osteons (Type 1 ROI) and regions with parallel network at the periosteal site (Type 4 ROI). This encourages the statement made above, that there might be different mechanisms of bone formation depending on the anatomical site, which is also supported by measurements performed at mineralization fronts as discussed in Chapter 4.4.

S is reported to be present in so called sulfated Proteoglycans. Proteoglycans in general are reported to act as inhibitors of mineralization [44, 45]. They are abundant in cartilage tis-

sue but also (but to less extend) present in bone. Studies have shown that for example the Proteoglycan Perlecan is located mainly at the canaliculi walls [45]. Our study showed S concentations close to the detection limit of EDX. Hence, no reliable statistic can be performed. However, the data might suggest that the S concentration is either constant or slightly decreasing with ongoing mineralization.

The result that the Ca/P ratio as well as Mg and Na concentrations depend on the individual age (when comparing the same $at\%Ca$ range) is surprising. One might suspect that the course of bone formation and thus the involvement of minor elements is always the same. Despite the low sample number, for this cohort the separation for Ca/P, Mg and Na (at least between 10.5 and 11.5 $at\%Ca$) is quite convincing. Thus a systematically altered bone material composition depending on the individual age is most likely. The evaluation of potentially different concentrations of major and minor elements depending on the individual age features an exciting topic for future investigation and might lead to new insights into the role of these elements in bone and skeletal development.

Limitations
There are some limitations in this study, which should be taken into account when interpreting the data. We are aware that the total number of eight individuals (4 per age group) is quite low to make reliable general predictions. The study design was chosen to reveal basic mechanisms of bone mineralization, which are not supposed to vary a lot between different individuals. Nevertheless, interindividual differences in nutrition, age and genetic background are not known und thus might cause scattering of the measurement parameters. The selected samples originate from humans without documented bone diseases and were chosen with respect to a cause of death, which was not related to bone metabolism, but the exact health status of the persons is not known.

The EDX measurement fields used to gain the elemental information are useful as long as high spatial resolution is not necessary and as long as relatively homogenous mineralized regions are covered by the ROIs. Hence, mineralization fronts, where the degree of mineralization changes rapidly with the location, were excluded from this study. Therefore, the elemental distributions in these critical regions remain unknown (Figure 4.19). The detailed evaluation of these interfaces between mineralized and non-mineralized bone tissue will be discussed in the next chapter.

4.4 Changes of the Elemental Compositions of Bone at Mineralization Fronts

4.4.1 Measurement routine

To address this question the EDX routine as introduced in Chapter 3.5 was modified to perform profile scans to investigate the elemental distributions in defined distances to the mineralization front. Therefore, ROIs of 39.1 $\times$ 29.3 μm^2 were divided into 2 μm broad

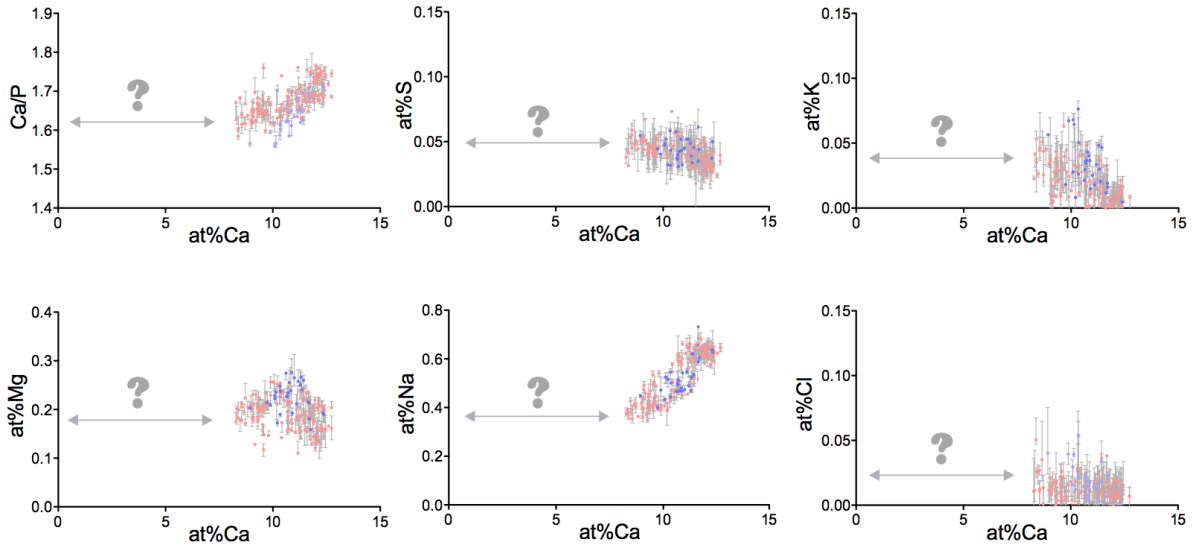

Figure 4.19: Energy dispersive X-ray analysis (EDX) results separated into measurements taken at the periosteal (blue) and the osteonal site (red): According to the study design and the measurement setup no information can be gained on the low mineralized regions between 0 and 8 $at\%Ca$.

stripes placed parallel to the mineralization front (see Figure 4.21 and Figure 4.21). Spectra were recorded for each box with measurement parameters described above (Chapter 3.5), thus providing an average spectrum for every 29 3 2 m^2 sub-ROI. Mineralization fronts were identified using BEI images as shown in Figure 4.21 with respect to following criteria:

- There is a layer of non-mineralized bone matrix (osteoid) adjacent to the surface of a bone packet with low mineral content (Figure 4.21).

- There is a typical gradient of osteoid to the mineralized matrix, exhibiting cloudy dots of mineralized clusters.

Spectra were consecutively recorded for each sub-ROI and quantification of the elements of interest was performed as described above (Chapter 3.5). Figure 4.20 gives an example of a spectra-set obtained within one ROI covering the mineralization front and the adjacent tissue.

Such datasets were obtained in the samples originating from femora of children ($n = 4$, samples #4 7 in Table 3.1) at three periosteal mineralization fronts (in one case only two) and three osteonal mineralization fronts. Samples from adults were not investigated due to rare periosteal bone forming sites. For the illustration of quantitative results, elemental concentrations can be plotted versus the location. The spectra were shifted to set the visually defined middle of the mineralization to the zero mark of the x-axis as shown in Figure 4.21.

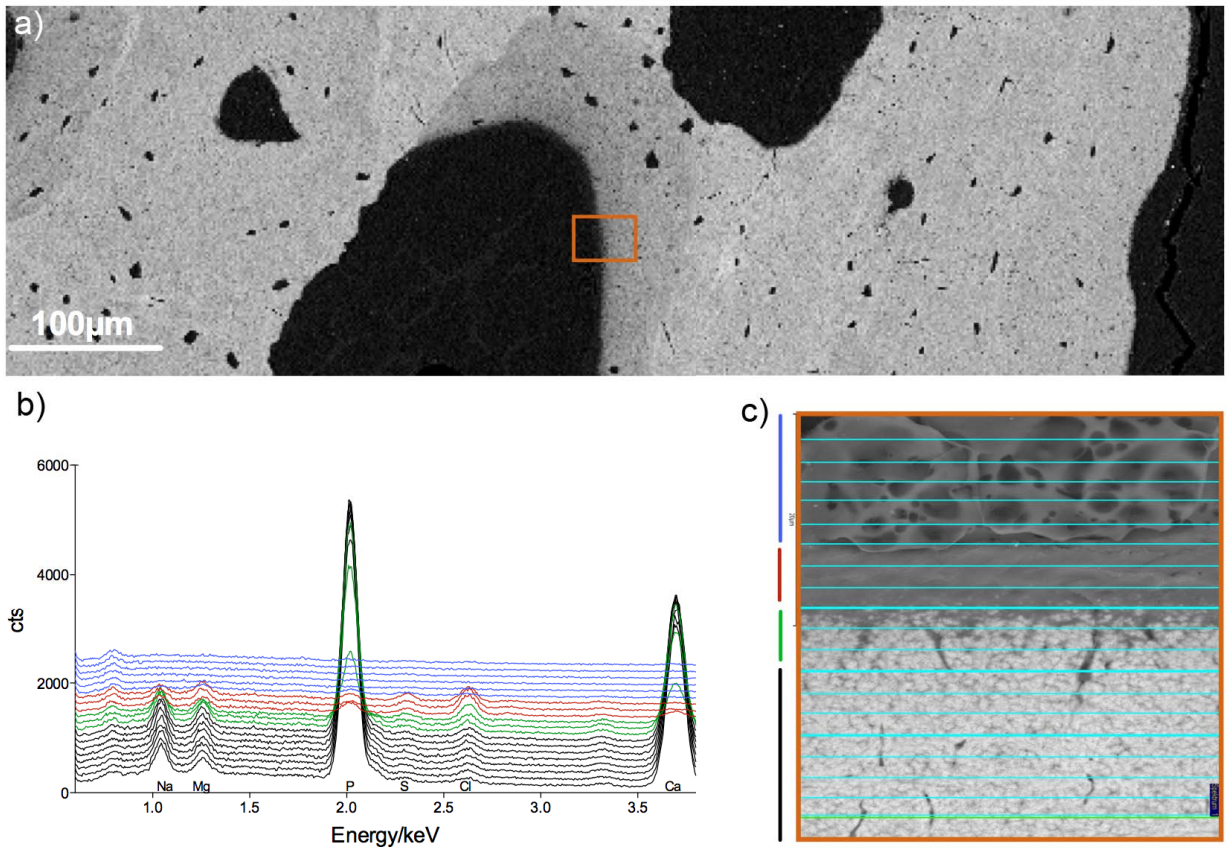

Figure 4.20: Backscattered electron image (BEI) (upper panel) of an osteon located in the femur cross section of a healthy child (a). In the lower panel a high - resolution BEI image of the mineralization-front region is shown. A grid of sub-regions of interest (sub-ROI) divides the ROI into 2 m thin stripes which were considered for successive energy dispersive X-ray (EDX) measurements (b). The corresponding spectra are shown exhibiting the elemental peaks typical for bone. The colors correspond to the mineralized matrix (black), transition zone (green), osteoid (red) and PMMA (blue) (c).

4.4.2 Results

The *Ca/P* ratio at mineralization fronts

Figure 4.22 shows the quantified results of one representative specimen (#10, Table 3.1). Detailed data from the other specimens are presented in Appendix 5. Surprisingly, there was a clear lower $Ca\ P$ ratio observed in the mineralized region next to a mineralization front at the periosteal site compared to the osteonal site. For all except one of the 23 analyzed profiles, there was a total site related separation of the $Ca\ P$ ratio. This was usually accompanied by a drop of the ratio even below 1.5 exclusively close to periosteal mineralization fronts. In general, $Ca\ P$ revealed to be below the theoretical value of perfect HAP ($Ca\ P = 1\,67$). According to extremely low Ca and P count rates in the osteoid the ratio was not evaluated in these regions.

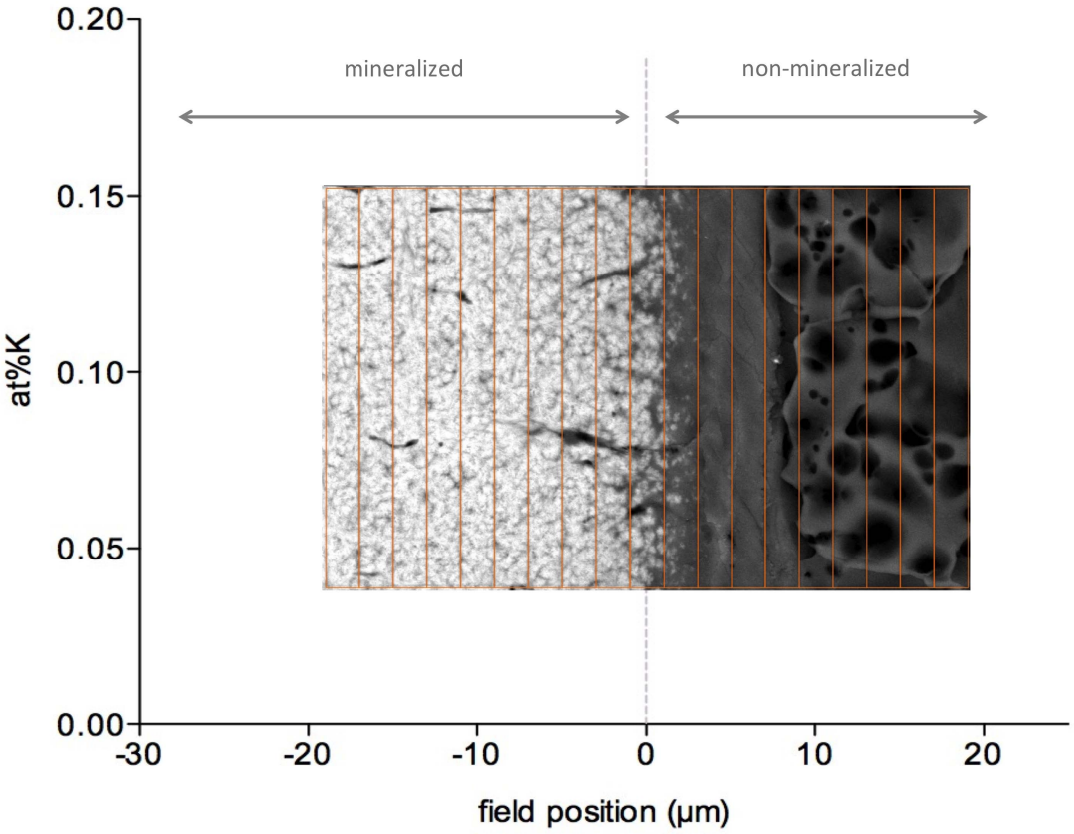

Figure 4.21: In the following (Figure 4.22) the elemental concentration is plotted vs. the relative location. Line profiles are shifted so, that the transition between mineralized bone matrix and osteoid is at $x = 0$. Hence, $x < 0$ corresponds to mineralized matrix and at $x > 0$ osteoid and PMMA are located.

Concentration of minor elements close to mineralization fronts

The Na concentrations were found to be distinctly increased close to periosteal mineralizing surfaces. For all samples a total separation of the data was observed, which was to some extend still present in the osteoid region. Consistently, also the Mg content exhibited increased values at periosteal mineralization fronts (Figure 4.22f). Although the separation of the data in the mineralized matrix was not as clear as for Na, in the osteoid region there were manifold increases in Mg concentrations observed for all datasets of all four samples at periosteal sites.

While K and Cl concentration were too low to be evaluated in the high mineralized matrix as investigated in Chapter 4.3, at the mineralization fronts evaluable values were obtained. Like Mg and Na, K and Cl concentrations were found to be increased at periosteal mineralization fronts. In the case of K this observation is most significant in the mineralized part of the ROI while Cl concentrations separate between the anatomical sites in the mineralized and in the non-mineralized tissue. Interestingly, a peak in the Cl content was seen for all sites in the osteoid. Such a peak was also discovered for the S concentration but in this case no difference between periosteal and osteonal sites were observed (Figure 4.22d).

Summary
As the reported elemental concentrations refer to the lowest mineralized regions in bone tissue and as $at\%Ca$ data were evaluated simultaneously to the minor elements, it is possible to insert the measurements in Figure 4.19. In Figure 4.23 the newly included data points, (each representing a sub-ROI) now also cover the very low mineralized region. This plot shows again the separation of the Ca/P values. Even in the already mineralized tissue at about 10 $at\%Ca$ (corresponding to sub-ROIs in $10 - 15$ μm distance to the mineralization front) there is a clear separation between the two sites showing lower Ca/P values at the periosteal mineralization fronts. This is in line with the location-dependent data evaluation as described above. Consistently K, Mg, N and Cl concentrations are clearly elevated at the periosteum compared to osteonal mineralization sites when normalizing for the Ca content. Note that in Figure 4.23 no data from the non-mineralized matrix are included.

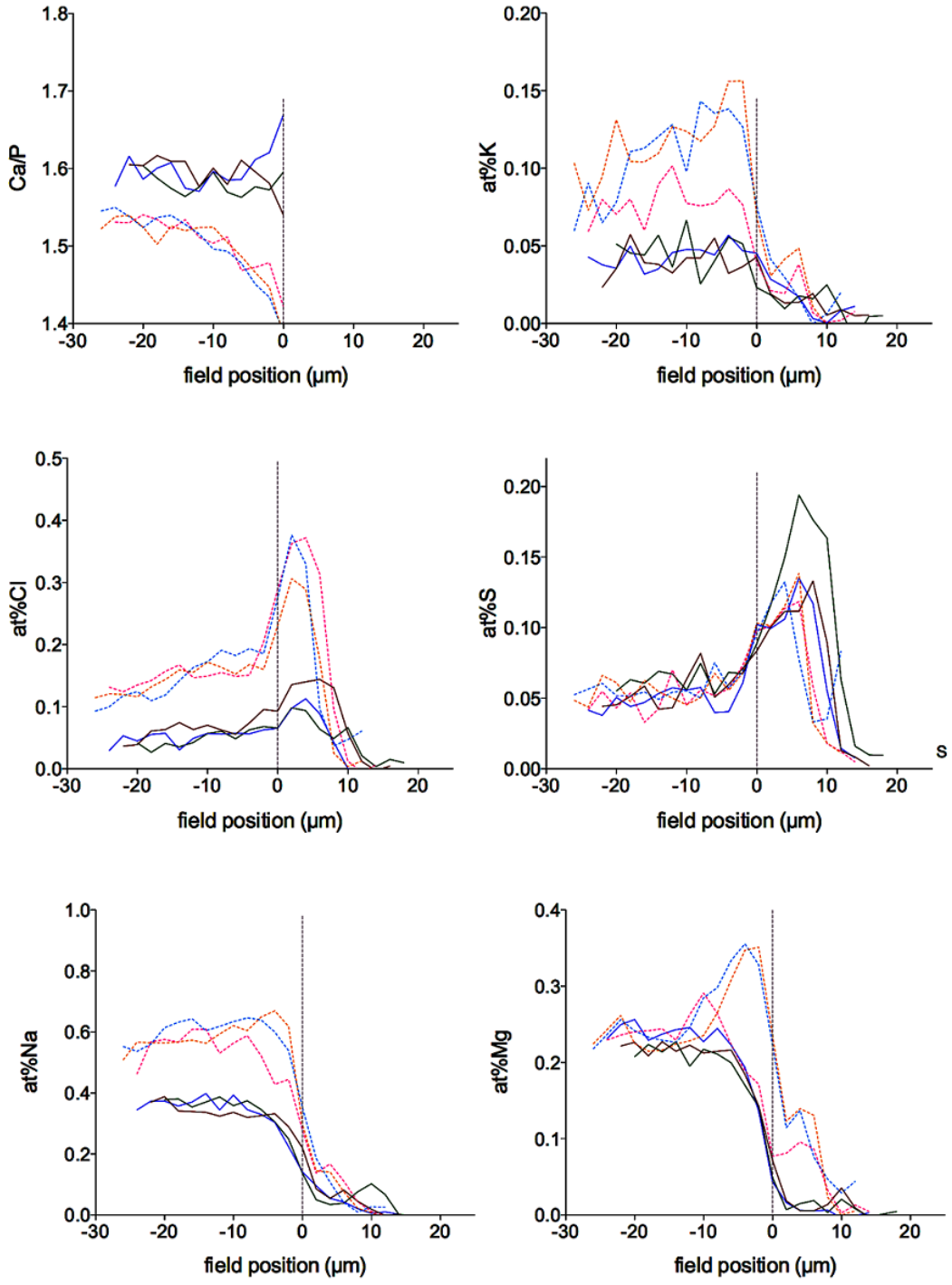

Figure 4.22: Ca/P ratio and quantified measurements of K, Cl, S, Na and Mg plotted as described in Figure 4.21. $x < 0$ corresponds to the mineralized matrix and at $x > 0$ osteoid and PMMA are located. Dashed lines refer to mineralization fronts located at the periosteal site while straight lines represent osteonal sites of active bone formation.

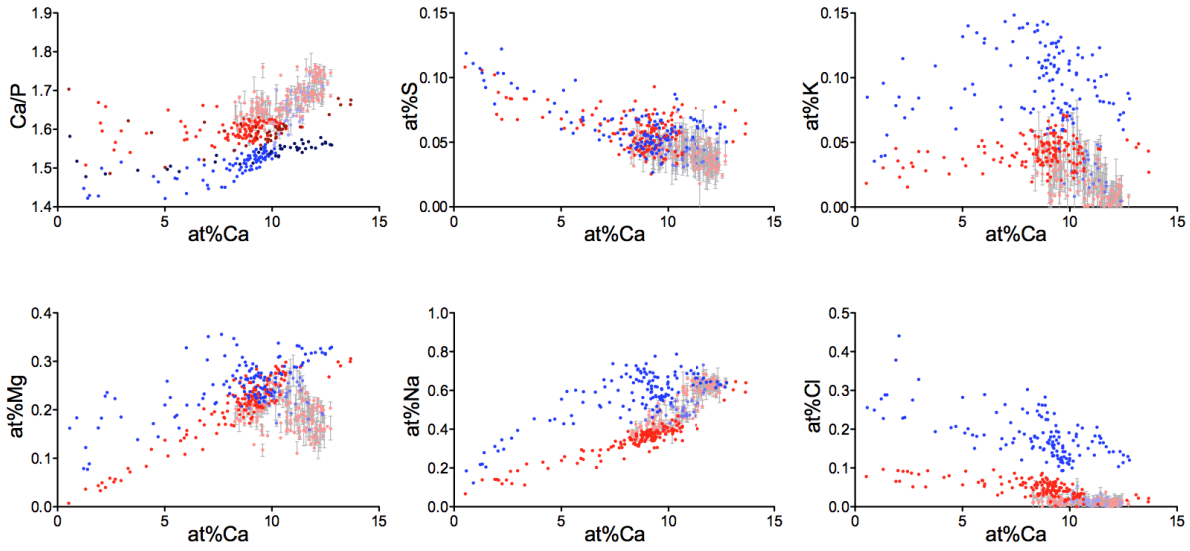

Figure 4.23: Energy dispersive X-ray analysis (EDX) results separated into measurements taken at the periosteal site (blue) and the osteonal site (red): In contrast to Figure 4.19 now also the data from the mineralization fronts are included (dark data points), thus covering the whole $at\%Ca$ range. The separation of the $Ca\ \ P$ ratio, K, Mg, Na and Cl with respect to the anatomical site are obvious. This is not observed for S.

4.4.3 Discussion and Outlook

Discussion

In the frame of this study we proofed that there is a difference in the bone material composition between regions close to osteonal and periosteal mineralization fronts in a group consisting of four children. Increased levels of K, Mg, Na and Cl and a decreased Ca/P ratio were observed at mineralizing surfaces at the periosteum when normalizing for relative location or $at\%Ca$. The S concentration seems to be the same for both anatomical sites. Consistently, the reduced Ca/P ratio and increased Mg content at periosteal mineralization fronts is also reflected by the results presented in Chapter 4.3.3, where we found increased P and Mg concentrations at periosteal bone regions in distinct distance to the bone surface.

Interestingly, the distribution of minor elements strongly depends on the localization relative to the mineralization front. The K content exhibits a peak in the mineralized bone matrix between 0 and 10 μm distance to the mineralization front at periosteal bone forming sites. This was not observed at osteonal regions where only very low K concentrations were measured. The results might indicate a stronger involvement of K in periosteal bone formation. Wiesmann et al. studied the role of K in the transition from non-mineralized predentin to mineralized dentin (a bone like material located in teeth) and suggested that monovalent ions like K might be more suitable to trigger extracellular matrix systems than bivalent ions. The involvement of K in apatite biomineralization was hypothesized [156]. According to our results, in this work an increase of K at the mineralization front is reported.

S and Cl contents revealed distinct peaks in the osteoid. While S concentrations were similar for both investigated sites, Cl was strongly increased at periosteal bone forming regions. The elevated S content at the osteoid is consistent with the literature where an abundant presence of proteinpolysachariedes (PS) at the mineralization fronts is reported. In that work also increased S concentrations (which are assigned to PS) were measured at the osteoid [44]. No literature was found describing an involvement of Cl in bone formation.

It was further shown that more Mg and Na are present at periosteal mineralization fronts compared to osteonal sites. Mg is known to substitute Ca in the HAP crystal [42, 153] and is reported to be a stabilizer of amorphous mineral phases as they might occur in early stages of mineralization [47]. In this context, different Mg concentrations are interesting. It is possible that various Mg content at the mineralization front indicates different or different amounts of HAP precursors.
There is hardly any information about the local distribution of Na in bone. It remains unclear whether Na binds to the apatite crystals or is part of the organic matrix.

These results suggest differences in the composition of newly formed bone matrix depending on the anatomical site. In the literature no systematic measurements of the elemental bone material composition at mineralization fronts are described until yet. Differential bone compositions close to mineralization fronts might also be influenced by the accessibility of mineralization precursors and nucleation centers [63, 62]. Osteons are encased in the mineralized matrix where a continuous resorption and formation of bone matrix occurs [52]. Hence,

at these sites the supply with Ca, P and mediators of mineralization might not be an issue due to resorption sites nearby, releasing necessary ions and proteins. The situation might change at the periosteal site where during skeletal growth global bone formation occurs. In this case the extensive supply with mineral precursors and modulators must be provided through the blood vessels, likely mediated by matrix vesicles [63, 62].

Outlook
Taking the considerations made above into account, it is not totally surprising that tissue close to mineralization fronts contains minor elements in different amounts. The various Ca/P ratio and the Mg concentrations might indicate the presence of differing Calciumphosphate phases during the early stages of mineralization depending on the anatomical site. To proof this hypothesis, additional experiments need to be performed. In this sense the actual study was extended and a follow up project is currently in progress:

- From the same four children unstained samples were embedded and prepared to perform Raman spectroscopy mappings covering mineralization fronts at osteonal, periosteal and endosteal sites. The corresponding regions were preselected using high resolution BEI. From these measurements we expect to see differences in the characteristics of the PO_4-related Raman peaks if other mineral phases than HAP are present close to the mineralization front.

- A beamtime application (European synchrotron radiation facility (ESRF) - beamline ID13) was submitted and is already approved. Using small- and wide-angle X-ray scattering, the mineral particle size and orientation will be evaluated close to mineralization fronts at different anatomical sites.

Limitations
Despite of the highly consistent results for all four specimens, the sample number is too low to allow extrapolations and general conclusions concerning other individuals. Comparable evaluations for adults are not possible according to the lack periosteal bone apposition.

It should be noted that results of the quantification procedure of EDX results for concentrations below 0.5 $at\%$ must be treated with caution according to the low X-ray count rates. This affects all reported values of the minor elements. Nevertheless, the relative comparison between various sites with similar degree of mineralization appears reliable and can be used for the considerations. In general, for a reliable quantification, a constant interaction volume is presupposed. This is likely valid for the mineralized bone matrix. When investigating osteoid regions the lower average atomic number of the target spot facilitates increased electron penetration and less X-ray absorption on the way out of the sample. This will adulterate the quantitative results possibly causing artifacts in the comparison between minor element concentrations in the mineralized and the non-mineralized matrix and must be taken into account for the interpretation of Figure 4.22. In contrast, relative changes are supposed to be reliable as long as matrices with equivalent degree of mineralization are compared.

As evaluated in detail in Chapter 3.5, beam damage contributes to systematical errors in the quantification of absolute values of elements while the Ca/P ratio remains unaffected. For the evaluation of the mineralization fronts regions of 60 μm^2 were analyzed with the same measurement parameters (same beam current and acquisition time) as the ROIs investigated in Chapter 4.3 (1145.6 μm^2). Consequently, the damage caused by the electrons in the current project is distinctly higher and in a strict sense, inserting the data points of both projects into one sheet as done in Figure 4.23 is problematic. Thus this must be considered for the comparison of the data of the two studies.

As stated above mineralization front regions were selected with respect to high-resolution BEI images. Despite the fact that only regions exhibiting a pattern characteristic for mineralization fronts were considered for evaluation, we have no final proof that these regions are sites of active bone formation. From our experience with qBEI image evaluation, it can be stated that these fronts most likely correspond to regions where bone was apposed immediately before death of the individual. However, there are bone diseases reported where mineralization is prohibited causing "old" mineralization fronts. In general, making use of the in-vivo Tetracycline labeling technique, it would be possible to prove, whether the considered regions represented states of active bone formation, but such an approach was not available for our samples.

Chapter 5

Summary

The purpose of the presented work was to gain new insight into the elemental composition of mineralized bone matrix at defined anatomical sites of healthy human bone tissue, and into mouse models linked to human genetic diseases. Hence, it was necessary to extend methods and routines for the characterization of mineralized bone matrix with a focus on its elemental composition.

Using these methodological developments, the question was addressed whether extensively elevated bone formation affects the mineralization kinetics of bone. This was done by means of a mouse model, likely relevant for future Osteoporosis treatment. Another aim was to shed light on the relationship between osteocyte lacunae canaliculi network (OLCN) types and the composition of the mineralized matrix, contributing to the active debate on osteocytic osteolysis. We decided to apply the developed tools also to mineralization fronts, reflecting a critical stage of bone development. Hereby, the goal was to reveal potential differences in the mineralization process, which are supposed to be reflected by different elemental compositions of regions close to bone forming sites.

Methodological developments
New measurement protocols for the combination of established and adapted characterization techniques were introduced. It is now possible to combine quantitative backscattered electron imaging (qBEI), energy dispersive X-ray analysis (EDX), confocal laser scanning microscopy (CLSM) and Raman micro-spectroscopy on the same regions of interest (ROI) to gain more comprehensive information on bone matrix mineralization.

The qBEI quantification protocol was successfully adapted to a state of the art field emission electron microscope (FESEM, Supra40, Zeiss, Oberkochen). Beam damage and counting statistic effects were examined and documented. In the proposed protocol stability of the primary electron beam and the backscattered electron detector are monitored to maintain constant sampling conditions. Measurements of the same ROIs performed with the Supra40 microscope and with the established and validated DSM962 system (Zeiss, Oberkochen) confirmed comparability of the results.

By developing a routine to match images examined with qBEI (local Ca concentration) and

CLSM (tissue age information), a tool was generated to gain tissue age specific information on the degree of mineralization in addition to Raman parameters collected in the same ROIs. This enhancement of established measurement routines provides access to the mineralization kinetics of fluorescent-labeled bone.

If beside the degree of mineralization also information on the concentration of major and minor elements is desired, a new established protocol for EDX analysis now facilitates quantification of these elements with a special focus on the Ca/P ratio. Limitations like adulterations due to electron beam damage and the impact of different quantification models are documented. EDX measurements can now be performed in a standardized way in compact bone regions and at mineralization fronts.

To characterize the OLCN in polymethylmethacrylate (PMMA) embedded bone samples the Rhodamine staining protocol was successfully adapted according to the water-free embedding procedure. Subsequent CLSM imaging led to impressive insight into the organization of the OLCN. As Rhodamine staining does not interfere with qBEI and EDX analysis, ROIs can be easily revisited making use of reflection images taken at the CLSM. Thus the bone composition can now be interpreted in the context of the OLCN structure.

A high affinity of Rhodamine to the non-mineralized bone matrix (osteoid) was observed. Hence, the presented staining procedure and subsequent CLSM imaging provides valuable information on the amount of osteoid. Thus this can be seen as a tool to visualize and to quantify mineralization defects, which are not accessible using qBEI.

In a technical study, the correlation of mineralization examined with qBEI ($wt\%Ca$) and Raman micro-spectroscopy ($mineral/matrix$) was compared. The gained regression between the quantities fit theoretical estimations and it was demonstrated that deviations from the regression line correspond to biological inhomogeneities. These data will support the interpretation of future studies were Raman and qBEI measurements are performed on the same ROIs.

Biological relevance
The presented adapted/extended methods were designed to gain a maximum of information on the bone material composition and structure at defined regions. In multiple studies, they were applied to murine and human bone samples investigating mineralized tissue in customized setups to address the regarding scientific question.

Making use of these tools, changes in the mineralization kinetics of Sost-knockout ($SostKO$) mice were found exclusively at the endocortical site of bone apposition. The outcomes explained the results of a previous study where lower bone matrix mineralization at cortical bone was indicated using conventional qBEI analysis. Raman parameters also indicated alterations of organic matrix in this region. Medical implications of these results are most likely as the administration of sclerostin antibodies (SclAB), which target the same pathway, features one of the most promising candidates for future treatment of Osteoporosis and other bone fragility diseases.
In a follow-up study the impact on the mineralization pattern of SclAB injection in a mouse

model of growing and adult Osteogenesis Imperfecta (OI) mice was examined. Using qBEI it was demonstrated that SclAB administration had the same effect on the mineralization of wild-type and OI mice. Compared to reports of other mouse models of less severe OI types, the response to the treatment was small, thus suggesting a treatment dependency on the severity of the phenotype. Additional studies are needed before treatment with SclAB can be considered for humans suffering OI.

Beside the determination of the degree of mineralization, the developed tools facilitate the analysis of the elemental composition (using EDX) with respect to the OLCN type at the same regions of human osteonal bone. Thus, it was demonstrated that the regions without visible network correspond to high mineralized regions. The concentration of Na clearly increases with the degree of mineralization while this is not the case for S and Mg. Surprisingly, differences were found in the Mg concentration and in the Ca/P ratio between osteonal regions (mainly radial orientated OLCN) and periosteal sites (highly parallel OLCN). These differences were confirmed when investigating mineralization fronts with EDX, revealing fundamental changes in the composition of osteoid and low mineralized bone matrix. Periosteal sites of bone formation exhibited a distinctly lower Ca/P ratio and higher K, Cl, N and Mg concentrations compared to osteonal bone forming sites. According to these findings, we assume differing mineralization mechanisms depending on the anatomical site. A running project, which targets this question, also includes sites of endosteal bone formation. Using Raman spectroscopy, and synchrotron small- and wide-angle scattering it is planed to determine the differences in the mineral crystal size and shape to further characterize the mineralization processes.

In conclusion, using the newly developed measurement routines, new insight into bone mineralization, composition and structure was gained. Their application in actively debated fields led to results of great biological and medical importance.

Bibliography

[1] H. Gupta, S. Schratter, W. Tesch, P. Roschger, A. Berzlanovich, T. Schoeberl, K. Klaushofer, and P. Fratzl, "Two different correlations between nanoindentation modulus and mineral content in the bone–cartilage interface," *Journal of Structural Biology*, vol. 149, no. 2, pp. 138–148, 2005.

[2] A. A. Lloyd, Z. X. Wang, and E. Donnelly, "Multiscale contribution of bone tissue material property heterogeneity to trabecular bone mechanical behavior," *Journal of Biomechanical Engineering*, vol. 137, no. 1, p. 010801, 2015.

[3] H. Kind, *Studien zur Frage der Osteolyse. Histologische Untersuchungen an frischen experimentellen Frakturen.* Fischer, 1951.

[4] L. F. Bonewald, "The amazing osteocyte," *Journal of Bone and Mineral Research*, vol. 26, no. 2, pp. 229–238, 2011.

[5] E. Bonucci, "The osteocyte: the underestimated conductor of the bone orchestra," *Rendiconti Lincei*, vol. 20, no. 3, pp. 237–254, 2009.

[6] L. J. Melton, E. A. Chrischilles, C. Cooper, A. W. Lane, and B. L. Riggs, "How many women have osteoporosis?," *Journal of Bone and Mineral Research*, vol. 20, no. 5, pp. 886–892, 2005.

[7] C. Cooper, G. Campion, and L. Melton Iii, "Hip fractures in the elderly: a world-wide projection," *Osteoporosis International*, vol. 2, no. 6, pp. 285–289, 1992.

[8] P. Garnero, E. Sornay-Rendu, M.-C. Chapuy, and P. D. Delmas, "Increased bone turnover in late postmenopausal women is a major determinant of osteoporosis," *Journal of Bone and Mineral Research*, vol. 11, no. 3, pp. 337–349, 1996.

[9] S. R. Cummings and L. J. Melton, "Epidemiology and outcomes of osteoporotic fractures," *The Lancet*, vol. 359, no. 9319, pp. 1761–1767, 2002.

[10] F. O. Kolb, "Skeletal renewal and metabolic bone disease.," *Archives of Internal Medicine*, vol. 127, no. 3, pp. 506–506, 1971.

[11] A. Forlino, W. A. Cabral, A. M. Barnes, and J. C. Marini, "New perspectives on osteogenesis imperfecta," *Nature Reviews Endocrinology*, vol. 7, no. 9, pp. 540–557, 2011.

[12] P. Roschger, N. Fratzl-Zelman, B. M. Misof, F. H. Glorieux, K. Klaushofer, and F. Rauch, "Evidence that abnormal high bone mineralization in growing children with osteogenesis imperfecta is not associated with specific collagen mutations," *Calcified Tissue International*, vol. 82, no. 4, pp. 263–270, 2008.

[13] S. Gourion-Arsiquaud, J. C. Burket, L. M. Havill, E. DiCarlo, S. B. Doty, R. Mendelsohn, M. C. van der Meulen, and A. L. Boskey, "Spatial variation in osteonal bone properties relative to tissue and animal age," *Journal of Bone and Mineral Research*, vol. 24, no. 7, pp. 1271–1281, 2009.

[14] P. Roschger, E. Paschalis, P. Fratzl, and K. Klaushofer, "Bone mineralization density distribution in health and disease," *Bone*, vol. 42, no. 3, pp. 456–466, 2008.

[15] L. Galvis, "Raman spectroscopy investigation of organic matrix orientation and chemistry changes during fracture healing," 2012. PhD. thesis at the "Technische Universität Berlin".

[16] S. Gamsjäger, M. Kazanci, E. P. Paschalis, and P. Fratzl, "Raman application in bone imaging," *Raman spectroscopy for soft Matter Applications*, pp. 225–267, 2009.

[17] A. Roschger, S. Gamsjaeger, B. Hofstetter, A. Masic, S. Blouin, P. Messmer, A. Berzlanovich, E. P. Paschalis, P. Roschger, K. Klaushofer, *et al.*, "Relationship between the v2po4/amide iii ratio assessed by raman spectroscopy and the calcium content measured by quantitative backscattered electron microscopy in healthy human osteonal bone," *Journal of Biomedical Optics*, vol. 19, no. 6, pp. 065002–065002, 2014.

[18] N. Hassler*, A. Roschger*, S. Gamsjaeger, I. Kramer, S. Lueger, A. van Lierop, P. Roschger, K. Klaushofer, E. Paschalis, M. Kneissel, *et al.*, "Sclerostin deficiency is linked to altered bone composition," *Journal of Bone and Mineral Research*, 2014.

[19] P. V. Bodine, "Wnt signaling control of bone cell apoptosis," *Cell Research*, vol. 18, no. 2, pp. 248–253, 2008.

[20] M. Moester, S. Papapoulos, C. Löwik, and R. Van Bezooijen, "Sclerostin: current knowledge and future perspectives," *Calcified Tissue International*, vol. 87, no. 2, pp. 99–107, 2010.

[21] A. Roschger, P. Roschger, P. Keplingter, K. Klaushofer, S. Abdullah, M. Kneissel, and F. Rauch, "Effect of sclerostin antibody treatment in a mouse model of severe osteogenesis imperfecta," *Bone*, vol. 66, pp. 182–188, 2014.

[22] B. Hesse, P. Varga, M. Langer, A. Pacureanu, S. Schrof, N. Männicke, H. Suhonen, P. Maurer, P. Cloetens, F. Peyrin, *et al.*, "Canalicular network morphology is the major determinant of the spatial distribution of mass density in human bone tissue-evidence by means of synchrotron radiation phase-contrast nano-ct," *Journal of Bone and Mineral Research*, 2014.

[23] H. Qing and L. F. Bonewald, "Osteocyte remodeling of the perilacunar and pericanalicular matrix," *International Journal of Oral Science*, vol. 1, no. 2, p. 59, 2009.

[24] S. Liu, W. Tang, J. Zhou, L. Vierthaler, and L. D. Quarles, "Distinct roles for intrinsic osteocyte abnormalities and systemic factors in regulation of fgf23 and bone mineralization in hyp mice," *American Journal of Physiology-Endocrinology and Metabolism*, vol. 293, no. 6, pp. E1636–E1644, 2007.

[25] P. Fratzl, H. Gupta, E. Paschalis, and P. Roschger, "Structure and mechanical quality of the collagen–mineral nano-composite in bone," *Journal of Materials Chemistry*, vol. 14, no. 14, pp. 2115–2123, 2004.

[26] P. M. Mayhew, C. D. Thomas, J. G. Clement, N. Loveridge, T. J. Beck, W. Bonfield, C. J. Burgoyne, and J. Reeve, "Relation between age, femoral neck cortical stability, and hip fracture risk," *The Lancet*, vol. 366, no. 9480, pp. 129–135, 2005.

[27] N. Napoli, J. Jin, K. Peters, R. Wustrack, S. Burch, A. Chau, J. Cauley, K. Ensrud, M. Kelly, and D. M. Black, "Are women with thicker cortices in the femoral shaft at higher risk of subtrochanteric/diaphyseal fractures? the study of osteoporotic fractures," *The Journal of Clinical Endocrinology & Metabolism*, vol. 97, no. 7, pp. 2414–2422, 2012.

[28] H. Chen, X. Zhou, S. Shoumura, S. Emura, and Y. Bunai, "Age-and gender-dependent changes in three-dimensional microstructure of cortical and trabecular bone at the human femoral neck," *Osteoporosis International*, vol. 21, no. 4, pp. 627–636, 2010.

[29] S. Mori, R. Harruff, W. Ambrosius, and D. Burr, "Trabecular bone volume and microdamage accumulation in the femoral heads of women with and without femoral neck fractures," *Bone*, vol. 21, no. 6, pp. 521–526, 1997.

[30] F. A. Schulte, F. M. Lambers, G. Kuhn, and R. Mï¿½ller, "In vivo micro-computed tomography allows direct three-dimensional quantification of both bone formation and bone resorption parameters using time-lapsed imaging," *Bone*, vol. 48, no. 3, pp. 433–442, 2011.

[31] S. Weiner, W. Traub, and H. D. Wagner, "Lamellar bone: structure–function relations," *Journal of Structural Biology*, vol. 126, no. 3, pp. 241–255, 1999.

[32] H. Gupta, U. Stachewicz, W. Wagermaier, P. Roschger, H. Wagner, and P. Fratzl, "Mechanical modulation at the lamellar level in osteonal bone," *Journal of Materials Research*, vol. 21, no. 08, pp. 1913–1921, 2006.

[33] H. Ritzel, M. Amling, M. Pösl, M. Hahn, and G. Delling, "The thickness of human vertebral cortical bone and its changes in aging and osteoporosis: A histomorphometric analysis of the complete spinal column from thirty-seven autopsy specimens," *Journal of Bone and Mineral Research*, vol. 12, no. 1, pp. 89–95, 1997.

[34] M. Mullender, D. Van der Meer, R. Huiskes, and P. Lips, "Osteocyte density changes in aging and osteoporosis," *Bone*, vol. 18, no. 2, pp. 109–113, 1996.

[35] H. Qing, L. Ardeshirpour, P. Divieti Pajevic, V. Dusevich, K. Jähn, S. Kato, J. Wysolmerski, and L. F. Bonewald, "Demonstration of osteocytic perilacunar/canalicular remodeling in mice during lactation," *Journal of Bone and Mineral Research*, vol. 27, no. 5, pp. 1018–1029, 2012.

[36] *Philosophical Transactions of the Royal Society of London. Coverage: 1776-1886*, vol. 66-177. The Royal Society, 1966.

[37] H. S. Gupta, J. Seto, W. Wagermaier, P. Zaslansky, P. Boesecke, and P. Fratzl, "Cooperative deformation of mineral and collagen in bone at the nanoscale," *Proceedings of the National Academy of Sciences*, vol. 103, no. 47, pp. 17741–17746, 2006.

[38] W. Wagermaier, H. Gupta, A. Gourrier, M. Burghammer, P. Roschger, and P. Fratzl, "Spiral twisting of fiber orientation inside bone lamellae," *Biointerphases*, vol. 1, no. 1, pp. 1–5, 2006.

[39] M. A. Rubin, I. Jasiuk, J. Taylor, J. Rubin, T. Ganey, and R. P. Apkarian, "Tem analysis of the nanostructure of normal and osteoporotic human trabecular bone," *Bone*, vol. 33, no. 3, pp. 270–282, 2003.

[40] F. Meirer, B. Pemmer, G. Pepponi, N. Zoeger, P. Wobrauschek, S. Sprio, A. Tampieri, J. Goettlicher, R. Steininger, S. Mangold, *et al.*, "Assessment of chemical species of lead accumulated in tidemarks of human articular cartilage by x-ray absorption near-edge structure analysis," *Journal of Synchrotron Radiation*, vol. 18, no. 2, pp. 238–244, 2011.

[41] C. Li, O. Paris, S. Siegel, P. Roschger, E. P. Paschalis, K. Klaushofer, and P. Fratzl, "Strontium is incorporated into mineral crystals only in newly formed bone during strontium ranelate treatment," *Journal of Bone and Mineral Research*, vol. 25, no. 5, pp. 968–975, 2010.

[42] E. Bertoni, A. Bigi, G. Cojazzi, M. Gandolfi, S. Panzavolta, and N. Roveri, "Nanocrystals of magnesium and fluoride substituted hydroxyapatite," *Journal of Inorganic Biochemistry*, vol. 72, no. 1, pp. 29–35, 1998.

[43] J. E. Coleman, "Structure and mechanism of alkaline phosphatase," *Annual Review of Biophysics and Biomolecular Structure*, vol. 21, no. 1, pp. 441–483, 1992.

[44] D. Baylink, J. Wergedal, and E. Thompson, "Loss of proteinpolysaccharides at sites where bone mineralization is initiated," *Journal of Histochemistry & Cytochemistry*, vol. 20, no. 4, pp. 279–292, 1972.

[45] W. R. Thompson, S. Modla, B. J. Grindel, K. J. Czymmek, C. B. Kirn-Safran, L. Wang, R. L. Duncan, and M. C. Farach-Carson, "Perlecan/hspg2 deficiency alters

the pericellular space of the lacunocanalicular system surrounding osteocytic processes in cortical bone," *Journal of Bone and Mineral Research*, vol. 26, no. 3, pp. 618–629, 2011.

[46] A. Roschger, J. Hofstaetter, B. Pemmer, N. Zoeger, P. Wobrauschek, G. Falkenberg, R. Simon, A. Berzlanovich, H. Thaler, P. Roschger, *et al.*, "Differential accumulation of lead and zinc in double-tidemarks of articular cartilage," *Osteoarthritis and Cartilage*, vol. 21, no. 11, pp. 1707–1715, 2013.

[47] A. Boskey and A. Posner, "Magnesium stabilization of amorphous calcium phosphate: a kinetic study," *Materials Research Bulletin*, vol. 9, no. 7, pp. 907–916, 1974.

[48] T. Wada, T. Nakashima, N. Hiroshi, and J. M. Penninger, "Rankl–rank signaling in osteoclastogenesis and bone disease," *Trends in Molecular Medicine*, vol. 12, no. 1, pp. 17–25, 2006.

[49] C. Y. Logan and R. Nusse, "The wnt signaling pathway in development and disease," *Annual Review of Cell and Developmental Biology*, vol. 20, pp. 781–810, 2004.

[50] D. Dempster, D. Felsenberg, and S. van der Geest, *The Bone Quality Book: A Guide to Factors Influencing Bone Strength*. Excerpta Medica Elsevier, 2006.

[51] N. A. Sims and C. Vrahnas, "Regulation of cortical and trabecular bone mass by communication between osteoblasts, osteocytes and osteoclasts," *Archives of Biochemistry and Biophysics*, 2014.

[52] R. Marcus, D. Feldman, D. Nelson, and C. J. Rosen, *Fundamentals of osteoporosis*. Academic Press, 2009.

[53] S. Gamsjaeger, B. Buchinger, E. Zwettler, R. Recker, D. Black, J. A. Gasser, E. F. Eriksen, K. Klaushofer, and E. P. Paschalis, "Bone material properties in actively bone-forming trabeculae in postmenopausal women with osteoporosis after three years of treatment with once-yearly zoledronic acid," *Journal of Bone and Mineral Research*, vol. 26, no. 1, pp. 12–18, 2011.

[54] M. Hesse, L. F. Fröhlich, U. Zeitz, B. Lanske, and R. G. Erben, "Ablation of vitamin d signaling rescues bone, mineral, and glucose homeostasis in fgf-23 deficient mice," *Matrix Biology*, vol. 26, no. 2, pp. 75–84, 2007.

[55] B. Hofstetter, S. Gamsjaeger, R. J. Phipps, R. R. Recker, F. H. Ebetino, K. Klaushofer, and E. P. Paschalis, "Effects of alendronate and risedronate on bone material properties in actively forming trabecular bone surfaces," *Journal of Bone and Mineral Research*, vol. 27, no. 5, pp. 995–1003, 2012.

[56] S. Gamsjaeger, W. Brozek, R. Recker, K. Klaushofer, and E. P. Paschalis, "Transmenopausal changes in trabecular bone quality," *Journal of Bone and Mineral Research*, vol. 29, no. 3, pp. 608–617, 2014.

[57] F. Melsen and L. Mosekilde, "Trabecular bone mineralization lag time determined by tetracycline double-labeling in normal and certain pathological conditions," *Acta Pathologica Microbiologica Scandinavica Section A Pathology*, vol. 88, no. 1-6, pp. 83–88, 1980.

[58] V. Uskoković and D. P. Uskoković, "Nanosized hydroxyapatite and other calcium phosphates: chemistry of formation and application as drug and gene delivery agents," *Journal of Biomedical Materials Research Part B: Applied Biomaterials*, vol. 96, no. 1, pp. 152–191, 2011.

[59] K. Onuma and A. Ito, "Cluster growth model for hydroxyapatite," *Chemistry of Materials*, vol. 10, no. 11, pp. 3346–3351, 1998.

[60] I. Melikhov, "Crystallization behavior of nanodisperse phases," *Inorganic Materials*, vol. 36, no. 3, pp. 278–286, 2000.

[61] G. Boivin and P. Meunier, "Methodological considerations in measurement of bone mineral content," *Osteoporosis International*, vol. 14, pp. 22–28, 2003.

[62] E. E. Golub, "Role of matrix vesicles in biomineralization," *Biochimica et Biophysica Acta (BBA)-General Subjects*, vol. 1790, no. 12, pp. 1592–1598, 2009.

[63] R. J. Majeska and R. E. Wuthier, "Studies on matrix vesicles isolated from chick epiphyseal cartilage association of pyrophosphatase and atpase activities with alkaline phosphatase," *Biochimica et Biophysica Acta (BBA)-Enzymology*, vol. 391, no. 1, pp. 51–60, 1975.

[64] C. Wennberg, L. Hessle, P. Lundberg, S. Mauro, S. Narisawa, U. H. Lerner, and J. L. Millán, "Functional characterization of osteoblasts and osteoclasts from alkaline phosphatase knockout mice," *Journal of Bone and Mineral Research*, vol. 15, no. 10, pp. 1879–1888, 2000.

[65] K. Johnson, L. Hessle, S. Vaingankar, C. Wennberg, S. Mauro, S. Narisawa, J. Goding, K. Sano, J. Millan, and R. Terkeltaub, "Osteoblast tissue-nonspecific alkaline phosphatase antagonizes and regulates pc-1," *American Journal of Physiology-Regulatory, Integrative and Comparative Physiology*, vol. 279, no. 4, pp. R1365–R1377, 2000.

[66] F. Barvencik, F. T. Beil, M. Gebauer, B. Busse, T. Koehne, S. Seitz, J. Zustin, P. Pogoda, T. Schinke, and M. Amling, "Skeletal mineralization defects in adult hypophosphatasia - a clinical and histological analysis," *Osteoporosis International*, vol. 22, no. 10, pp. 2667–2675, 2011.

[67] W. Tesch, T. Vandenbos, P. Roschgr, N. Fratzl-Zelman, K. Klaushofer, W. Beertsen, and P. Fratzl, "Orientation of mineral crystallites and mineral density during skeletal development in mice deficient in tissue nonspecific alkaline phosphatase," *Journal of Bone and Mineral Research*, vol. 18, no. 1, pp. 117–125, 2003.

[68] P. Fratzl, N. Fratzl-Zelman, K. Klaushofer, G. Vogl, and K. Koller, "Nucleation and growth of mineral crystals in bone studied by small-angle x-ray scattering," *Calcified Tissue International*, vol. 48, no. 6, pp. 407–413, 1991.

[69] S. Weiner and H. D. Wagner, "The material bone: structure-mechanical function relations," *Annual Review of Materials Science*, vol. 28, no. 1, pp. 271–298, 1998.

[70] B. Xie and G. H. Nancollas, "How to control the size and morphology of apatite nanocrystals in bone," *Proceedings of the National Academy of Sciences*, vol. 107, no. 52, pp. 22369–22370, 2010.

[71] R. FV, *Untersuchungen uber Rachitis und Osteomalacia*. Jena: Gustav Fischer, 1920.

[72] P. ten Dijke, C. Krause, D. J. De Gorter, C. W. Löwik, and R. L. Van Bezooijen, "Osteocyte-derived sclerostin inhibits bone formation: its role in bone morphogenetic protein and wnt signaling," *The Journal of Bone & Joint Surgery*, vol. 90, no. Supplement 1, pp. 31–35, 2008.

[73] A. H. van Lierop, N. A. Hamdy, H. Hamersma, R. L. van Bezooijen, J. Power, N. Loveridge, and S. E. Papapoulos, "Patients with sclerosteosis and disease carriers: human models of the effect of sclerostin on bone turnover," *Journal of Bone and Mineral Research*, vol. 26, no. 12, pp. 2804–2811, 2011.

[74] I. Kramer, G. G. Loots, A. Studer, H. Keller, and M. Kneissel, "Parathyroid hormone (pth)–induced bone gain is blunted in sost overexpressing and deficient mice," *Journal of Bone and Mineral Research*, vol. 25, no. 2, pp. 178–189, 2010.

[75] R. Recker, C. Benson, T. Matsumoto, M. Bolognese, D. Robins, J. Alam, A. Y. Chiang, L. Hu, J. H. Krege, H. Sowa, *et al.*, "A randomized, double-blind phase 2 clinical trial of blosozumab, a sclerostin antibody, in postmenopausal women with low bone mineral density," *Journal of Bone and Mineral Research*, 2014.

[76] B. P. Sinder, M. M. Eddy, M. S. Ominsky, M. S. Caird, J. C. Marini, and K. M. Kozloff, "Sclerostin antibody improves skeletal parameters in a brtl/+ mouse model of osteogenesis imperfecta," *Journal of Bone and Mineral Research*, vol. 28, no. 1, pp. 73–80, 2013.

[77] X. Li, M. S. Ominsky, Q.-T. Niu, N. Sun, B. Daugherty, D. D'Agostin, C. Kurahara, Y. Gao, J. Cao, J. Gong, *et al.*, "Targeted deletion of the sclerostin gene in mice results in increased bone formation and bone strength," *Journal of Bone and Mineral Research*, vol. 23, no. 6, pp. 860–869, 2008.

[78] S. Zhao, Y. Kato, Y. Zhang, S. Harris, S. Ahuja, and L. Bonewald, "Mlo-y4 osteocyte-like cells support osteoclast formation and activation," *Journal of Bone and Mineral Research*, vol. 17, no. 11, pp. 2068–2079, 2002.

[79] T. Nakashima, M. Hayashi, T. Fukunaga, K. Kurata, M. Oh-hora, J. Q. Feng, L. F. Bonewald, T. Kodama, A. Wutz, E. F. Wagner, *et al.*, "Evidence for osteocyte

regulation of bone homeostasis through rankl expression," *Nature Medicine*, vol. 17, no. 10, pp. 1231–1234, 2011.

[80] L. F. Bonewald and M. L. Johnson, "Osteocytes, mechanosensing and wnt signaling," *Bone*, vol. 42, no. 4, pp. 606–615, 2008.

[81] H. Vaananen, H. Zhao, M. Mulari, and J. M. Halleen, "The cell biology of osteoclast function," *Journal of Cell Science*, vol. 113, no. 3, pp. 377–381, 2000.

[82] N. E. Lane, W. Yao, M. Balooch, R. K. Nalla, G. Balooch, S. Habelitz, J. H. Kinney, and L. F. Bonewald, "Glucocorticoid-treated mice have localized changes in trabecular bone material properties and osteocyte lacunar size that are not observed in placebo-treated or estrogen-deficient mice," *Journal of Bone and Mineral Research*, vol. 21, no. 3, pp. 466–476, 2006.

[83] K. Tazawa, K. Hoshi, S. Kawamoto, M. Tanaka, S. Ejiri, and H. Ozawa, "Osteocytic osteolysis observed in rats to which parathyroid hormone was continuously administered," *Journal of Bone and Mineral Metabolism*, vol. 22, no. 6, pp. 524–529, 2004.

[84] S. A. Lloyd, A. E. Loiselle, Y. Zhang, and H. J. Donahue, "Evidence for the role of connexin 43-mediated intercellular communication in the process of intracortical bone resorption via osteocytic osteolysis," *BMC Musculoskeletal Disorders*, vol. 15, no. 1, p. 122, 2014.

[85] M. Kerschnitzki, P. Kollmannsberger, M. Burghammer, G. N. Duda, R. Weinkamer, W. Wagermaier, and P. Fratzl, "Architecture of the osteocyte network correlates with bone material quality," *Journal of Bone and Mineral Research*, vol. 28, no. 8, pp. 1837–1845, 2013.

[86] E. M. Aarden, P. J. Nijweide, and E. H. Burger, "Function of osteocytes in bone," *Journal of Cellular Biochemistry*, vol. 55, no. 3, pp. 287–299, 1994.

[87] M. Haine and V. Cosslett, *The electron microscope.* E & FN Spon Limited, 1961.

[88] J. I. Goldstein, D. E. Newbury, P. Echlin, D. C. Joy, C. Fiori, E. Lifshin, *et al.*, *Scanning electron microscopy and X-ray microanalysis. A text for biologists, materials scientists, and geologists.* Plenum Publishing Corporation, 1981.

[89] J. H. Wittke, "http://www4.nau.edu/microanalysis/microprobe-sem/instrumentation.html," 2008.

[90] P. Roschger, "Characterization of mineralized tissue in vertebrates by scanning microscopic methods for material science and medicine," 2003. Postdoctoral lecture qualification at the Montanuniversitaet Leoben.

[91] J. Skedros, R. Bloebaum, K. Bachus, and T. Boyce, "The meaning of graylevels in backscattered electron images of bone," *Journal of Biomedical Materials Research*, vol. 27, no. 1, pp. 47–56, 1993.

[92] A. Boyde and S. Jones, "Back-scattered electron imaging of skeletal tissues," *Metabolic Bone Disease and Related Research*, vol. 5, no. 3, pp. 145–150, 1984.

[93] P. Roschger, P. Fratzl, J. Eschberger, and K. Klaushofer, "Validation of quantitative backscattered electron imaging for the measurement of mineral density distribution in human bone biopsies," *Bone*, vol. 23, no. 4, pp. 319–326, 1998.

[94] H. Seiler, "Secondary electron emission in the scanning electron microscope," *Journal of Applied Physics*, vol. 54, no. 11, pp. R1–R18, 1983.

[95] P. Roschger, H. Plenk Jr, K. Klaushofer, and J. Eschberger, "A new scanning electron microscopy approach to the quantification of bone mineral distribution: backscattered electron image grey-levels correlated to calcium k alpha-line intensities.," *Scanning Microscopy*, vol. 9, no. 1, pp. 75–86, 1995.

[96] B. M. Misof, P. Roschger, F. Cosman, E. S. Kurland, W. Tesch, P. Messmer, D. W. Dempster, J. Nieves, E. Shane, P. Fratzl, *et al.*, "Effects of intermittent parathyroid hormone administration on bone mineralization density in iliac crest biopsies from patients with osteoporosis: a paired study before and after treatment," *The Journal of Clinical Endocrinology & Metabolism*, vol. 88, no. 3, pp. 1150–1156, 2003.

[97] B. Misof, M. Bodingbauer, P. Roschger, T. Wekerle, B. Pakrah, M. Haas, A. Kainz, R. Oberbauer, F. Mühlbacher, and K. Klaushofer, "Short-term effects of high-dose zoledronic acid treatment on bone mineralization density distribution after orthotopic liver transplantation," *Calcified Tissue International*, vol. 83, no. 3, pp. 167–175, 2008.

[98] B. M. Misof, P. Roschger, D. Gabriel, E. P. Paschalis, E. F. Eriksen, R. R. Recker, J. A. Gasser, and K. Klaushofer, "Annual intravenous zoledronic acid for three years increased cancellous bone matrix mineralization beyond normal values in the horizon biopsy cohort," *Journal of Bone and Mineral Research*, vol. 28, no. 3, pp. 442–448, 2013.

[99] N. Fratzl-Zelman, P. Roschger, B. M. Misof, K. Nawrot-Wawrzyniak, S. Pötter-Lang, C. Muschitz, H. Resch, K. Klaushofer, and E. Zwettler, "Fragility fractures in men with idiopathic osteoporosis are associated with undermineralization of the bone matrix without evidence of increased bone turnover," *Calcified Tissue International*, vol. 88, no. 5, pp. 378–387, 2011.

[100] B. M. Misof, P. Roschger, T. Baldini, C. L. Raggio, V. Zraick, L. Root, A. L. Boskey, K. Klaushofer, P. Fratzl, and N. P. Camacho, "Differential effects of alendronate treatment on bone from growing osteogenesis imperfecta and wild-type mouse," *Bone*, vol. 36, no. 1, pp. 150–158, 2005.

[101] B. Misof, P. Roschger, W. Tesch, P. Baldock, A. Valenta, P. Messmer, J. Eisman, A. Boskey, E. Gardiner, P. Fratzl, *et al.*, "Targeted overexpression of vitamin d receptor in osteoblasts increases calcium concentration without affecting structural properties of bone mineral crystals," *Calcified Tissue International*, vol. 73, no. 3, pp. 251–257, 2003.

[102] C. Hamann, C. Goettsch, J. Mettelsiefen, V. Henkenjohann, M. Rauner, U. Hempel, R. Bernhardt, N. Fratzl-Zelman, P. Roschger, S. Rammelt, *et al.*, "Delayed bone regeneration and low bone mass in a rat model of insulin-resistant type 2 diabetes mellitus is due to impaired osteoblast function," *American Journal of Physiology-Endocrinology and Metabolism*, vol. 301, no. 6, pp. E1220–E1228, 2011.

[103] D. Attwood, *Soft x-rays and extreme ultraviolet radiation: principles and applications*. Cambridge university press, 1999.

[104] M. O. Krause, "Atomic radiative and radiationless yields for k and l shells," *Journal of Physical and Chemical Reference Data*, vol. 8, no. 2, pp. 307–327, 1979.

[105] P. Larkin, *Infrared and Raman spectroscopy; principles and spectral interpretation*. Elsevier, 2011.

[106] W. Demtröder, *Laser spectroscopy*, vol. 3. Springer, 1982.

[107] M. Tanaka and R. Young, "Review polarised raman spectroscopy for the study of molecular orientation distributions in polymers," *Journal of Materials Science*, vol. 41, no. 3, pp. 963–991, 2006.

[108] J. S. Nyman, A. J. Makowski, C. A. Patil, T. P. Masui, E. C. O Quinn, X. Bi, S. A. Guelcher, D. P. Nicollela, and A. Mahadevan-Jansen, "Measuring differences in compositional properties of bone tissue by confocal raman spectroscopy," *Calcified Tissue International*, vol. 89, no. 2, pp. 111–122, 2011.

[109] M. Amer, *Raman spectroscopy for soft matter applications*. John Wiley & Sons, 2009.

[110] M. D. Morris, W. F. Finney, R. M. Rajachar, and D. H. Kohn, "Bone tissue ultrastructural response to elastic deformation probed by raman spectroscopy," *Faraday discussions*, vol. 126, pp. 159–168, 2004.

[111] O. Akkus, A. Polyakova-Akkus, F. Adar, and M. B. Schaffler, "Aging of microstructural compartments in human compact bone," *Journal of Bone and Mineral Research*, vol. 18, no. 6, pp. 1012–1019, 2003.

[112] J. A. Timlin, A. Carden, and M. D. Morris, "Chemical microstructure of cortical bone probed by raman transects," *Applied Spectroscopy*, vol. 53, no. 11, pp. 1429–1435, 1999.

[113] S. Gamsjaeger, B. Hofstetter, E. Zwettler, R. Recker, J. Gasser, E. Eriksen, K. Klaushofer, and E. Paschalis, "Effects of 3 years treatment with once-yearly zoledronic acid on the kinetics of bone matrix maturation in osteoporotic patients," *Osteoporosis International*, vol. 24, no. 1, pp. 339–347, 2013.

[114] M. Kazanci, P. Roschger, E. Paschalis, K. Klaushofer, and P. Fratzl, "Bone osteonal tissues by raman spectral mapping: orientation–composition," *Journal of Structural Biology*, vol. 156, no. 3, pp. 489–496, 2006.

[115] E. Landi, G. Celotti, G. Logroscino, and A. Tampieri, "Carbonated hydroxyapatite as bone substitute," *Journal of the European Ceramic Society*, vol. 23, no. 15, pp. 2931–2937, 2003.

[116] M. Tsuboi and G. J. Thomas JR, "Raman scattering tensors in biological molecules and their assemblies," *Applied Spectroscopy Reviews*, vol. 32, no. 3, pp. 263–299, 1997.

[117] J. Pawley, *Handbook of biological confocal microscopy*. Springer, 2010.

[118] R. L. Price and W. G. J. Jerome, *Basic confocal microscopy*. Springer, 2011.

[119] M. Kerschnitzki, W. Wagermaier, P. Roschger, J. Seto, R. Shahar, G. N. Duda, S. Mundlos, and P. Fratzl, "The organization of the osteocyte network mirrors the extracellular matrix orientation in bone," *Journal of Structural Biology*, vol. 173, no. 2, pp. 303–311, 2011.

[120] N. Fratzl-Zelman, P. Roschger, A. Gourrier, M. Weber, B. Misof, N. Loveridge, J. Reeve, K. Klaushofer, and P. Fratzl, "Combination of nanoindentation and quantitative backscattered electron imaging revealed altered bone material properties associated with femoral neck fragility," *Calcified Tissue International*, vol. 85, no. 4, pp. 335–343, 2009.

[121] F. Chen, R. Guo, S. Itoh, L. Moreno, E. Rosenthal, T. Zappitelli, R. A. Zirngibl, A. Flenniken, W. Cole, M. Grynpas, *et al.*, "First mouse model for combined osteogenesis imperfecta and ehlers-danlos syndrome," *Journal of Bone and Mineral Research*, vol. 29, no. 6, pp. 1412–1423, 2014.

[122] R. Zoehrer, P. Roschger, E. P. Paschalis, J. G. Hofstaetter, E. Durchschlag, P. Fratzl, R. Phipps, and K. Klaushofer, "Effects of 3-and 5-year treatment with risedronate on bone mineralization density distribution in triple biopsies of the iliac crest in postmenopausal women," *Journal of Bone and Mineral Research*, vol. 21, no. 7, pp. 1106–1112, 2006.

[123] P. Fratzl, P. Roschger, N. Fratzl-Zelman, E. P. Paschalis, R. Phipps, and K. Klaushofer, "Evidence that treatment with risedronate in women with postmenopausal osteoporosis affects bone mineralization and bone volume," *Calcified Tissue International*, vol. 81, no. 2, pp. 73–80, 2007.

[124] J. G. Hofstaetter, P. Roschger, K. Klaushofer, and H. K. Kim, "Increased matrix mineralization in the immature femoral head following ischemic osteonecrosis," *Bone*, vol. 46, no. 2, pp. 379–385, 2010.

[125] P. Roschger, P. Fratzl, J. Eschberger, and K. Klaushofer, "Response to the letter to the editor by eg vajda and jg skedros," *Bone*, vol. 24, no. 6, pp. 620–621, 1999.

[126] R. Bloebaum, J. Skedros, E. Vajda, K. Bachus, and B. Constantz, "Determining mineral content variations in bone using backscattered electron imaging," *Bone*, vol. 20, no. 5, pp. 485–490, 1997.

[127] J. L. Holmes, K. N. Bachus, and R. D. Bloebaum, "Thermal effects of the electron beam and implications of surface damage in the analysis of bone tissue," *Scanning*, vol. 22, no. 4, pp. 243–248, 2000.

[128] P. Roschger, H. Gupta, A. Berzlanovich, G. Ittner, D. Dempster, P. Fratzl, F. Cosman, M. Parisien, R. Lindsay, J. Nieves, *et al.*, "Constant mineralization density distribution in cancellous human bone," *Bone*, vol. 32, no. 3, pp. 316–323, 2003.

[129] J. Cassella, N. Garrington, T. Stamp, and S. Ali, "An electron probe x-ray microanalytical study of bone mineral in osteogenesis imperfecta," *Calcified Tissue International*, vol. 56, no. 2, pp. 118–122, 1995.

[130] R. D. Bloebaum, J. L. Holmes, and J. G. Skedros, "Mineral content changes in bone associated with damage induced by the electron beam," *Scanning*, vol. 27, no. 5, pp. 240–248, 2005.

[131] J. L. Holmes, K. N. Bachus, and R. D. Bloebaum, "Thermal effects of the electron beam and implications of surface damage in the analysis of bone tissue," *Scanning*, vol. 22, no. 4, pp. 243–248, 2000.

[132] E. Donnelly, R. M. Williams, S. A. Downs, M. E. Dickinson, S. P. Baker, and M. C. van der Meulen, "Quasistatic and dynamic nanomechanical properties of cancellous bone tissue relate to collagen content and organization," *Journal of Materials Research*, vol. 21, no. 08, pp. 2106–2117, 2006.

[133] M. P. Whyte, "Hypophosphatasia," in *The Genetics of Osteoporosis and Metabolic Bone Disease*, pp. 335–356, Springer, 2000.

[134] K. Nawrot-Wawrzyniak, F. Varga, A. Nader, P. Roschger, S. Sieghart, E. Zwettler, K. Roetzer, S. Lang, R. Weinkamer, K. Klaushofer, *et al.*, "Effects of tumor-induced osteomalacia on the bone mineralization process," *Calcified Tissue International*, vol. 84, no. 4, pp. 313–323, 2009.

[135] M. F. Holick, "Sunlight and vitamin d for bone health and prevention of autoimmune diseases, cancers, and cardiovascular disease," *The American Journal of Clinical Nutrition*, vol. 80, no. 6, pp. 1678S–1688S, 2004.

[136] N. Fratzl-Zelman, I. Schmidt, P. Roschger, F. H. Glorieux, K. Klaushofer, P. Fratzl, F. Rauch, and W. Wagermaier, "Mineral particle size in children with osteogenesis imperfecta type i is not increased independently of specific collagen mutations," *Bone*, vol. 60, pp. 122–128, 2014.

[137] A. Ravaglioli, A. Krajewski, G. Celotti, A. Piancastelli, B. Bacchini, L. Montanari, G. Zama, and L. Piombi, "Mineral evolution of bone," *Biomaterials*, vol. 17, no. 6, pp. 617–622, 1996.

[138] K. J. Obrant and R. Odselius, "Electron microprobe investigation of calcium and phosphorus concentration in human bone trabeculae - both normal and in

posttraumatic osteopenia," *Calcified Tissue International*, vol. 37, no. 2, pp. 117–120, 1985.

[139] W. H. Bergstrom and W. M. Wallace, "Bone as a sodium and potassium reservoir," *Journal of Clinical Investigation*, vol. 33, no. 6, p. 867, 1954.

[140] S. Gourion-Arsiquaud, J. C. Burket, L. M. Havill, E. DiCarlo, S. B. Doty, R. Mendelsohn, M. C. van der Meulen, and A. L. Boskey, "Spatial variation in osteonal bone properties relative to tissue and animal age," *Journal of Bone and Mineral Research*, vol. 24, no. 7, pp. 1271–1281, 2009.

[141] R. Havaldar, S. Pilli, and B. Putti, "Effects of magnesium on mechanical properties of human bone," *Journal of Pharmacy and Biological Sciences*, vol. 7, no. 3, 2013.

[142] B. Wopenka and J. D. Pasteris, "A mineralogical perspective on the apatite in bone," *Materials Science and Engineering: C*, vol. 25, no. 2, pp. 131–143, 2005.

[143] M. R. McClung, A. Grauer, S. Boonen, M. A. Bolognese, J. P. Brown, A. Diez-Perez, B. L. Langdahl, J.-Y. Reginster, J. R. Zanchetta, S. M. Wasserman, *et al.*, "Romosozumab in postmenopausal women with low bone mineral density," *New England Journal of Medicine*, vol. 370, no. 5, pp. 412–420, 2014.

[144] R. K. Fuchs, M. E. Faillace, M. R. Allen, R. J. Phipps, L. M. Miller, and D. B. Burr, "Bisphosphonates do not alter the rate of secondary mineralization," *Bone*, vol. 49, no. 4, pp. 701–705, 2011.

[145] R. K. Fuchs, M. R. Allen, M. E. Ruppel, T. Diab, R. J. Phipps, L. M. Miller, and D. B. Burr, "In situ examination of the time-course for secondary mineralization of haversian bone using synchrotron fourier transform infrared microspectroscopy," *Matrix Biology*, vol. 27, no. 1, pp. 34–41, 2008.

[146] G. Boivin and P. Meunier, "The mineralization of bone tissue: a forgotten dimension in osteoporosis research," *Osteoporosis International*, vol. 14, no. 3, pp. 19–24, 2003.

[147] P. Schneider, M. Meier, R. Wepf, and R. Müller, "Serial fib/sem imaging for quantitative 3d assessment of the osteocyte lacuno-canalicular network," *Bone*, vol. 49, no. 2, pp. 304–311, 2011.

[148] P. Roschger, N. Fratzl-Zelman, B. M. Misof, F. H. Glorieux, K. Klaushofer, and F. Rauch, "Evidence that abnormal high bone mineralization in growing children with osteogenesis imperfecta is not associated with specific collagen mutations," *Calcified Tissue International*, vol. 82, no. 4, pp. 263–270, 2008.

[149] P. Milovanovic, E. A. Zimmermann, M. Hahn, D. Djonic, K. Püschel, M. Djuric, M. Amling, and B. Busse, "Osteocytic canalicular networks: morphological implications for altered mechanosensitivity," *ACS nano*, vol. 7, no. 9, pp. 7542–7551, 2013.

[150] A. Boyde, "The real response of bone to exercise," *Journal of Anatomy*, vol. 203, no. 2, pp. 173–189, 2003.

[151] B. Busse, D. Djonic, P. Milovanovic, M. Hahn, K. Püschel, R. O. Ritchie, M. Djuric, and M. Amling, "Decrease in the osteocyte lacunar density accompanied by hypermineralized lacunar occlusion reveals failure and delay of remodeling in aged human bone," *Aging cell*, vol. 9, no. 6, pp. 1065–1075, 2010.

[152] J. Barsony, Y. Sugimura, and J. G. Verbalis, "Osteoclast response to low extracellular sodium and the mechanism of hyponatremia-induced bone loss," *Journal of Biological Chemistry*, vol. 286, no. 12, pp. 10864–10875, 2011.

[153] C. Serre, M. Papillard, P. Chavassieux, J. Voegel, and G. Boivin, "Influence of magnesium substitution on a collagen–apatite biomaterial on the production of a calcifying matrix by human osteoblasts," *Journal of Biomedical Materials Research*, vol. 42, no. 4, pp. 626–633, 1998.

[154] T. A. Steitz, "Structural biology: A mechanism for all polymerases," *Nature*, vol. 391, no. 6664, pp. 231–232, 1998.

[155] B. Pemmer, A. Roschger, A. Wastl, J. Hofstaetter, P. Wobrauschek, R. Simon, H. Thaler, P. Roschger, K. Klaushofer, and C. Streli, "Spatial distribution of the trace elements zinc, strontium and lead in human bone tissue," *Bone*, vol. 57, no. 1, pp. 184–193, 2013.

[156] H.-P. Wiesmann, U. Plate, K. Zierold, and H. Höhling, "Potassium is involved in apatite biomineralization," *Journal of Dental Research*, vol. 77, no. 8, pp. 1654–1657, 1998.

Appendix

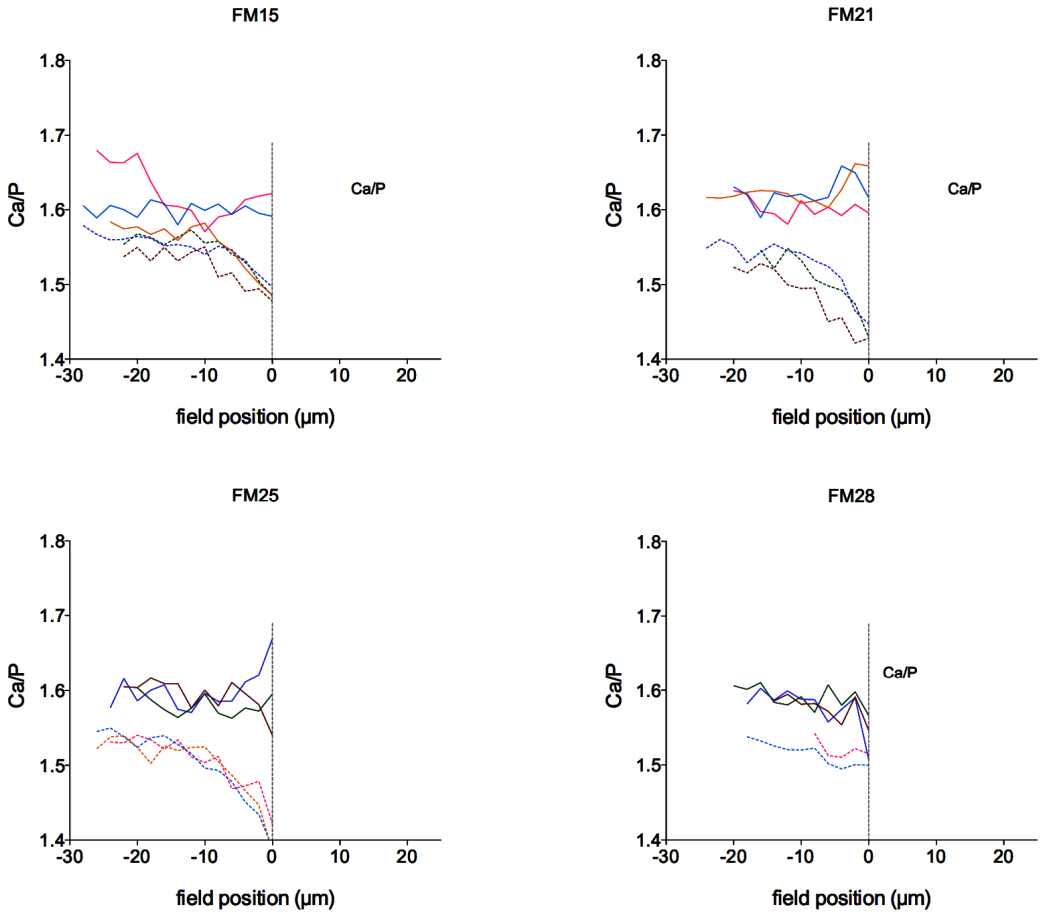

Figure 1: $Ca\ \ P$ ratio at mineralization fronts of four different samples. Dashed lines correspond to periosteal, straight lines to osteonal regions. The gray mark labels the mineralization front.

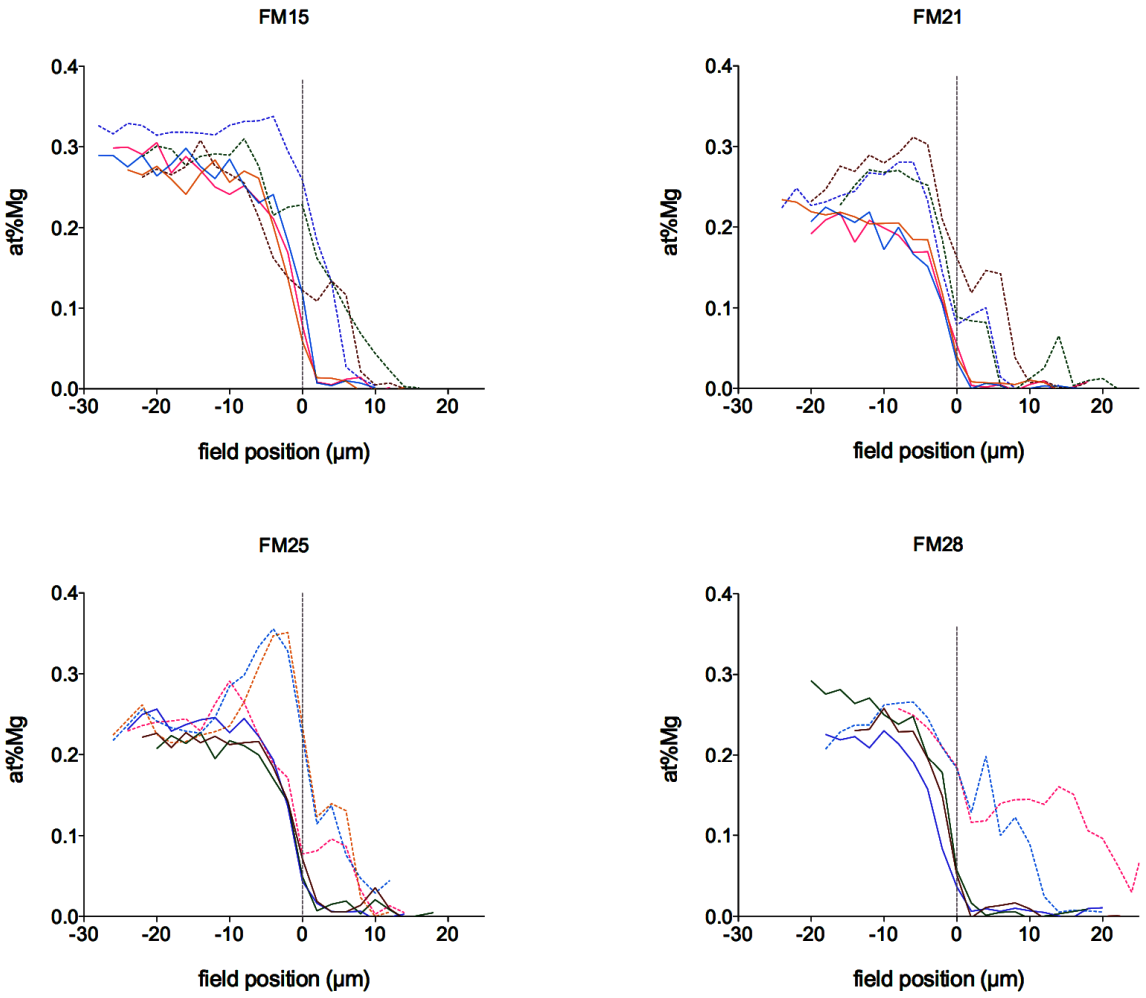

Figure 2: Mg concentration at mineralization fronts of four different samples. Dashed lines correspond to periosteal, straight lines to osteonal regions. The gray mark labels the mineralization front.

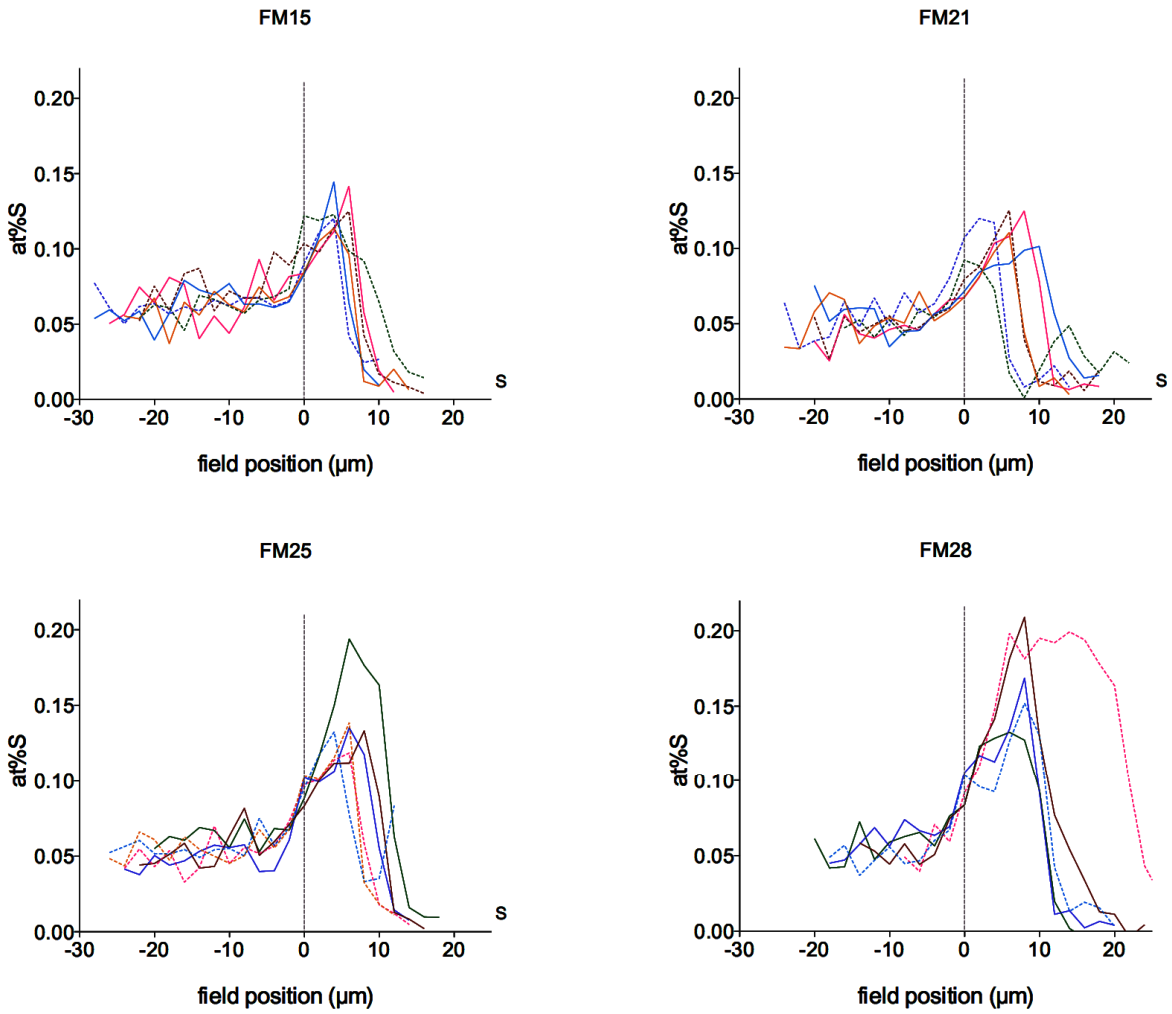

Figure 3: *S* concentration at mineralization fronts of four different samples. Dashed lines correspond to periosteal, straight lines to osteonal regions. The gray mark labels the mineralization front.

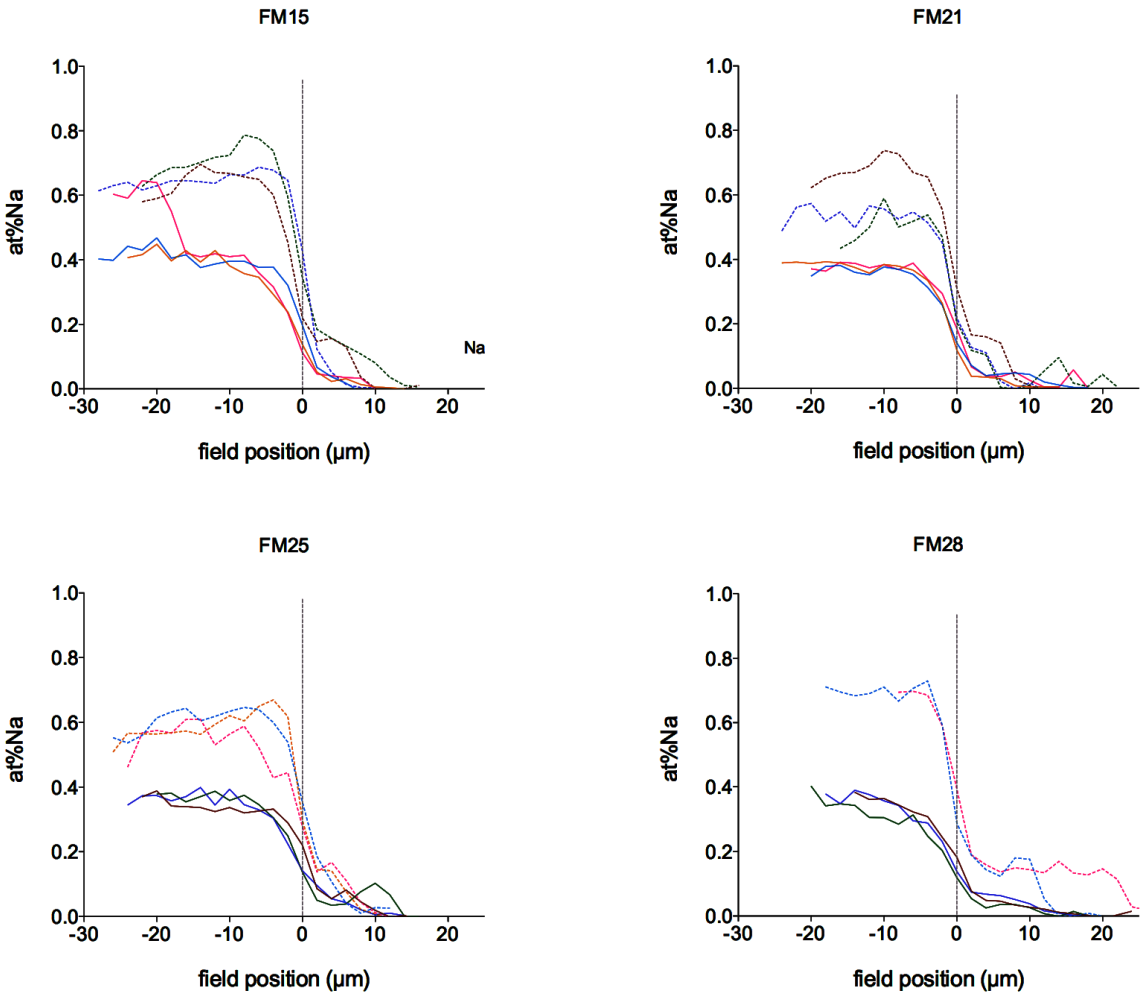

Figure 4: *Na* concentration at mineralization fronts of four different samples. Dashed lines correspond to periosteal, straight lines to osteonal regions. The gray mark labels the mineralization front.

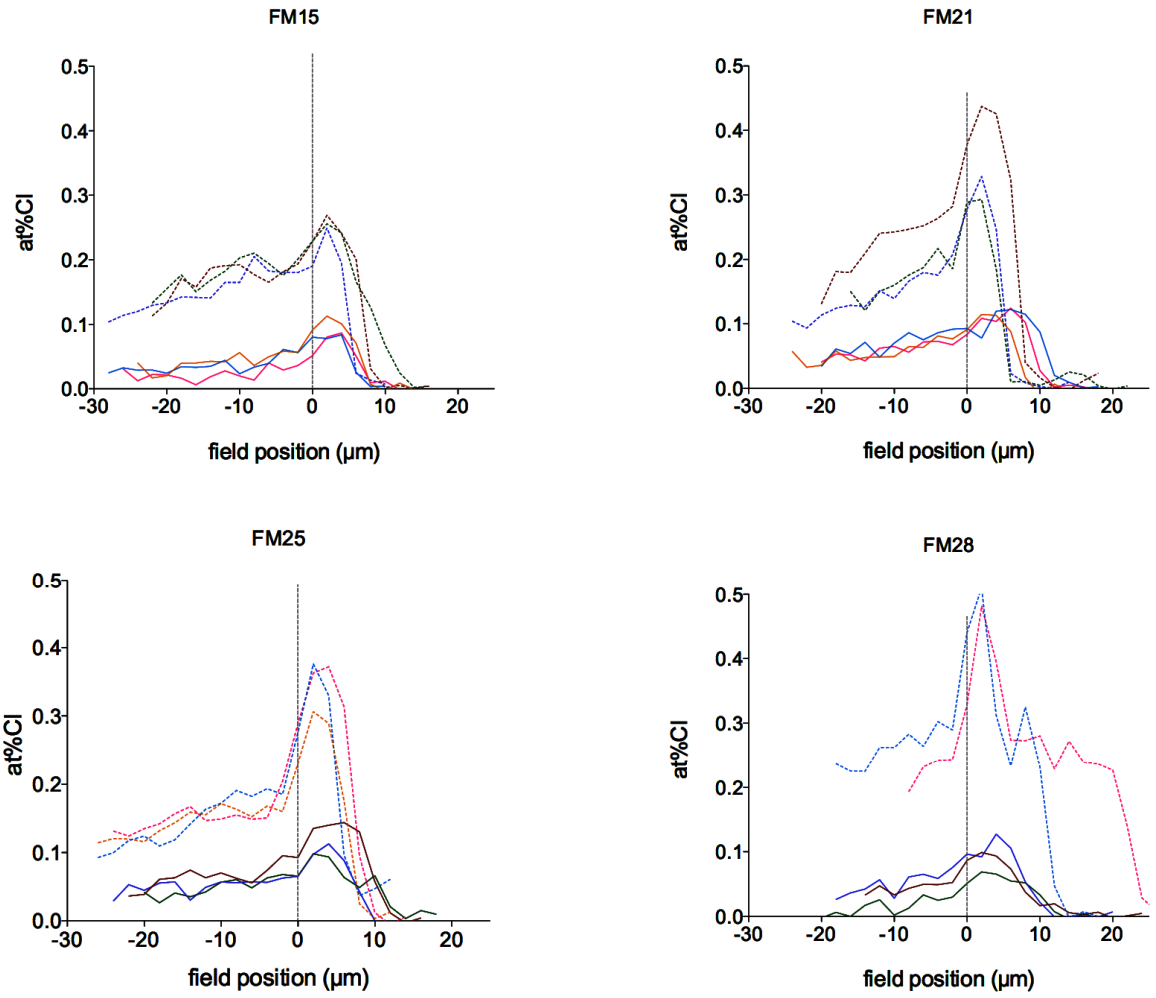

Figure 5: *Cl* concentration at mineralization fronts of four different samples. Dashed lines correspond to periosteal, straight lines to osteonal regions. The gray mark labels the mineralization front.

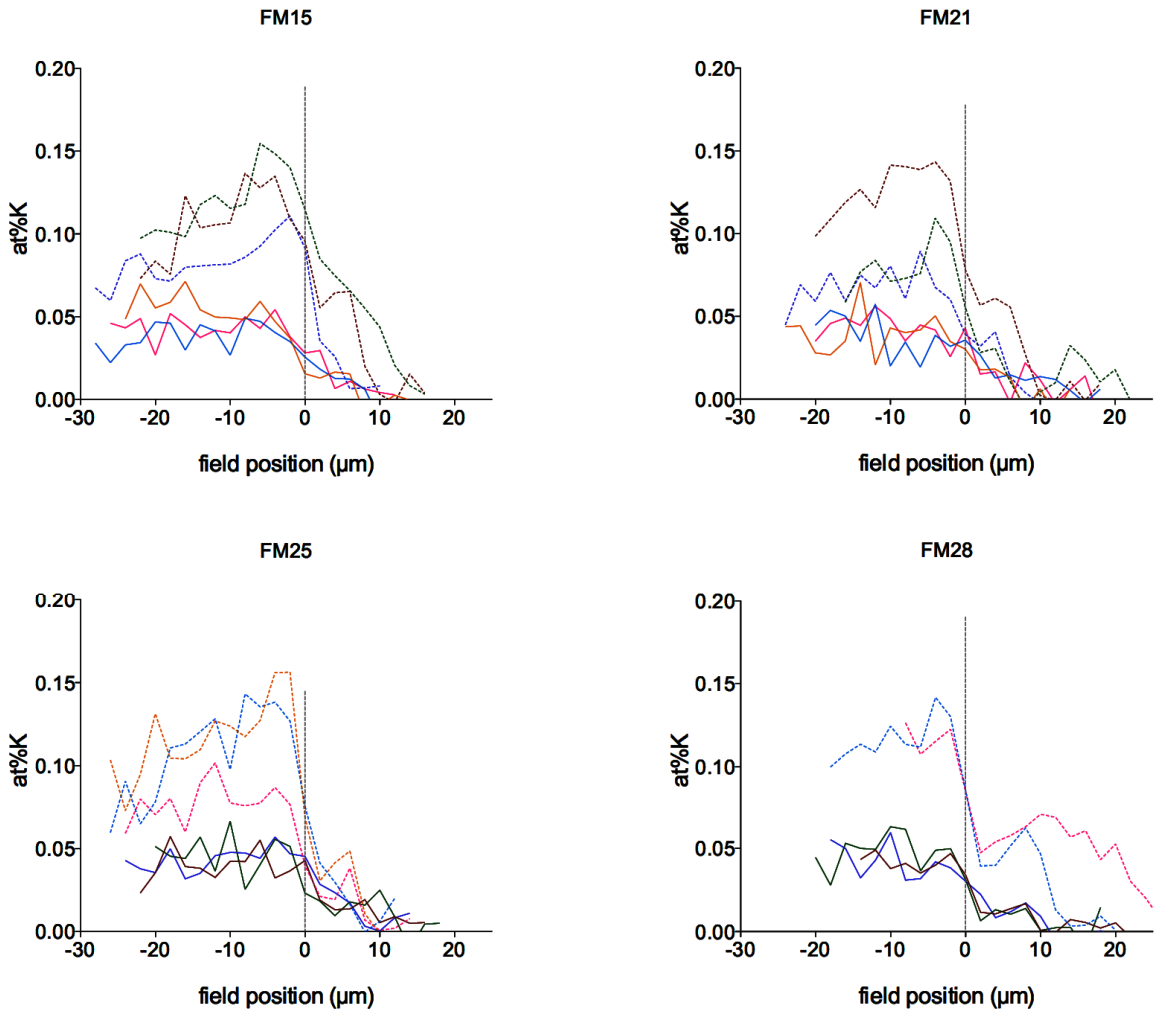

Figure 6: K concentration at mineralization fronts of four different samples. Dashed lines correspond to periosteal, straight lines to osteonal regions. The gray mark labels the mineralization front.

Related Abstracts

Relationship between the $v_2PO_4/amide_{III}$ ratio assessed by Raman spectroscopy and the calcium content measured by quantitative backscattered electron microscopy in healthy human osteonal bone

Roschger A[1,2], *Gamsjaeger S*[1], *Hofstetter B*[1], *Masic A*[2], *Blouin S*[1], *Messmer P*[1], *Berzlanovich A*[3], *Paschalis EP*[1], *Roschger P*[1], *Klaushofer K*[1], *Fratzl P*[2].

[1]Ludwig Boltzmann Institute of Osteology at the Hanusch Hospital of WGKK and AUVA Trauma Centre Meidling, 1st Medical Department, Hanusch Hospital, Heinrich Collin Straße 30, A-1140 Vienna, Austria.
[2]Max Planck Institute of Colloids and Interfaces, 14424 Potsdam, Germany.
[3]Medical University of Vienna, Department of Forensic Medicine, A-1090 Vienna, Austria.

Raman microspectroscopy and quantitative backscattered electron imaging (qBEI) of bone are powerful tools to investigate bone material properties. Both methods provide information on the degree of bone matrix mineralization. However, a head-to-head comparison of these outcomes from identical bone areas has not been performed to date. In femoral midshaft cross sections of three women, 99 regions ($20 \times 20\ \mu m^2$) were selected inside osteons and interstitial bone covering a wide range of matrix mineralization. As the focus of this study was only on regions undergoing secondary mineralization, zones exhibiting a distinct gradient in mineral content close to the mineralization front were excluded. The same regions were measured by both methods. We found a linear correlation ($R^2 = 0.75$) between $mineral/matrix$ as measured by Raman spectroscopy and the $wt.\%Mineral/(100 - wt.\%Mineral)$ as obtained by qBEI, in good agreement with theoretical estimations. The observed deviations of single values from the linear regression line were determined to reflect biological heterogeneities. The data of this study demonstrate the good correspondence between Raman and qBEI outcomes in describing tissue mineralization. The obtained correlation is likely sensitive to changes in bone tissue composition, providing an approach to detect potential deviations from normal bone.

Published:
J Biomed Opt. 2014 Jun;19(6):065002. doi: 10.1117/1.JBO.19.6.065002.

Sclerostin deficiency is linked to altered bone composition.

Hassler N[1*], *Roschger A*[1*], *Gamsjaeger S*[1], *Kramer I*[2], *Lueger S*[1], *van Lierop A*[3], *Roschger P*[1], *Klaushofer K*[1], *Paschalis EP*[1], *Kneissel M*[2], *Papapoulos S*[3].

[1]Ludwig Boltzmann Institute of Osteology at the Hanusch Hospital of WGKK and AUVA Trauma Centre Meidling, 1st Medical Department, Hanusch Hospital, Heinrich Collin Straße 30, A-1140 Vienna, Austria.
[2]Musculoskeletal Disease Area, Novartis Institutes for Biomedical Research, Basel, Switzerland.
[3]Department of Endocrinology and Metabolic Diseases and Leiden Center for Bone Quality, Leiden University Medical Center, 2333 ZA Leiden, The Netherlands

High bone mass in animals and humans with sclerostin deficiency is associated with increased bone strength, which is not the case for all disorders with high bone mineral density, some of which are even associated with fragility fractures owing to unfavorable bone composition. In the current study we investigated whether alterations in bone composition may contribute to the bone strength characteristics associated with lack of sclerostin. We examined cortical bone of $Sost-knockout$ (KO) mice ($n = 9, 16$ weeks old) and sclerosteosis patients (young [4 to 14 years], $n = 4$ and adults [24 and 43 years], $n = 2$) by quantitative backscattered electron imaging and Raman microspectroscopy and compared it to bone from wild-type mice and healthy subjects, respectively. In $Sost - KO$ mice endocortical bone exhibited altered bone composition, whereas subperiosteal bone was unchanged. When comparing endocortical bone tissue of identical tissue age as defined by sequential dual fluorochrome labeling the average bone matrix mineralization was reduced -1.9% ($p < 0.0001$, younger tissue age) and -1.5% ($p < 0.05$, older tissue age), and the relative proteoglycan content was significantly increased. Similarly, bone matrix mineralization density distribution was also shifted toward lower matrix mineralization in surgical samples of compact bone of sclerosteosis patients. This was associated with an increase in mineralization heterogeneity in the young population. In addition, and consistently, the relative proteoglycan content was increased. In conclusion, we observed decreased matrix mineralization and increased relative proteoglycan content in bone subcompartments of $Sost - KO$ mice - a finding that translated into sclerosteosis patients. We hypothesize that the altered bone composition contributes to the increased bone strength of patients with sclerostin deficiency.

Published:
J Bone Miner Res. 2014 Oct;29(10):2144-51. doi: 10.1002/jbmr.2259..

* Both authors contributed equally and are listed in alphabedical order

Effect of sclerostin antibody treatment in a mouse model of severe osteogenesis imperfecta.

Roschger A[1], *Roschger P*[1], *Keplingter P*[1], *Klaushofer K*[1], *Abdullah S*[2], *Kneissel M*[3], *Rauch F*[4].

[1]Ludwig Boltzmann Institute of Osteology at the Hanusch Hospital of WGKK and AUVA Trauma Centre Meidling, 1st Medical Department, Hanusch Hospital, Heinrich Collin Straße 30, A-1140 Vienna, Austria.
[2]Shriners Hospital for Children, Montreal, Quebec, Canada; McGill University, Montreal, Quebec, Canada.
[3]Musculoskeletal Disease Area, Novartis Institutes for Biomedical Research, Basel, Switzerland.
[4]Shriners Hospital for Children, Montreal, Quebec, Canada; McGill University, Montreal, Quebec, Canada.

Osteogenesis imperfecta (OI) is a heritable bone fragility disorder that is usually caused by mutations affecting collagen type I production in osteoblasts. Stimulation of bone formation through sclerostin antibody treatment (Sost-ab) has shown promising results in mouse models of relatively mild OI. We assessed the effect of once-weekly intravenous Sost-ab injections for 4weeks in male $Col1a1^{(Jrt)/+}$ mice, a model of severe dominant OI, starting either at 4 weeks (growing mice) or at 20 weeks (adult mice) of age. Sost-ab had no effect on weight or femur length. In OI mice, no significant treatment-associated differences in serum markers of bone formation (alkaline phosphatase activity, procollagen type I N-propeptide) or resorption (C-telopeptide of collagen type I) were found. Micro-CT analyses at the femur showed that Sost-ab treatment was associated with higher trabecular bone volume and higher cortical thickness in wild type mice at both ages and in growing OI mice, but not in adult OI mice. Three-point bending tests of the femur showed that in wild type but not in OI mice, Sost-ab was associated with higher ultimate load and work to failure. Quantitative backscattered electron imaging of the femur did not show any effect of Sost-ab on CaPeak (the most frequently occurring calcium concentration in the bone mineral density distribution), regardless of genotype, age or measurement location. Thus, Sost-ab had a larger effect in wild type than in $Col1a1^{(Jrt)/+}$ mice. Previous studies had found marked improvements of Sost-ab on bone mass and strength in an OI mouse model with a milder phenotype. Our data therefore suggest that Sost-ab is less effective in a more severely affected OI mouse model.

Published:
Bone. 2014 Sep;66:182-8. doi: 10.1016/j.bone.2014.06.015. Epub 2014 Jun 19.

Eidesstattliche Erklärung

Hiermit versichere ich, dass ich meine Dissertation mit dem Titel "Quantitative Analysis of Local Mineral Content and Composition During Bone Growth and Remodeling" selbstständig erarbeitet und verfasst habe, und keine anderen, als die von mir angegebenen Hilfsmittel und Quellen verwendet habe. Ich versichere, dass ich bisher an keiner Universität, weder im In- noch im Ausland, einen Promotionsversuch unternommen habe. Ich erkläre hiermit außerdem, dass ich die Promotionsordnung der Mathematisch- Naturwissenschaftlichen Fakultät der Humboldt-Universität zu Berlin in der Fassung vom 06. Juli 2009 anerkenne.

Andreas Roschger

Berlin, Februar 2015